Secondary Organic Aerosols: Chemical Aging, Hygroscopicity, and Cloud Droplet Activation

Angela Buchholz

JÜLICH
FORSCHUNGSZENTRUM

Mitglied der Helmholtz-Gemeinschaft

Schriften des Forschungszentrums Jülich
Reihe Energie & Umwelt / Energy & Environment Band / Volume 97

Forschungszentrum Jülich GmbH
Institute of Energy and Climate Research (IEK)
Troposphere (IEK-8)

Secondary Organic Aerosols: Chemical Aging, Hygroscopicity, and Cloud Droplet Activation

Angela Buchholz

Schriften des Forschungszentrums Jülich
Reihe Energie & Umwelt / Energy & Environment Band / Volume 97

ISSN 1866-1793 ISBN 978-3-89336-691-0

Bibliographic information published by the Deutsche Nationalbibliothek.
The Deutsche Nationalbibliothek lists this publication in the Deutsche Nationalbibliografie; detailed bibliographic data are available in the Internet at http://dnb.d-nb.de.

Publisher and Distributor:	Forschungszentrum Jülich GmbH Zentralbibliothek 52425 Jülich Phone +49 (0) 24 61 61-53 68 · Fax +49 (0) 24 61 61-61 03 e-mail: zb-publikation@fz-juelich.de Internet: http://www.fz-juelich.de/zb
Cover Design:	Grafische Medien, Forschungszentrum Jülich GmbH
Printer:	Grafische Medien, Forschungszentrum Jülich GmbH
Copyright:	Forschungszentrum Jülich 2011

Schriften des Forschungszentrums Jülich
Reihe Energie & Umwelt / Energy & Environment Band / Volume 97

D 38 (Diss., Köln, Univ., 2010)

ISSN 1866-1793
ISBN 978-3-89336-691-0

The complete volume ist freely available on the Internet on the Jülicher Open Access Server (JUWEL) at http://www.fz-juelich.de/zb/juwel

Dedicated to Anneliese Buchholz
who never ran out of ideas

Zusammenfassung

Atmosphärische Aerosole haben einen wichtigen Einfluss auf die Strahlungsbilanz und damit auf das Klima der Erde. Aerosolpartikel streuen und absorbieren einfallende solare und terrestrische Strahlung. Abgesehen von diesem direkten Effekt sind sie auch Wolkenkondensationskeime (CCN) und beeinflussen dadurch die Mikrophysik von Wolken. In vielen Regionen machen sekundäre organische Aerosole (SOA) einen großen Anteil der Gesamtaerosolmasse aus. Sie sind hauptsächlich Produkte der Oxidation von biogenen flüchtigen organischen Verbindungen.
In der vorliegenden Arbeit wurde das hygroskopische Wachstum und die CCN-Aktivierung von biogenem SOA untersucht, das durch die Oxidation von VOCs mit Ozone und photochemische gebildeten OH-Radikalen bei geringen NO_x Konzentrationen hergestellt wurde. Zu diesem Zweck wurden in der Jülich Plant Atmosphere Chamber (JPAC) komplexe Mischungen von VOCs, die von für boreale Wälder typischen Baumarten emittiert wurden, als Vorläufer verwendet. In Langzeitstudien in der Atmosphärensimulationskammer SAPHIR wurden α-Pinen oder eine Mischung mit gleichen Anteilen von α-Pinen, β-Pinen, Limonen, Ocimen und Δ-3-Caren als Vorläufer benutzt. Die VOC-Startkonzentrationen lagen zwischen 40 und 1000 ppbC.
Das hier untersuchte SOA war wenig hygroskopisch und der mittlere Hygroskopizitätparameter lag bei $\kappa(\mathrm{CCN}) = 0.10 \pm 0.02$ und $\kappa(90\%RH) = 0.05 \pm 0.01$. Die Messungen des hygroskopischen Wachstums und der CCN-Aktivität konnten zur Deckung gebracht werden unter der Annahme von reduzierter Oberflächenspannung, begrenzter Löslichkeit oder Nichtidealität der Lösung im untersättigten Regime. SOA-Lösungen, die mit RH <95% im Gleichgewicht sind, sind wahrscheinlich hoch nichtideal. Deshalb wurden die Wasser-Organik-Wechselwirkungen mit dem UNIFAC-Model untersucht. Berechnungen mit Surrogatverbindungen ergaben die gleiche starke Konzentrations- bzw. RH-Abhängigkeit von κ bei Untersättigung. Für die Anpassung der Wachstumskurven und die Vorhersage der CCN-Eigenschaften wurde ein binäres Wasser-Organik-System angenommen und das Auftreten der funktionellen Gruppen in dieser hypothetischen Verbindung angepasst. Allerdings werden weitere Angaben zur Oberflächenspannung und dem Verhältnis von Molmasse und Dichte des gelösten Stoffs benötigt, um aus Messungen des hygroskopischen Wachstums die Aktivierungseigenschaften abzuleiten.
Es wurde eine Abhängigkeit von κ vom Verhältnis aus OH-Primärproduktion und VOC-Startkonzentration festgestellt. Die höhere κ-Werte bei niedrigen Vorläuferkonzentrationen konnte dem ebenfalls höheren OH/VOC-Level zugeschrieben werden. Die genaue chemische Zusammensetzung der Vorläufersubstanzen hatte nur einen geringen Einfluss auf κ. In Langzeitstudien hatte die beobachtete chemische

Alterung der Partikle keinen signifikanten Effekt auf κ. Die beobachtete geringe Varabilität von κ erleichtert die Einbindung in globale Modelle, da ein mittlerer Wert von $\kappa = 0.1$ angenommen werden kann.

Abstract

Atmospheric aerosols have an important impact on the radiation balance, and thus, on the climate of the Earth. Aerosol particles scatter and absorb incoming solar and terrestrial radiation. Apart from this direct effect, aerosol particles act as cloud condensation nuclei (CCN), thereby greatly influencing the microphysics of clouds. Secondary organic aerosols (SOA) are an important fraction of the total aerosol mass. In many environments these organic compounds are mainly products of the oxidation of biogenic volatile organic compounds (VOC).
In this study the hygroscopic growth and CCN activation of biogenic SOA were investigated which was formed by the oxidation of VOC with O_3 and photochemically formed OH radicals under low NO_x conditions. For this purpose, a complex mixture of VOC emitted by boreal tree species as gas-phase precursors was used in the Jülich Plant Atmosphere Chamber (JPAC). In long-term studies in the atmosphere simulation chamber SAPHIR α-pinene or a defined mixture of α-pinene, β-pinene, limonene, ocimene, Δ-3-carene served as precursors. Initial precursor concentrations between 40 and 1000 ppbC were investigated.
The observed SOA particles were slightly hygroscopic with an average hygroscopicity parameter $\kappa(\mathrm{CCN}) = 0.10 \pm 0.02$ and $\kappa(90\%RH) = 0.05 \pm 0.01$. Closure between hygroscopic growth and CCN activation data could be achieved allowing either surface tension reduction, limited solubility, or non-ideality of the solution in the droplet. The SOA solutions in equilibrium with RH <95% are possible highly non-ideal. Therefore the organic-water interaction were investigated by applying the UNIFAC model. Calculations for surrogate compounds exhibited the same strong concentration (i.e. RH) dependence of κ at sub-saturation. The growth curves could be fitted and CCN activation predicted by assuming a binary mixture of water and one hypothetical organic compound. The occurrence of functional groups in this compound was adjusted to reproduce the observed growth curves. However, further information on surface tension and the ratio of the molecular mass and density of the solute is needed to predict activation behavior from hygroscopic growth measurements.
A dependence of κ on the ratio of primarily produced OH to initial VOC level was observed. The higher κ values for low precursor concentrations could be attributed to a higher OH/VOC level. The detailed chemical composition of the gas-phase precursors had only little effect on κ. In long term experiments there was no significant effect of the observed chemical aging of the particles on κ. The observed low variability of κ for biogenic SOA particles simplifies their treatment in global models as an average value of $\kappa = 0.1$ can be used.

Contents

List of Figures

List of Tables

Abbreviations

AE	activation efficiency
AH	absolute humidity in Pa
AMS	Aerosol Mass Spectrometer
APCI-MS	Atmospheric Pressure Chemical Ionization Mass Spectrometer
a_w	water activity
b	bright radiation conditions with j($O(^1D)$) above $10^{-6}s^{-1}$
BMT	boreal monoterpenes: α-pinene, β-pinene, limonene, ocimene, Δ-3-carene
c	cloudy radiation conditions with j($O(^1D)$ below $10^{-6}s^{-1}$
CCN	cloud condensation nuclei
CCN-C	Cloud Condensation Nuclei Counter
CN	condensation nuclei
CO	carbon monoxide
CPC	Condensed Particle Counter
$D50$	diameter of dry particles which are activated at set SS
DMA	Differential Mobility Analyzer
DMT	Droplet Measurement Technologies
DRH	RH at the deliquescence point
ERH	RH at efflorescence (recrystallization) point
GC-MS	Gas Chromatograph Mass Spectrometer
GF	hygroscopic growth factor
HNO_2	nitrous acid
HR-Tof-AMS	High Resolution Time-of-flight Aerosol Mass Spectrometer
HTDMA	Hygroscopicity Tandem Differential Mobility Analyzer
j($O(^1D)$)	photolysis rate of O_3 to $O(^1D)$
JPAC	Juelich Plant Atmosphere Chamber
$\kappa(90\%)$	hygroscopicity parameter κ calculated from GF at 90% RH
κ(CCN)	hygroscopicity parameter κ derived from fitting equation 2.29 to the measured $SS_{crit}/D50$ data
MT	monoterpene
$(NH_4)_2SO_4$	ammonium sulfate
NO_x	nitrogen oxids (NO, NO_2)
O_3	ozone
OA	organic aerosol
$O(^1D)$	excited oxygen radical at state (^1D)
OH	hydroxyl radical
OMT	oxidized monoterpenes

Pa	Pascal
PC	plant chamber
ppbC	parts per billion related to carbon
ppb	parts per billion
ppm	parts per million
PSL	polystyrene latex
PTR-MS	Proton Transfer Reaction Mass Spectrometer
RC	reaction chamber
RH	relative humidity
SAPHIR	Simulation Atmosphärischer Photochemie in einer großen Reaktionskammer
SMPS	Scanning Mobility Particle Sizer
SQT	sesquiterpenes
SS	super-saturation
SS_{crit}	critical SS at the activation point
TgC/a	Teragramm carbon per year
UNIFAC	Universal Quasi chemical Functional Group Activity Coefficients
VOC	volatile organic compound

1. Introduction

1.1 Atmospheric aerosols

Aerosols are defined as a suspension of solid or liquid particles in gas. In a strict sense the term aerosol refers to both, the gas and the particle phase. In atmospheric science the term is often used to describe only the particle phase.

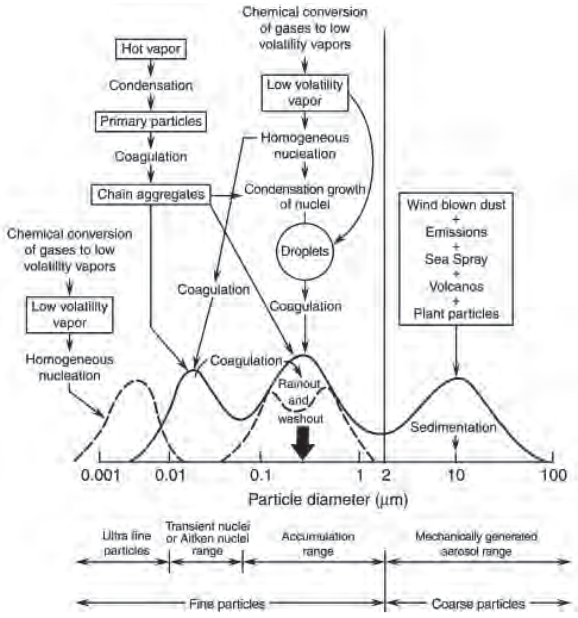

Figure 1.1: *Schematic aerosol size distribution. Adapted from Finlayson-Pitts and Pitts (2000). The typical four mode size distribution with the formation and loss processes for each mode is shown. The solid lines represents the original hypothesis of Whitby and Sverdrup (1980). The dashed lines include the ultra fine particle mode in the aerosol size distribution.*

The size of atmospheric aerosol particles range from 10^{-9} to 10^{-4} m. A typical (schematic) size distribution is shown in Figure 1.1 (*Finlayson-Pitts and Pitts* (2000)). A selection of the large number of complex processes leading to particle formation is indicated in this figure. On the one hand, primary aerosols are emitted directly into the atmosphere e.g. mineral dust, sea spray, or soot from biomass or fossil fuel burning. On the other hand, gas-phase compounds from

various sources are oxidized in the atmosphere to yield low-volatile products, which may form new (secondary) particles or condense on existing ones. The size of the particles increases with time due to this condensation of new vapors and coagulation of the particles. The major removal processes are wash-out by rain or other precipitation, and sedimentation and dry deposition of large particles. Typically, the lifetime of aerosol particles in the troposphere is several days. During this time the particles may be transported away from the source region, and chemical and physical changes can occur to the particles. This processing in the atmosphere is called aging.
In Figure 1.2 the composition of submicron aerosol particles is shown measured at different locations in the northern hemisphere with Aerosol Mass Spectrometers (AMS, *Zhang et al.* (2007)). Beside the inorganic species (sulfate, ammonium, nitrate, and chloride) organic matter is detected in all probed environments. Depending on the region, it composes 18 to 70% of the total aerosol mass. (Note that the AMS cannot detect refractory compounds e.g. soot or mineral dust.)

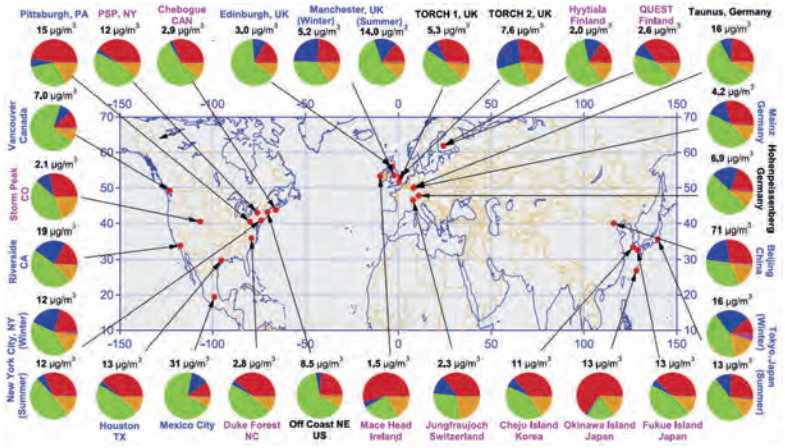

Figure 1.2: *Composition of aerosol particles* $< 1\mu m$ *determined from AMS measurements. Type of sampling location is indicated as following: urban areas (blue),* <100 *miles downwind of major cities (black), rural/remote areas* >100 *miles downwind of major cities (pink). Pie charts show the average mass concentration and chemical composition: organics (green), sulfate (red), nitrate (blue), ammonium (orange), chloride (purple). Taken from Zhang et al. (2007)*

1.2 Secondary organic aerosol

Organic aerosols (OA) are an important constituent of atmospheric aerosols. *Hallquist et al.* (2009) find that the main fraction of OA is made up by secondary organic aerosol (SOA) from oxidation of biogenic volatile organic compounds (VOC). This corresponds to the much higher emissions of biogenic VOCs (430 - 1150 TgC/a) compared to anthropogenic VOCs (160 TgC/a, *Guenther et al.*

(1995)). Similar findings are reported by *Kanakidou et al.* (2005) with up to 90% contribution of SOA to OA in boreal and tropical regions (see Figure 1.3). However, the formation of SOA is underestimated in current models by one or two orders of magnitude (*Goldstein and Galbally* (2007), *Heald et al.* (2005)). This indicates that the understanding of SOA formation is still incomplete.

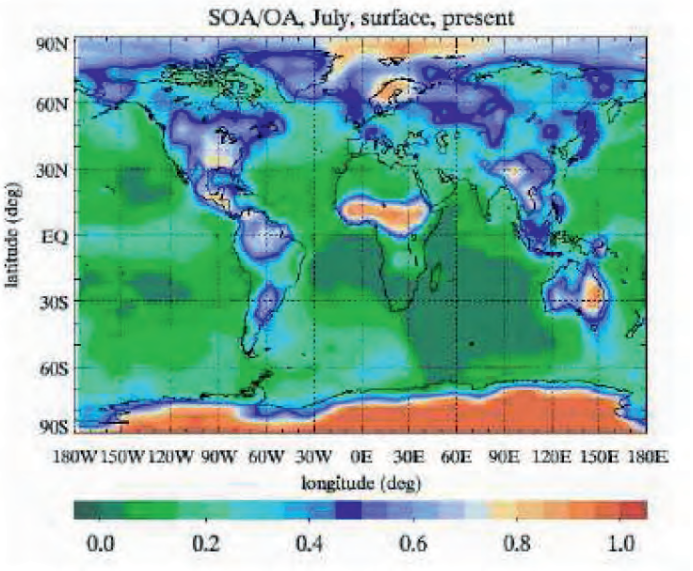

Figure 1.3: *Contribution of SOA to all organic aerosol calculated with a 3-D global chemistry transport model for July. Taken from Kanakidou et al. (2005).*

Generally, VOC are oxidized by reactions with ozone (O_3), hydroxyl radicals (OH), or nitrate radicals. C-C double bonds are most reactive, but OH and NO_3 radicals react also with C-H bonds. Most oxidation products have a lower saturation vapor pressure than the precursors. Thus, super-saturation with respect to the oxidized compounds can be achieved quickly and nucleation will occur forming new particles. If the available particle surface is able to take up the produced condensable vapors, no new particles are formed. Instead, condensational growth of the existing particles is observed.
The global VOC emissions are dominated by isoprene (*Guenther et al.* (1995)). The next abundant compounds are the group of monoterpenes (MT). The emissions of boreal tree species are dominated by MT. If plants are subject to abiotic (heat, drought) or biogenic stress (plant disease), sesquiterpenes (SQT) and oxidized compounds are emitted. Another indicator for stress is ocimene and its isomers. The oxidation of these different VOC types should lead to a rather different chemical composition of the formed SOA.

1.3 Aerosol climate interactions

Atmospheric aerosols have an important impact on regional and global climate. Depending on their composition aerosol particles scatter or absorb the incoming solar and terrestrial radiation. This direct effect leads to a negative radiative forcing of -0.50±0.40 W/m^2 (*Forster et al.* (2007)). Apart from this, aerosols greatly influence the microphysics of clouds: their radiative properties, occurrence, and lifetime. Direct and indirect effects of aerosol particles on the radiation are summarized in Figure 1.4. If the liquid water content in the cloud is constant, an increase in the amount of cloud condensation nuclei (CCN) leads to smaller cloud droplets. Therefore, the cloud albedo is increased in comparison to an unperturbed cloud. At the same time, the lifetime of the formed cloud is increased. Additionally, the extend and height of the cloud changes and also the precipitation probability is influenced. In the current IPCC report only the effect of enhanced cloud albedo is considered. This results in a negative radiative forcing of -0.7(-1.1/+0.4) W/m^2 (*Forster et al.* (2007)).

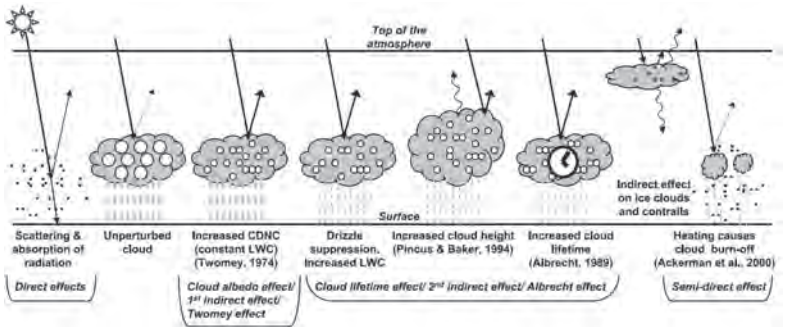

Figure 1.4: *Schematic diagram showing the various radiative mechanisms associated with cloud effects that have been identified as significant in relation to aerosols. The small black dots represent aerosol particles; the larger open circles cloud droplets. Straight lines represent the incident and reflected solar radiation, and wavy lines represent terrestrial radiation. The white circles indicate cloud droplet number concentration (CDNC). The vertical gray dashes represent rainfall, and LWC refers to the liquid water content. Taken from Forster et al. (2007).*

1.4 Focus of this work

The aim of this work was to investigate the influence of the gas-phase precursors and oxidation conditions on the microphysical properties of the formed SOA. Furthermore, the temporal evolution of these properties due to chemical aging of the particles was studied. Since both, hygroscopic growth and cloud droplet activation, were measured, they could be related to each other and other physical-chemical properties were derived (closure study).

For this investigations SOA was produced from photo oxidation and ozonolysis of biogenic gas-phase precursors in two different simulation chambers and the hygroscopic properties and CCN activation of these particles were measured. In one simulation chamber emissions from real tree species were used. In these experiments the main constituents of the tree emissions were identified. The five dominant MT were used as precursors in the other chamber where experiments on a longer timescale were possible and natural sunlight could be used for photochemistry.
In the first part of this work the theory describing the hygroscopicity of aerosol particles and the parameterizations of this theory are presented. These parameters will be used to describe the measured data. The second part comprises the description of the experimental set-up and a list of all conducted experiments. In part three and four the measured data is shown and discussed with regard to the objectives of this work.

2. Theory

In this chapter the general Koehler theory will be presented since it is the theoretical description of the hygroscopicity of aerosol particles. Two of the previously applied single parameter approaches of the Koehler equation will be shown (κ, ρ_{ion}). Finally, the UNIFAC model will be described briefly. This model was used to estimate the water activity in the solution droplets.

2.1 Hygroscopicity of aerosol particles

Aerosol particles interact with water vapor in the surrounding gas phase. In figure 2.1 the dependence of the particle size on the water vapor saturation ratio (S) is shown for two different dry particle sizes (20 nm: red and orange, 80 nm: light and dark blue). In the following S below 1 is called relative humidity (RH) and above 1 supersaturation (SS).

$$\begin{aligned} RH &= S \cdot 100\% \\ SS &= S \cdot 100\% - 100\% \end{aligned} \tag{2.1}$$

For low RH the Gibbs free energy of a solid soluble salt (in this example ammonium sulfate) is lower than that of the corresponding aqueous solution. Thus, no water vapor is taken up, and the particle diameter stays constant (orange and light blue straight line). At a substance-specific RH the Gibbs free energy of the saturated solution becomes less than that of the solid. Hence, water condenses on the particles forming a saturated solution, and the particle diameter increases. This is called deliquescence point and the corresponding RH deliquescence RH (DRH). With increasing RH more water condenses and the particles grow further. If the RH decreases again, the corresponding amount of water evaporates and the particles shrink. When the RH drops below the DRH, a metastable, supersaturated solution is formed (red and dark blue line) as the (homogeneous) recrystallization of the salt and evaporation of all water is kinetically hindered. At the efflorescence point (ERH) the kinetic barrier is overcome and the salt crystallizes forming a solid particle.
For S above 1 (supersaturation with respect to water) the droplet growth continues with increasing SS. But above a certain droplet size (maximum of the curves) the droplets will continue to grow even if the SS decreases and will eventually become cloud droplets. Therefore, this is called the activation point. The SS at this point is called critical SS (SS_{crit}) and the particle diameter critical wet diameter (D^{w}_{crit}). The position of the activation point depends on the diameter of the dry particle: the larger the starting diameter the lower the critical SS. For

technical reasons the measured activation extends over a certain small range of D_p. For a given SS_{crit} the diameter of dry particles where 50% of the particles activate is called $D50$.

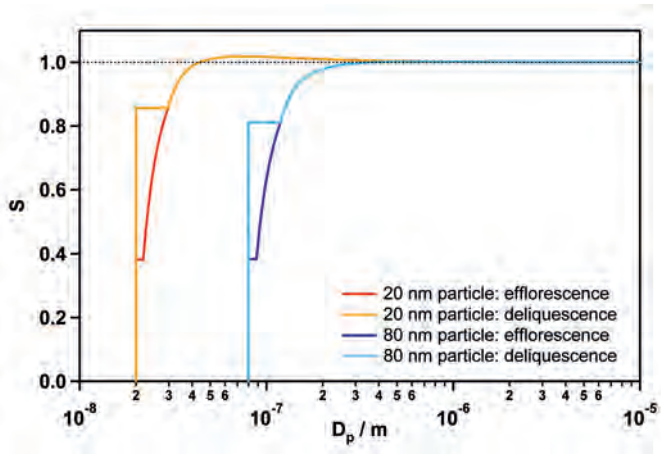

Figure 2.1: *Koehler curves for ammonium sulfate particles of different dry sizes (orange and red: 20 nm, light and dark blue: 80 nm).*

2.2 Koehler theory

2.2.1 General application

The Koehler theory (*Köhler* (1936)) describes the interaction of an aqueous solution droplet with the surrounding gas phase. The vapor pressure of water over the curved solution depends on both, the amount of solute in the solution and the curvature of the droplet. These two effects can be treated separately.
Over a flat surface of an aqueous solution the saturation vapor pressure is given by Raoult's law. The ratio of the saturation vapor pressure over the solution (p^0_{sol}) and pure water (p^0_w) equals the water activity (a_w) in the solution.

$$p^0_{sol} = a_w \cdot p^0_w \Longleftrightarrow \frac{p^0_{sol}}{p^0_w} = a_w \tag{2.2}$$

The Kelvin effect describes the ratio of the saturation vapor pressure of pure water over a curved ($p_w(D_p)$) and a flat surface (p^0_w). The curvature of the surface is characterized by the curvature radius ($\frac{D_p}{2}$).

$$\frac{p_w(D_p)}{p^0_w} = exp\left(\frac{4\overline{V}_w\,\sigma_w}{R\,T\,D_p}\right) \tag{2.3}$$

$\overline{V}_w$	: partial molar volume of water	
σ_w	: surface tension of pure water at T	
R	: universal gas constant	$(8.314\ J/Kmol)$

By combining equations 2.2 and 2.3 the saturation ratio (S) over a solution droplet with the diameter D_p is given by:

$$S = \frac{p_{sol}(D_p)}{p_w^0} = a_w \cdot exp\left(\frac{4\overline{V}_w\,\sigma_{sol}}{R\,T D_p}\right) \tag{2.4}$$

$p_{sol}(D_p)$: saturation water vapor pressure over a curved surface of the solution with a curvature radius of $\frac{D_p}{2}$
σ_{sol} : surface tension of the solution

2.2.2 Parametrization of the Koehler theory

The Koehler theory given in equation 2.4 is generally applicable. No additional assumptions to those for Raoult's law and the Kelvin equation are necessary to describe the hygroscopicity of aerosol particles. But for calculations with a real (atmospheric) aerosol several of the parameters in equation 2.4 are unknown. The partial molar volume of water and the surface tension of the solution in the droplet are difficult to assess. Furthermore, the water activity in the droplet of a given size needs to be determined. In this section, first the general approximations are described. Then two different ways of parameterizing the water activity are presented.
As a first approximation, the surface tension of pure water is used for the solution (0.072 N/m at 298 K). This may be valid for pure inorganic salt particles but several compounds identified in organic aerosols have the potential to reduce the surface tension (e.g. *Facchini et al.* (2000) and *Dinar et al.* (2006)). In several studies the agreement between measured data and Koehler theory could be improved by applying a reduced surface tension e.g. for particles containing humic acid like substances (*Ziese et al.* (2008), *Asa-Awuku et al.* (2010) etc). Other studies (*Prisle et al.* (2008)) imply that the surface tension effect may be partially compensated by surface partitioning of the surface active compounds. Hence, as no additional information is available in this study, the surface tension of pure water is used.
To enable the calculation of the volume of water in the solution from the dry and wet particle size, volume additivity is assumed. I.e. the change in volume due to mixing is neglected. As a direct consequence of this assumption the partial molar volume ($\overline{V}_w$) of water then equals the molar volume ($\overline{V}_w^0$), which can be expressed as the ratio of the molar weight (M_w) and the density of pure water (ρ_w).

$$\overline{V}_w^0 = \frac{M_w}{\rho_w} \tag{2.5}$$

Thus, the Koehler equation (2.4) changes to:

$$S = a_w \cdot exp\left(\frac{4M_w\sigma_w}{R\,T\rho_w D_p}\right) \tag{2.6}$$

This approximation can cause severe errors in the partial molar volume of ionic

inorganic systems. However, for organic substances that are in the focus of this work (big molecules, compared to water, with polar groups) only a small volume contraction due to mixing is expected and the effect gets less important the more dilute the solution is. This would lead to an underestimation of the amount of water molecules in the droplet, i.e. the calculated molar fraction of water (x_w) for a measured RH/GF pair would be too low. The hygroscopicity deduced would be to low as well. But as there is no data on the concentration dependent partial molar volume and the exact composition of the mixture of organic compounds in the particle is not known, the ideal assumption is applied.

Osmotic coefficient ϕ

The osmotic coefficient ϕ can be used to describe the water activity. The rational osmotic coefficient (ϕ_{rat}) is defined as the ratio of the osmotic pressure of a real solution (Π_{real}) and the ideal solution (Π_{id}):

$$\phi_{rat} = \frac{\Pi_{real}}{\Pi_{id}} = \frac{ln(a_w)}{ln(x_w)} \tag{2.7}$$

Using that the sum of the mole fraction of water (x_w) and of the solute (x_s) equals 1 and that for small x_s: $ln(1 - x_s) = - x_s$, equation 2.7 changes to:

$$\phi = -\frac{ln(a_w)}{x_s} = - ln(a_w) \cdot \frac{n_w + n_s}{n_s} \tag{2.8}$$

Since for small x_s the amount of solute (n_s) is much smaller than the amount of water in the solution n_w, equation 2.8 becomes:

$$\phi = - ln(a_w) \cdot \frac{n_w}{n_s} \tag{2.9}$$

Equation 2.9 is identical to the definition of the molal osmotic coefficient (ϕ). Hence, for dilute solutions the molal osmotic coefficient equals the rational osmotic coefficient. Both coefficients approach 1 as $a_w \to 1$.
Assuming that the dry particle is spherical, n_s can be calculated from the diameter and density of the dry particle. With the factor ν both, dissociation of salts ($\nu > 1$) and incomplete dissolving of the solute ($\nu < 1$), are included.

$$n_s = \nu \cdot \frac{V_s \cdot \rho_s}{M_s} = \nu \cdot \frac{\pi}{6} \cdot \frac{D_{dry}^3 \cdot \rho_s}{M_s} \tag{2.10}$$

ν : number of dissolved entities per molecule of solute
V_s : volume of the solute
ρ_s : density of the dry particle
M_s : molar mass of the dry solute
D_{dry} : diameter of the dry particle

n_w can be calculated from the difference of the droplet volume (V_p) and V_s. As volume additivity is assumed, it does not matter if the solute is completely dissolved or an insoluble core remains. Additionally, the molar volume of pure

water (equation 2.5) can be applied.

$$\begin{aligned} n_w &= \frac{V_w \cdot \rho_w}{M_w} = \frac{(V_p - V_s) \cdot \rho_w}{M_w} \\ n_w &= \frac{\pi}{6} \cdot \frac{(D_p^3 - D_{dry}^3) \cdot \rho_w}{M_w} \end{aligned} \tag{2.11}$$

ρ_w : density of pure water
M_w : molar mass of water ($0.018\ kg/mol$)

Combining equations 2.9 to 2.11 with the Koehler equation 2.6 leads to:

$$S = exp\left(\frac{4M_w\sigma_w}{R\,T\rho_w D_p} - \phi\nu \cdot \frac{\rho_s M_w}{\rho_w M_s} \cdot \frac{D_{dry}^3}{(D_p^3 - D_{dry}^3)}\right) \tag{2.12}$$

Parameter ρ_{ion}

For most aerosol systems the parameters ϕ, ρ_s, ν, and M_s are unknown. Hence, *Wex et al.* (2007) proposed to merge them into the new parameter ρ_{ion}. This is the number of entities (ions and/or molecules) per dry solute that are expected to dissolve in order to produce the same behavior as the real solution assuming an ideal solution:

$$\rho_{ion} = \nu\phi\frac{\rho_s}{M_s} \tag{2.13}$$

Then equation 2.12 changes to:

$$S = exp\left(\frac{4M_w\sigma_w}{R\,T\rho_w D_p} - \rho_{ion} \cdot \frac{M_w}{\rho_w} \cdot \frac{D_{dry}^3}{(D_p^3 - D_{dry}^3)}\right) \tag{2.14}$$

Hygroscopicity parameter κ

Petters and Kreidenweis introduced the hygroscopicity parameter κ to parameterize the water activity (*Petters and Kreidenweis* (2007)).

$$a_w = \left(1 + \kappa\,\frac{V_s}{V_w}\right)^{-1} \tag{2.15}$$

As shown in the previous section under assumption of volume additivity the volume of water (V_w) and the solute (V_s) in the droplet can be calculated from the droplet and dry particle diameter, respectively.

$$V_s = \frac{\pi}{6} \cdot D_{dry}^3 \tag{2.16}$$

$$V_w = V_p - V_s = \frac{\pi}{6}\left(D_p^3 - D_{dry}^3\right) \tag{2.17}$$

The combination of equations 2.6, 2.16 and 2.17 leads to the so called κ-Koehler equation:

$$S = \left(1 + \kappa \frac{D_{dry}^3}{\left(D_p^3 - D_{dry}^3\right)}\right)^{-1} \cdot exp\left(\frac{4 M_w \sigma_w}{R\,T \rho_w D_p}\right) \tag{2.18}$$

The water activity can also be written as the mole fraction of water (x_w) multiplied with a molar activity coefficient (γ_w):

$$a_w = \gamma_w \cdot x_w = \gamma_w \cdot \frac{n_w}{n_w + n_s} \tag{2.19}$$

Combining equations 2.15 and 2.19 results in:

$$a_w = \left(1 + \kappa \frac{V_s}{V_w}\right)^{-1} = \gamma_w \cdot \frac{n_w}{n_w + n_s} \tag{2.20}$$

For very dilute solutions ($a_w \to 1$) γ_w approaches 1. Then equation 2.20 can be solved for κ.

$$\begin{aligned} \frac{n_w + n_s}{n_w} &= 1 + \kappa \frac{V_s}{V_w} \\ \kappa = \frac{\overline{V}_w^0}{\overline{V}_s^0} &= \frac{M_w}{\rho_w} \cdot \frac{\nu \rho_s}{M_s} \end{aligned} \tag{2.21}$$

This means for dilute solutions κ will approach the ratio of the molar volumes of water and the solute.

Relation of the parameters ϕ, ρ_{ion}, and κ

ϕ, ρ_{ion}, and κ are only different ways of expressing a_w, or more precisely the difficult to assess non-ideality of the solution. They can be directly related to each other. ρ_{ion} is already linked to ϕ by definition (equation 2.13). Using equations 2.9 to 2.11 a_w can be written as:

$$a_w = exp\left(-\rho_{ion} \frac{V_s M_w}{V_w \rho_w}\right) \tag{2.22}$$

Combining this with equation 2.20 and solving the equation for κ leads to:

$$\begin{aligned} \left(1 + \kappa \frac{V_s}{V_w}\right)^{-1} &= exp\left(-\rho_{ion} \frac{V_s M_w}{V_w \rho_w}\right) \\ \kappa &= \frac{V_w}{V_s} \cdot \left(exp\left(\rho_{ion} \frac{V_s M_w}{V_w \rho_w}\right) - 1\right) \end{aligned} \tag{2.23}$$

If the exponential term is developed as a series expansion, which is terminated after the linear term, one obtains:

$$\begin{aligned} \kappa &= \left(1 + \rho_{ion}\frac{V_s M_w}{V_w \rho_w} - 1\right) \cdot \frac{V_w}{V_s} \\ \kappa &= \rho_{ion}\frac{M_w}{\rho_w} = \rho_{ion}\overline{V}_w \end{aligned} \tag{2.24}$$

Thus, κ and ρ_{ion} are related by a constant factor of $1.8 \cdot 10^{-5}$ as long as these approximations hold. But even if this is not the case, they can be converted for each measured data point by applying equation 2.24. To calculate the corresponding ϕ with equation 2.13, values for M_s, ρ_s, and ν must be assumed or obtained from other measurements.

Approximations for CCN activation

To investigate the position of the maximum of the Koehler curve ($D50$ and SS_{crit}) equation 2.14 is used. At the maximum of the curve the derivative of the function equals 0. To solve this analytically, it is assumed that the volume of the dry particle can be neglected in comparison to the droplet volume at the activation point. Equation 2.14 simplifies to:

$$\begin{aligned} S &= exp\left(\frac{A}{D_p} - \frac{B}{D_p^3}\right) \\ A &= \frac{4 M_w \sigma_w}{R\,T \rho_w} \\ B &= \frac{\rho_{ion} M_w D_{dry}^3}{\rho_w} \end{aligned} \tag{2.25}$$

D_{crit}^w and S_{crit} are then given by:

$$D_{crit}^w = \frac{3B}{A} \tag{2.26}$$

$$S_{crit} = exp\left(\left(\frac{4A^3}{27B}\right)^{\frac{1}{2}}\right) \tag{2.27}$$

Converting the saturation ratio S into SS (in %) and using a series expansion for the exponential term (terminated after the linear term) yields:

$$SS_{crit} = \left(\frac{4A^3}{27B}\right)^{\frac{1}{2}} \tag{2.28}$$

The $SS_{crit}/D50$ pairs obtained in CCN-C measurements can be fitted with equation 2.28 using $D50$ as D_{dry} and p_0 as a free parameter.

$$SS_{crit} = p_0 \cdot D50^{-\frac{3}{2}} \tag{2.29}$$

A value for the surface tension must be assumed to calculate ρ_{ion} from the fitting parameter p_0.

$$\rho_{ion} = \frac{2.56 \cdot 10^6 M_w^2}{27 R^3 T^3 \rho_w^2} \cdot \sigma^3 \cdot {p_0}^{-2} \tag{2.30}$$

This approach is similar to the "Koehler theory analysis" presented in *Padro et al.* (2007).

2.3 UNIFAC model

The activity coefficient describes the deviation of a real mixture of compounds from the ideal behavior (equation 2.19). It is impossible to measure the activity coefficients of all possible mixtures of organic compounds. Instead, one can treat organic molecules as the sum of their functional groups and the influence of each functional group is parameterized (group contribution method). In the Universal Quasi chemical Functional Group Activity Coefficients model (UNIFAC) these parameters are used to calculate the activity coefficient (γ) of each organic compound and water in arbitrary, non-ideal mixture (*Fredenslund et al.* (1977)). It is assumed that the activity coefficient of a molecule i (γ_i) in solution is determined by two separate contributions: the combinatorial (γ_i^C) and the residual (γ_i^R).

$$ln\left(\gamma_i\right) = ln\left(\gamma_i^C\right) + ln\left(\gamma_i^R\right) \tag{2.31}$$

Additionally, it is assumed that the contribution of a functional group to γ_i solely depends on its concentration and the temperature of the system.

Combinatorial contribution

The influence of the molecule size and shape on γ_i is treated in the combinatorial term. The volume r_i and surface q_i of the pure component i is calculated from the normalized van-der-Waals volumes R_k and surfaces Q_k of each functional group k in the molecule weighted with the occurrence of the groups in each molecule ν_k^i.

$$r_i = \sum_k \nu_k^i R_k \tag{2.32}$$

$$q_i = \sum_k \nu_k^i Q_k \tag{2.33}$$

with $k = 1, 2, \cdots N$ number of unique functional groups in mixture

The molar weighted fractional contribution of the molecule i to the total volume and surface of all molecules in the system is given by:

$$V_i = \frac{r_i}{\sum_j x_j r_j} \tag{2.34}$$

$$F_i = \frac{q_i}{\sum_j x_j q_j} \tag{2.35}$$

with $j = 1, 2, \cdots M$ number of unique components in mixture

With this the combinatorial contribution for the molecule i can be calculated. Here z is the coordination number which is set to 10 for all calculations performed in this thesis.

$$ln\left(\gamma_i^C\right) = 1 - V_i + ln\left(V_i\right) - \frac{z}{2}\left(1 - \frac{V_i}{F_i} + ln\left(\frac{V_i}{F_i}\right)\right) \tag{2.36}$$

Residual contribution

The residual contribution is the sum of the difference between the group activity coefficient of a group k of the molecule i in the mixture (Γ_k) and in the pure component i (Γ_k^i).

$$ln\left(\gamma_i^R\right) = \sum_k \nu_k^i \left(ln\left(\Gamma_k\right) - ln\left(\Gamma_k^i\right)\right) \tag{2.37}$$

Γ_k and Γ_k^i depend on the interaction of the different functional groups in the system. These interactions are treated as pair-wise interactions of all functional groups in the system. The energy of interaction of two groups m and n is described with the group interaction parameter Ψ_{mn}.

$$\begin{aligned} \Psi_{mn} &= exp\left(-\frac{U_{mn} - U_{nm}}{RT}\right) = exp\left(\frac{-a_{mn}}{T}\right) \\ \text{with } U_{mn} &\neq U_{nm} \end{aligned} \tag{2.38}$$

This needs to be scaled with the group's surface contribution Θ_m:

$$\Theta_m = \frac{Q_m X_m}{\sum\limits_n Q_n X_n} \tag{2.39}$$

with $n = 1, 2, \cdots N$ number of unique functional groups in the mixture

where X_m is the group mole fraction:

$$X_m = \frac{\sum\limits_j \nu_m^i x_j}{\sum\limits_n \sum\limits_j \nu_n^i x_j} \tag{2.40}$$

with $n = 1, 2, \cdots N$ number of unique functional groups in the mixture
and $j = 1, 2, \cdots M$ number of unique components in the mixture

Hence, Γ_k (and Γ_k^i, respectively) can be calculated.

$$\Gamma_k = Q_k \left[1 - ln\left(\sum_m \Theta_m \Psi_{mk}\right) - \sum_m \left(\frac{\Theta_m \Psi_{km}}{\sum\limits_n \Theta_n \Psi_{nm}}\right)\right] \tag{2.41}$$

Parameters

The UNIFAC approach needs three types of parameters for each functional group: the van-der-Waals volume and surface parameters R and Q and the interaction parameter a_{nm}. These values are tabulated for a wide range of different functional groups. The parameters for the groups used in this study are shown in table 2.1 and 2.2 (*Poling et al.* (2000), *Wittig et al.* (2003)).

Table 2.1: *UNIFAC surface and volume parameters for the functional groups used in this study.*

group main	number sub	name	volume R	surface Q
1	1	CH_3	0.9011	0.848
	2	CH_2	0.6744	0.540
	3	CH_1	0.4469	0.228
	4	C	0.2195	0.000
5	14	OH	1.0000	1.200
7	16	H_2O	0.9200	1.400
9	18	CH_3CO	1.6724	1.448
	19	CH_2CO	1.4457	1.180
10	20	CHO	0.9980	0.948
20	42	COOH	1.3010	1.224

Table 2.2: *UNIFAC group interaction parameters of the functional groups used in this study.*

name (number)	(1)	(5)	(7)	(9)	(10)	(20)
$CH_{0\leq n\leq 3}$ (1)	0	986.5	1318.0	476.4	677.0	663.5
OH (5)	156.4	0	353.5	84.0	-203.6	199.0
H_2O (7)	300.0	-229.1	0	-195.4	-116.0	-14.09
$CH_{2\leq n\leq 3}CO$ (9)	26.76	164.5	472.5	0	-37.36	669.4
CHO (10)	505.7	529.0	480.8	128.0	0	497.5
COOH (20)	315.3	-151.0	-66.17	-297.8	-165.5	0

3. Experimental Set-up

In the first three sections of this chapter the instruments for hygroscopic growth and CCN activation measurement will be described. The hygroscopic growth of aerosol particles was measured with a custom built Hygroscopicity Tandem Differential Mobility Analyzer (HTDMA). As the instrument was designed during my diploma thesis and a detailed description and characterization of the set-up can be found in *Buchholz* (2007), it will be discussed only briefly. For CCN activity measurements three different set-ups were used and will be presented. In the last section of this chapter the simulation chambers will be described. Furthermore, there will be an overview of the experiments performed in these chambers.

3.1 Particle size selection and size measurement

Both the hygroscopic growth and CCN activation measurement have some common features which will be described here. In both instruments the particles are selected by size. For this purpose a Differential Mobility Analyzer (DMA) is employed which uses the fact that a fraction of the aerosol particles is charged. The DMA consists of a metal collector rod centered inside a metal cylinder. The aerosols are introduced at the top and flow down the outer wall of the cylinder. The aerosol flow is separated from the collector rod by a laminar particle free sheath air flow. The rod is maintained at a negative voltage while the outer cylinder is grounded. Thus, an electric field is generated, which influences the charged particles. Positively charged particles are drawn towards the collector rod while they move downwards with the air flow. The position where they reach it depends on their electro-mobility and the applied voltage. By changing the voltage, particles of a different electro-mobility will reach the bottom of the collector rod where they can exit through a small slit. All other particles are discarded. The electro-mobility Z_p is associated to the particle diameter D_p through:

$$Z_p = \frac{neC}{3\pi\mu D_p} \tag{3.1}$$

n : number of charges per particle
e : elementary charge $(1.602 \cdot 10^{-19} C)$
C : Cunningham slip correction
μ : gas viscosity $(1.822 \cdot 10^{-5} \frac{kg}{ms})$

Selecting one electro-mobility class is equal to selecting single charged particles of size D_{p0}, doubly charged particles of size $D_{p1} > D_{p0}$, and so on. A detailed description of treating these multiple charged particles will be given in section 3.3.4.
To measure the size distribution of aerosols the voltage is varied successively, and the number concentration of particles in each size class is determined with a Condensation Particle Counter (CPC). This combination is called Scanning Mobility Particle Sizer (SMPS).
The size calibration for size selection and measuring is done by measuring polystyrene latex (PSL) particles of a known size. The size range is shifted in a way that these particles are detected at the correct size.

3.2 HTDMA

3.2.1 Set-up

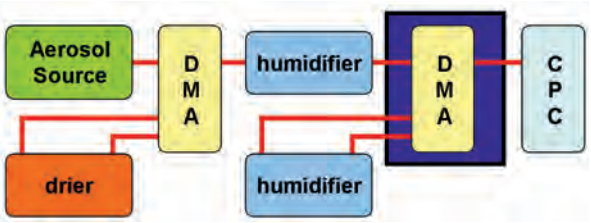

Figure 3.1: *Schematic of the HTDMA.*

The HTDMA consists of two DMA. With the first DMA a narrow size distribution is selected out of the polydisperse aerosol. The size selected aerosol and the sheath air of the second DMA are humidified at room temperature (25 - 30°C depending on the surroundings) to almost the same relative humidity (RH) with the sheath air being at slightly higher RH. The second DMA is placed in an insulated box and cooled to 20°C. Before entering the second DMA both aerosol and sheath air are cooled down to the same temperature and thus, the RH increased to its final value. The residence time of the air in this cooled area before entering the second DMA is 30 sec for the aerosol containing air and 5 sec for the sheath air. This second DMA measures the size of the particles (i.e. works as a SMPS). The hygroscopic growth factor (GF) is calculated as the ratio of the size of the wet particle (D_{wet}) and the selected dry size (D_{dry}).

$$GF = \frac{D_{wet}}{D_{dry}} \tag{3.2}$$

To determine the exact RH inside the second DMA, Vaisala HMP235 sensors measure the RH and temperature outside the insulated area (T_{ext}). The temperatures of the air flows inside the insulated area (T_{int}) are measured with PT100 sensors directly before or after they entered or left the DMA. First the saturation vapor pressure of water (p_{sat}) in Pascal (Pa) at a certain temperature T in Kelvin

is calculated with equation 3.3 (*Hyland and Wexler* (1983)):

$$\begin{aligned} p_{sat}(T) = exp(\quad & - \quad 0.5800 \cdot 10^4 \cdot K/T \\ & + \quad 1.3915 \\ & - \quad 0.0486 \cdot T/K \\ & + \quad 0.4176 \cdot 10^{-4} \cdot T^2/K^2 \\ & - \quad 0.1445 \cdot 10^{-7} \cdot T^3/K^3 \\ & + \quad 6.5460 \cdot log(T/K)) \; Pa \end{aligned} \tag{3.3}$$

Multiplying the vapor pressure with the measured RH gives the absolute humidity (AH):

$$AH(T) = RH(T) \cdot p_{sat}(T)/100\% \tag{3.4}$$

Assuming that the AH is the same throughout the instrument (no major losses) the RH inside the second DMA is then the ratio of the AH at T_{ext} and p_{sat} at T_{int}.

$$RH(T_{int}) = \frac{AH(T_{ext})}{p_{sat}(T_{int})} \cdot 100\% \tag{3.5}$$

3.2.2 Calibration

The calibration of the RH-measurement of the HTDMA is done by comparing ammonium sulfate ($(NH_4)_2SO_4$) aerosol measurements with the theoretical growth curve for this salt. For at least five different GF the measured and theoretical RH are read from the humidogram. To these a linear, quadratic, or cubic polynomial is fitted. The obtained parameters are used as correction factors. Which type of polynomial is used depended on the data and is decided by the user. For some data sets the best result is achieved by looking at RH higher than 90% separately. Hence, two sets of correction parameters are determined.
During a measurement campaign these calibration measurements were performed every three to seven days. For each campaign (up to 6 weeks long) one set of correction parameters could be used. No major continuous drift was observed.

3.2.3 Measurement errors

The measured size distribution is fitted with a asymmetric log-normal distribution.

$$\frac{dN}{dln(D_p)} = P_0 \cdot exp\left(-ln^2\left(\frac{1 + (ln(D_p) - P_1) \cdot (P_3^2 - 1)/(P_2 \cdot P_3)}{ln(P_3)}\right)\right) \tag{3.6}$$

P_i : fitting parameters

For all further calculations (e.g. GF) only the position of the maximum of this distribution is of interest. This can be deduced directly from P_1:

$$D_p = exp(P_1) \tag{3.7}$$

Hence, the error of the particle size can be calculated from the 1 σ error of the fitted parameter with Gaussian error propagation:

$$\sigma(D_p) = \pm\, \sigma(P_1) \cdot exp(P_1) \tag{3.8}$$

The error of the GF calculated with equation 3.2 is then given by:

$$\sigma(GF) = \pm \sqrt{\left(\frac{\sigma(D_{wet})}{D_{dry}}\right)^2 + \left(\frac{\sigma(D_{dry}) \cdot D_{wet}}{D_{dry}^2}\right)^2} \tag{3.9}$$

The accuracy of the RH-sensors is stated to be $\pm$ 1% RH below 90% RH and $\pm$ 2% RH above 90% RH. As the sensors are placed outside the cooled area, the maximum RH they experience is well below 90%. The accurracy of the T sensors is 0.1°C. From equations 3.4 and 3.5 follows with Gaussian error propagation:

$$\begin{aligned}\sigma(RH_{int}) = \pm\ & \sqrt{\left(\frac{\sigma(RH_{ext}) \cdot p_{sat}(T_{ext})}{p_{sat}(T_{int})}\right)^2} \\ & \overline{+\left(\sigma(T_{ext}) \cdot \frac{\partial}{\partial T_{ext}}\left(\frac{RH_{ext} \cdot p_{sat}(T_{ext})}{p_{sat}(T_{int})}\right)\right)^2} \\ & \overline{+\left(\sigma(T_{int}) \cdot \frac{\partial}{\partial T_{int}}\left(\frac{RH_{ext} \cdot p_{sat}(T_{ext})}{p_{sat}(T_{int})}\right)\right)^2}\end{aligned} \tag{3.10}$$

Calculating this reveals that the term depending on $\sigma(RH_{ext})$ is two dimensions bigger than the other two terms. Thus, equation 3.10 can be simplified to:

$$\sigma(RH_{int}) = \pm \frac{\sigma(RH_{ext}) \cdot p_{sat}(T_{ext})}{p_{sat}(T_{int})} \tag{3.11}$$

The calculated accuracy for the internal RH is between 1.4 and 1.8% RH depending on the RH.
As the size measurement takes 2 to 3 minutes, the RH may change in this interval. The RH is measured continuously, so the standard deviation in each size measurement interval can be calculated. Data points with a standard deviation higher than 0.5% are regarded as "bad data points" and omitted.

3.3 CCN-Counter

3.3.1 Working principle

In a Cloud Condensation Nuclei Counter (CCN-C) aerosol particles are exposed to a set super-saturation (SS) and the number of particles that become cloud droplets is counted. To create this SS, the fact is used that the diffusion of water vapor in air is faster than the diffusion of heat in air (*Roberts and Nenes* (2005)). In figure 3.2 a schematic cross section of the column in the CCN-C is shown. The walls of the column are wetted with water which evaporates and diffuses inwards. At point 3 on the center line the water vapor pressure is equal to that at point 2 on the wall but the temperature is equal to that at point 1.

As there is a positive temperature gradient, the temperature at point 1 is lower than at point 2. Consequently, the saturation vapor pressure at point 1 is also lower. Therefore, there is a super-saturation at point 3. Enclosed in a laminar sheath air flow, the aerosol flows at the centerline of the column and is exposed to this SS. The actual magnitude of the SS depends on the temperature gradient and the air flow in the column. At the end of the column an optical particle counter detects all particles bigger than 750 nm. As the inserted dry particles are much smaller than 750 nm, only the activated particles (CCN) are counted. This set-up of a continuous flow temperature gradient CCN-C was first proposed by *Roberts and Nenes* (2005) and has been made commercially available by Droplet measurement Technologies (DMT).

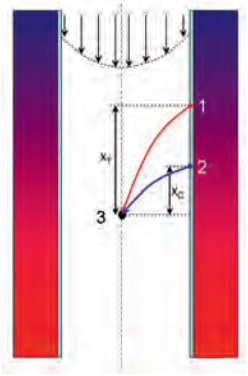

Figure 3.2: *Schematic cross section of CCN-C column adapted from figure 3 in Roberts and Nenes (2005).*

3.3.2 Set-up

From the CCN-C the activated particle concentration at a set super-saturation is received. But to measure the activation behavior of aerosol particles, the ratio of CCN to all particles (CN) (activated fraction a_f, see equation 3.12) is needed. So, the total particle concentration is measured with a CPC.

$$a_f = \frac{CCN}{CN} \tag{3.12}$$

The CCN activation of aerosol particles depends on both the dry particle diameter and the prevailing SS (see figure 3.3). Thus, measurements are either conducted at constant SS tuning the dry particle diameter, or for a constant particle size the SS is changed. A third option is to use the polydisperse aerosol and determine at which dry size the observed activated fraction is reached. In all cases a pair of so called critical SS and $D50$ is obtained. The methods used to measure the presented data are described below.

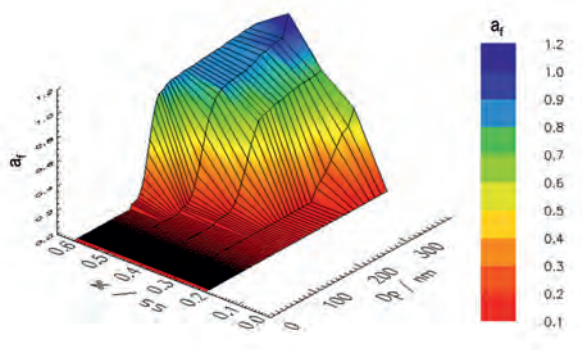

Figure 3.3: *Size and SS dependence of the activated fraction.*

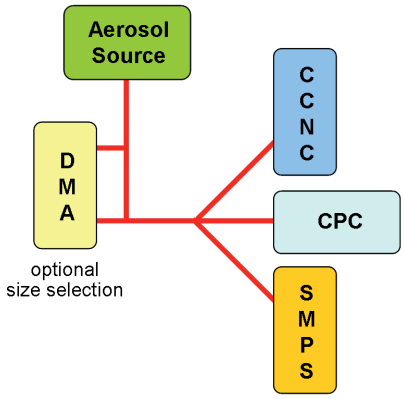

Figure 3.4: *Schematic of the general CCN-C set-up. For polydisperse measurements the DMA is by-passed, for size-scanning measurements no SMPS is needed.*

Single size selecting CCN-C measurements

The basic set-up of the CCN-C assembly is shown in figure 3.4. With a DMA a narrow size distribution is selected out of the polydisperse aerosol and distributed to a CPC, CCN-C, and a SMPS. The SMPS is solely there to check the selected size. The CCN-C steps through at least five SS, and for each step the a_f is calculated. Plotting the a_f vs. the SS results in a sigmoid activation curve which is fitted with a Gaussian error function (equation 3.13 with $x = SS$). The turning point (P_2) of this curve gives the critical SS for particles of the selected diameter. This set-up allows to investigate a chosen particle size.

$$a_f = \frac{P_0}{2 \cdot \left(1 + \mathrm{erf}\left(\frac{x - P_1}{P_2 \cdot \sqrt{2}}\right)\right)} \tag{3.13}$$

P_i : fitting parameters
erf: Gaussian type error function

Size scanning CCN-C measurements

For the size-scanning method the same set-up as for single size selection measurement is used, but without the SMPS system (see 3.4). The DMA is scanned between 10 and 450 nm while the SS remains constant, i.e. it is operated as a SMPS using an interval of 2 or 3 min for every full size scan. For each selected particle size the CN and CCN concentrations are measured.
Before the a_f can be calculated, the measured CN and CCN concentration must be corrected for multiple charged particles. As the DMA selects the electromobility diameter, multiple charged particles with accordingly larger diameters enter the CCN counter. The fraction of these particles pretends activation at small diameters. To separate the single from the multiple charged particles, the fraction of multiple charged particles is calculated according to a natural charge distribution using the measured size distribution (see chapter 3.3.4). Then, a_f is determined for each charge class separately and fitted with a Gaussian error function (equation 3.13 with $x = D_p$). The turning point of this function is the $D50$ at the set SS. This new method of CCN-C measurement was developed during this thesis. A detailed description and characterization can be found in *Strathmann* (2009).

Polydisperse CCN-C measurements

If the polydisperse aerosol is used without size selection, a SMPS is needed in addition to CPC and CCN-C to measure the aerosol size distribution. It is assumed that the aerosol particles are internally mixed (the chemical composition of all particles is the same). Thus, bigger particles will activate before the smaller ones. The calculated a_f is compared to the cumulative size distribution starting from the maximum diameter. The size, at which the cumulative size distribution equals a_f, is defined as $D50$.
Size measurements with the SMPS take 2 to 3 minutes. The particle concentrations measured by CPC and CCN-C are averaged over this interval. This method allows to use the full size distribution.

3.3.3 Calibration

Activation efficiency calibration

The activated fraction is the basis for all further calculations. Therefore, the activation efficiency (AE) of the CCN-C must be determined. In this study the AE is defined as the a_f of $(NH_4)_2SO_4$ aerosol at 1% SS. At this SS in the CCN-C the $D50$ of $(NH_4)_2SO_4$ particles is 29 nm (i.e. at a dry particle size of 29 nm 50% of the particles are activated). Hence, in the size range interesting for the measurements (40 - 200 nm) all particles should be activated and counted in the CCN-C ($AE = 1$). The lower cut-off of the used CPC is 2.5 nm. The AE is investigated for dependence on particle size and concentration using the single size selection method. There was no dependency of the AE on the particle concentration as long as the concentration was below 8000 particles per cm^3. Between 60 and 200 nm the AE was independend of particle dry size. From 60 to 40 nm the AE decreases by 0.05 - 0.1 with decreasing diameter.

Even if all particles are activated in the CCN-C, the AE can be unequal 1. This is the case if the number of particles reaching the CCN-C and CPC is not exactly the same (e.g. higher particle loss in one pathway due to longer tubing, more bends, etc.). With the procedure described above the "effective" AE is measured, which contains both effects. To correct the measured data, the a_f is divided by this "effective" AE measured every 3 to 5 days during a campaign. The AE was 0.9 - 1.0 for both, the SAPHIR campaign and the JPAC campaign.

SS calibration

No matter which measurement method is chosen, a calibration of the SS set in the CCN-C is necessary. At a constant sample flow the SS is proportional to the temperature difference between the top and bottom of the column (ΔT). The SS is calculated by the CCN-C software using the set ΔT. Due to physical limitations (e.g. the temperature cannot be measured inside the column) the calculated SS never exactly represents the true SS inside the column. Therefore, $(NH_4)_2SO_4$ aerosol is measured either with the single size selection or the size scanning method to determine the $D50$ and SS_{crit}. A set of measured data is shown in figure 3.5 (green dots). The theoretical values for $(NH_4)_2SO_4$ calculated with the parameters given in *Rose et al.* (2008) (parameter set: OS) are shown as red line. For each data point the theoretical SS_{th} was determined. By performing a linear fit to the theoretical vs. measured data the correction factors were obtained.

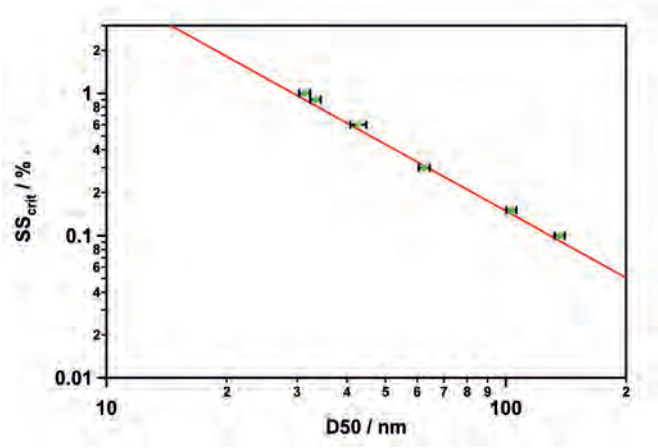

Figure 3.5: *Measured (green) and theoretical (red) activation data for $(NH_4)_2SO_4$ aerosol, error bars are width of size bin in SMPS/DMA selection*

$$SS_{th} = A + B \cdot SS_{crit} \tag{3.14}$$

During a measurement campaign this calibration was performed every 3 to 7 days (with at least three sizes for the single size selection method). No significant trend was observed during each campaign (3 to 6 weeks long), and the same correction factors could be used for the whole data set.

Size calibration

The size measurement of the SMPS system is calibrated with PSL particles of a known size. The size selection with the DMA is then checked with the previously calibrated SMPS.

3.3.4 Correction for multiple charged particles

Whenever a DMA (or SMPS) is used for size selection, the possible influence of multiple charged particles must be considered. For the single size selection method the contribution of multiple charged particles in the selected aerosol is constant during the whole measurement. Therefore, it can be subtracted as an offset. For measurement of the polydisperse aerosol no additional correction is needed as the SMPS software provides multiple charge correction automatically. For the size scanning method a more detailed treatment is needed. First the fraction of particles with n positive charges are calculated for each selected particle size with the Fuchs-Boltzmann distribution (*Wiedensohler* (1988), *Gunn and Woessner* (1956)):

$$ln\left(f_n^0(D_p)\right) = ln\left(\frac{e}{\sqrt{4\pi^2\epsilon_0 D_p kT}}\right) - \frac{\left(n - \frac{2\pi\epsilon_0 D_p kT}{e^2} \cdot ln(r)\right)^2}{\frac{4\pi\epsilon_0 D_p kT}{e^2}} \tag{3.15}$$

$f_n^0(D_p)$	: fraction of particles of the size D_p with n charges	
D_p	: particle diameter	
n	: number of charges per particle	
e	: elementary charge	$(1.602 \cdot 10^{-19} C)$
k	: Boltzmann constant	$(1.38 \cdot 10^{-23} J/K)$
ϵ_0	: vacuum permittivity	$(8.85 \cdot 10^{-12} F/m)$
r	: ion mobility	(0.875)

Only these charged particles can pass the DMA. So the contribution of each charge class to the selected aerosol $f_n(D_p)$ is given by:

$$f_n(D_p) = \frac{f_n^0(D_p)}{\sum_{n=+1}^{+4} f_n^0} \tag{3.16}$$

Single charged particles are present for all particle sizes. With increasing diameter the fraction of particles increases that are carrying more than one elementary charge. The distribution of charges for a given size distribution can be reconstructed. To start the calculation, a particle size class is needed where it is ensured that only single charged particles contribute to this size class. This is usually the size class with the largest diameter if an impactor is used, which cuts off particles by their aerodynamic size. Due to instrumental set-up the largest particles entering the DMA are 450 nm (D_{p1}) independent of the charge. This size class contributes doubly charged particles to the size class with diameter 269 nm (D_{p2}), triply charged to 204 nm (D_{p3}), and quadruply charged to 170 nm

(D_{p4}). This also means that there are no contributions of doubly charged particles at diameters larger than 269 nm, no contributions of triply charged particle at diameters larger than 204 nm etc. Particles carrying more charges make up less than 1% of all charged particles at this size. Thus, they are neglected in the following. First the total number of charged D_{p1} particles ($CN_{all}(D_{p1})$) is calculated from the measured total particle number at this size ($CN_{meas}(D_{p1})$) using the fractions calculated with equation 3.16:

$$CN_{all}(D_{p1}) = \frac{CN_{meas}(D_{p1})}{f_I(D_{p1})} \tag{3.17}$$

Therefore, the number of D_{p1} particles with n charges ($CN_n(D_{p1})$) is given by:

$$CN_n(D_{p1}) = CN_{all}(D_{p1}) \cdot f_n(D_{p1}) \tag{3.18}$$

Starting at $D_p = D_{p2}$ the number of single charged particles $CN_I(D_p)$ can be calculated by subtracting the sum of multiple charged particles from the measured value:

$$CN_I(D_p) = CN_{meas}(D_p) - \sum_{n=+2}^{+4} CN_n(D_{pn}) \tag{3.19}$$

D_{pn}: size of n charged particles detected at D_p

As the triply charged particles occur only below D_{p3} and quadruply charge particles only below D_{p4} their contribution to equation 3.19 is zero above these diameters. Repeating equations 3.17 to 3.19 subsequently moving one size class lower with each step allows to calculate the size spectra of single to quadruply charged particles.
The same correction needs to be performed for the number of activated particles detected with the CCN-C. As stated above, all particles detected between D_{p1} and D_{p2} are single charged. Thus, the activated fraction of single charged particles at those diameters is simply the ratio of measured CCN_{meas} and CN_{meas}:

$$a_{fI}(D_p) = \frac{CCN_{meas}(D_p)}{CN_{meas}(D_p)} \tag{3.20}$$

As the activation does not depend on the electro-mobility diameter but on the geometric diameter, the activated fraction for a multiply charged particle is the same as for the corresponding single charged particles of diameter D_{pn}. Therefore, the number of multiple charged CCN at a given size D_p can be calculated by multiplying the number of multiple charged CN (determined with equation 3.17 to 3.19) with the activated fraction for the corresponding size D_{pn} (calculated with equation 3.20):

$$CCN_n(D_p) = CN_n(D_p) \cdot a_{fI}(D_{pn}) \tag{3.21}$$

D_{pn}: size of n charged particles detected at D_p

Subtracting the obtained amount of multiple charge CCN from the measured number gives the number of single charged CCN at this size.

$$CCN_I(D_p) = CCN_{meas}(D_p) - \sum_{n=+2}^{+4} CCN_n(D_p) \tag{3.22}$$

Then the activated fraction for each charge class can be calculated with:

$$a_{fn}(D_p) = \frac{CCN_n(D_p)}{CN_n(D_p)} \tag{3.23}$$

Starting from the highest size class repeating equations 3.20 to 3.23 will lead to an activation curve for each charge class. These curves can be fitted separately with equation 3.13 to determine $D50$.

3.3.5 Measurement errors

Systematic errors

As shown in section 3.3.3, both the systematic errors of the a_f and the SS are accounted for by calibration procedures. Therefore, the accuracy of a_f and SS are determined by the accuracy of these calibrations.
The a_f is corrected by scaling it with the AE. The AE differs 0.05 - 0.2 (depending on the set-up) from the expected value of 1. But the variation (precision) for each set-up is smaller ± 0.05.
The correction parameters for the set SS are found by fitting the SS_{crit} measured for several $D50$ to the theoretical SS_{th} at those $D50$ (see equation 3.14). The error of the SS_{th} associated with each measured SS value depends on the error of $D50$ selected or determined (for single size selection and size scanning method, respectively). The width of a size bin in the SMPS is chosen as $\sigma(D50)$ (±(1 - 10) nm for 30 - 170 nm). This corresponds to a variation in the calculated SS_{th} of 0.05 - 0.001% for 0.09 - 1.0% SS. Using theses errors in the fitting procedure, the error of the corrected SS_{corr} depends on the errors for the fitting parameters ($\sigma(A)$ and $\sigma(B)$).

$$\sigma(SS_{calc}) = \sqrt{(SS_{crit} \cdot \sigma(B))^2 + \sigma(A)^2} \tag{3.24}$$

This leads to errors of ±0.01 - 0.02% for the investigated SS of 0.09 - 1.0%.

Statistic errors

For all measurement methods the data is averaged over each set SS. For polydisperse and size scanning measurements at least three scans are performed for each SS step. The $D50$ is determined for each scan and then averaged. Within the significant digits the same result is obtained if the spectra are averaged first and the mean $D50$ is calculated afterwards. For the single size selected method each SS step is held for 4 to 6 minutes, and the calculated a_f is averaged over this period. The standard deviation of a_f is used for the fitting of the activation curve with equation 3.13. Then the error of the determined SS_{crit} is the fitting error for the turning point of the curve.

3.4 Measurements of the chemical compositions of aerosol particles

During this study two different instruments measured the chemical composition of the formed aerosol particles: A High Resolution Time-of-flight Aerosol Mass Spectrometer (HR-Tof-AMS, Aerodyne Research Inc., Massachusetts) and an Atmospheric Pressure Chemical Ionization Mass Spectrometer (APCI-MS).

3.4.1 HR-Tof-AMS

The HR-Tof-AMS measures quantitatively the particle-size-resolved chemical composition of aerosol particles in the sub micron size range (*Jayne et al.* (2000)). The aerosol particles are focused into a narrow beam with an aerodynamic lens system. This beam enters a high vacuum chamber ($< 10^{-5} hPa$) reducing the gas phase by a factor of 10^7. At the end of the chamber the particles impact on a heated surface (600°C) where they are flash-evaporated. The evaporated compounds are ionized by electron impact (70 eV) and the resulting ions are detected with time-of-flight mass spectrometry. Due to the "hard" ionization method organic compounds show a high degree of fragmentation and usually the mother ions cannot be detected. But the resolution is high enough to distinguish between fragments containing only carbon and hydrogen atoms and oxygenated fragments. Analyzing all fragments and summing all oxygen and carbon atoms in all occurring fragments leads to the O/C ratio. A detailed description of the instrument and the data analysis is given by *Spindler* (2010).
Besides the chemical composition the particle size is also measured. The super sonic expansion of the particle beam into the vacuum chamber leads to size dependent velocities of the particles. Therefore, the particles reach the detector depending on their size. By periodically blocking the beam with a rotating wheel chopper, a common start time for the particle-time-of-flight measurement is created and size dependent mass spectra can be measured. By comparing the measured flight time with those of particles with a known size, the vacuum aerodynamic diameter (D_{ae}) of the particles is determined. Assuming spherical particles, the effective density of the aerosol particles can be calculated from the ratio of D_{ae} and the electro-mobility diameter D_p measured with the SMPS (section 3.1):

$$\rho_p = \frac{D_{ae}}{D_p} \tag{3.25}$$

3.4.2 APCI-MS

Unlike the HR-Tof-AMS the APCI-MS ionizes the sample at atmospheric pressure. Before entering the instrument, the VOCs in the gas phase are removed in a charcoal denuder. Inside the APCI-MS the particles are evaporated at 350°C and the vapors are chemically ionized. With a corona discharge primary ions are produced from nitrogen, oxygen and water molecules in the gas phase. Through proton transfer reactions the analyte molecules are ionized and can be detected in a mass spectrometer. As this chemical ionization is a much "softer" ionization method than electron impact, fragmentation of the mother ions is almost com-

pletely suppressed. Therefore, the resulting mass spectra represent the molecular mass distribution in the particles and an average molecular mass can be derived. The instrument and the measured data are described in detail in *Reinnig* (2009).

3.5 Chambers

3.5.1 The SAPHIR-chamber

Set-up

Figure 3.6: *Picture of the atmospheric simulation chamber SAPHIR.*

The aging of SOA particles was investigated in the atmospheric simulation chamber SAPHIR in the Research Center Jülich. This FEP-Teflon chamber has a volume of approx. 270 m^3 and is operated with high purity synthetic air (quality 6.0). During experiments a small constant flow of synthetic air through the chamber is maintained to compensate for sampling and leakage. Trace gases (such as water, O_3, CO, NO_x, VOCs, etc.) can be added to the chamber within this flow. Aerosols can be sprayed directly into the chamber with an aerosol generator. Photochemistry inside the chamber is triggered by natural sunlight (light transmission 85% when the roof is open). By keeping the roof closed, experiments under "dark" conditions are also possible.
The gas and particle phase inside the chamber are monitored with a set of different instruments. Here we list only those providing data directly used in this study. A detailed description of the chamber can be found in *Bares* (2003). Routinely, the standard measurements of temperature, pressure, RH, O_3, NO_x, and OH were conducted. VOCs and reaction products in the gas phase were measured with a Gas Chromatograph Mass Spectrometer (GC-MS) and a proton transfer reaction mass spectrometer (PTR-MS). A HR-Tof-AMS and a APCI-MS monitored the chemical composition of particle phase. The microphysical properties of the aerosol particles were measured with the HTDMA and the CCN-C system as described above.

Typical experiment

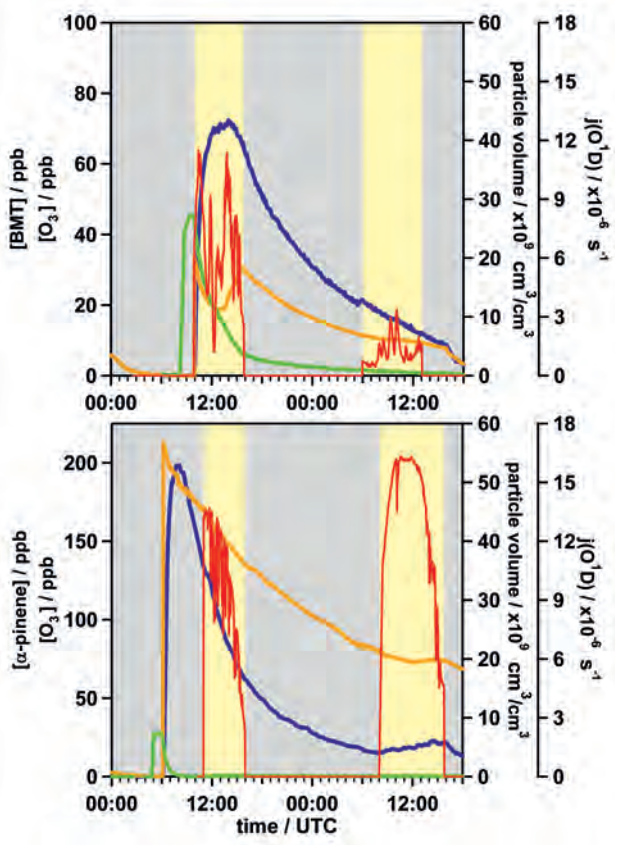

Figure 3.7: *Time series of a typical experiment in SAPHIR. Top panel: type A experiment, bottom: type B (see text), gray background indicates closed chamber roof, yellow background indicates open roof. Orange: O_3 mixing ratio, green: MT mixing ratio, blue: total particle volume, red: photolysis rate (j) of O_3 to $O(^1D)$.*

In the SAPHIR chamber two different types of experiments were conducted. For both types the clean, dark chamber was humidified and the VOCs were added (green squares in Figure 3.7). The chamber was considered "clean" if the trace gases and the particle concentration was below the detection limit of the used instruments. All experiments were conducted at low NO_x concentrations (less than 2 ppb). The gas phase was assumed to be well mixed if the MT concentration was stable (after approx. 1h). Then O_3 was added (orange). In experiment type B the chamber roof stayed closed for another 5h. The VOCs and O_3 reacted (ozonolysis), and aerosol particles (blue) were formed shortly after the O_3 addition. Then the roof was opened and photochemistry started. OH radicals were formed by the reaction of $O(^1D)$ from photolysis of O_3 with water vapor and by photolysis of traces of HNO_2, which are always present in the chamber. No new particle formation was observed, but the total aerosol mass increased. This is

superimposed by the dilution of the chamber due to the constant experimental flow. In experiment type A the chamber roof was opened directly after O_3 was added. Thus, both ozonolysis and photochemical processes took place from the beginning. As in type B aerosol particles were formed shortly after the O_3 addition / roof opening. For both experiment types the chamber roof was closed over night and opened again in the morning of the second day. After another 10 h reaction time the experiment was stopped and the chamber was flushed with synthetic air. The different variations of these general experiment types are described in the next section.

List of experiments

In table 3.1 the experiment conditions in SAPHIR are shown. As gas phase precursors α-pinene or a 1:1 mixture of five MT were used. This boreal monoterpene mix (BMT) consisting of α-pinene, β-pinene, limonene, ocimene, Δ-3-carene was identified as main constituent of emissions from boreal tree species in previous JPAC studies (see next section). As a variation to the BMT mix ocimene was left out or 15% sesquiterpenes were added (SQT - here α-farnesene and α-humulene). In the 3 x 40 ppbC experiment the roof was opened after the addition of the first 40 ppbC of BMT. The second and third 40 ppbC portion were added at 2 h interval.

Table 3.1: *Experiments conducted in SAPHIR. BMT: boreal monoterpene mix, b: bright, c: cloudy. For further details see text above.*

exp #	VOCs	[VOC] [ppbC]	[O_3] [ppb]	type	radiation conditions	comment
3,5	BMT	1000	60	A	b/b, c/c	
8	BMT	1000	200	B*	-/-	dark chamber
1	BMT	500	60	A	b/c	
11	BMT	3 x 40	60	A	b/b	
6	BMT - ocimene	1000	60	A	c/b	
2	BMT - ocimene	500	60	A	b/c	
4,7	BMT + SQT	1000 + 75	60	A	c/c, b/c	
9	none	0	60	A	b/b	
20	α-pinene	100	200	B	b/dark	
21	α-pinene	400	200	B	b/b	
22	α-pinene	400	200	B	b/b	dry chamber
23	α-pinene	400	200	B	b/b	300 ppm CO

In the column "type", B indicates that the VOCs first reacted only with O_3 for 5 h before the chamber roof was opened, and A that the roof was opened as soon as the O_3 was introduced. Experiment 8 (type B*) was conducted completely in the dark chamber. The photolysis rate of O_3 to $O(^1D)$ ($j(O(^1D))$) is used to categorize the radiation conditions on the first and second day of the experiment. $j(O(^1D)$ above $10^{-5}s^{-1}$ is considered bright (b) and $j(O(^1D))$ below $10^{-5}s^{-1}$ cloudy (c). The BMT experiments were part of the EUCAARI and the α-pinene ones were part of the MUCHACHAS campaign.

3.5.2 The Juelich Plant Atmosphere Chamber

Set-up

Experiments to investigate SOA formed from natural gas phase precursors were conducted in the Juelich Plant Atmosphere Chamber (JPAC). The schematic set-up is shown in Figure 3.8. The chamber has been described in detail previously in *Mentel et al.* (2009).

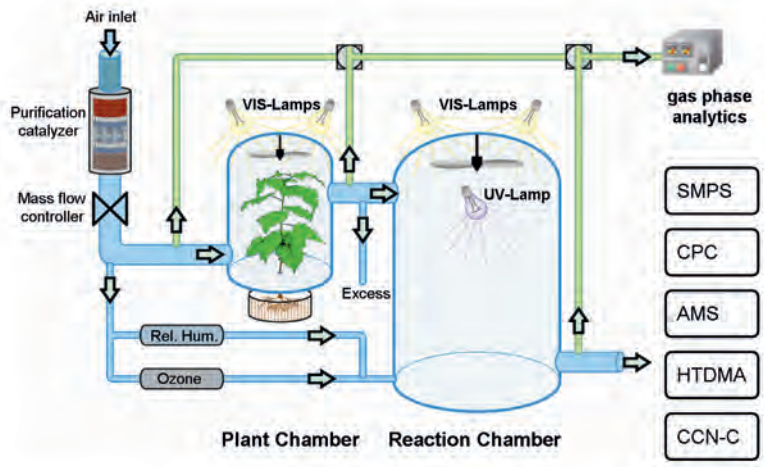

Figure 3.8: *Schematic of Juelich Plant Atmosphere Chamber.*

JPAC consists of three large glass chambers (164 L, 1150 L, and 1450 L) each in a separate climate-controlled housing. The two smaller chambers were used as plant chambers (PC) while the biggest served as reaction chamber (RC). The PCs were illuminated with discharge lamps mimicking the solar spectrum and providing a day-night cycle for the plants. Purified air (particle, VOC, NO_x and ozone free) with a constant CO_2-level around 350 ppm flowed through the PC. With this flow VOCs emitted by the plants were transferred into the RC. Besides the flow from the PC, two additional air streams supplied the RC with ozone (approx. 90 ppb) and water vapor. By controlling the humid air stream the *RH* in the RC was held at constant (65±2) % . Inside the RC a UV lamp was placed to produce OH radicals. Ozone was photolized and the produced O^1D radicals reacted with the water vapor forming OH radicals. The residence time of air in the chambers was approx. 65 min in the RC and between 5 to 20 min in the PC (depending on the chamber size).
The VOCs entering and leaving the RC were monitored with a GC-MS and a PTR-MS. The OH concentration was calculated from the MT consumption. The particle formation was measured with an Ultrafine CPC (TSI Model 3025) and a SMPS system (TSI Model 3070 + 3022A) and the chemical composition of the particle phase was investigated with a HR-Tof-AMS. An HTDMA and CCN-C (as described above) were used to measure the microphysical properties of the particles.

Typical experiment

In Figure 3.9 a typical experiment is shown. In this Figure the monoterpenes (MT) are shown as representative for all VOCs (dark green squares, right axis). At night the VOC emissions coming from the plants were low. Consequently, the concentration in the RC was also low (light green squares). When the lights in the PC were switched on (indicated by yellow background), the emissions increased, and the ozone concentration (orange line, left axis) decreased due to ozonolysis of the VOCs. But no particles were formed at this stage (blue diamonds, left axis). When the MT concentration in the RC stabilized (around noon), the UV-lamp was turned on and OH radicals were produced. The produced OH concentration (red triangles, right axis) is calculated from the consumption of deuterated cyclohexane, an added tracer reacting only with OH. The MT in the reaction chamber was completely consumed and the particle formation started. After the UV was switched off, there was no more OH to react with the MT whose concentration increased again. The particle production stopped and the remaining particles were flushed out. In two experiments the general procedure was varied slightly by leaving the lights in the PC turned off.

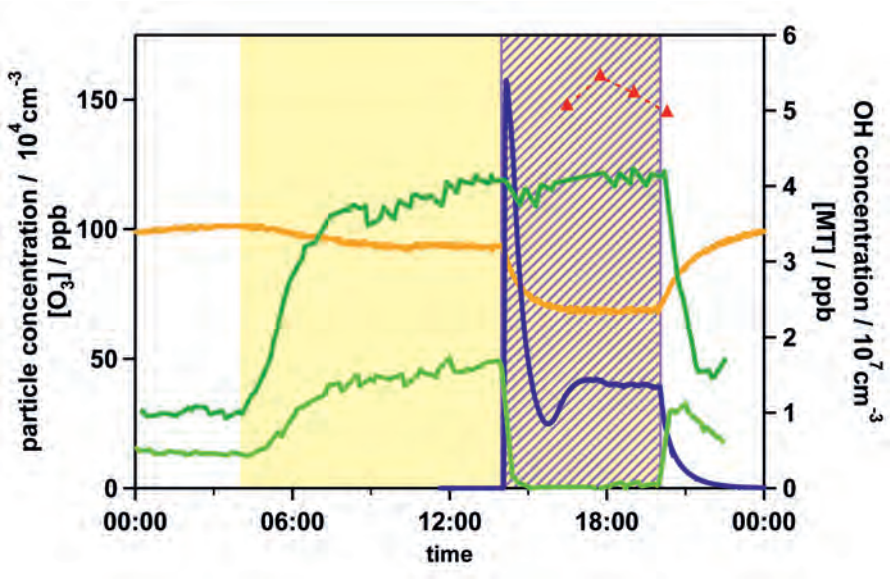

Figure 3.9: *Time series of a typical experiment in JPAC. Yellow background indicates lights on in the PC, violet indicates UV lamp on in RC. Orange line: O_3 mixing ratio, red triangles: OH concentration, blue line: particle number concentration, and dark and light green line: MT coming from the PC and leaving the RC,respectively.*

The size distribution of the formed particles is shown in Figure 3.10. The first nucleation shortly after the UV was switched on produced a narrow, fast growing mode. As these particles were flushed out, after 2 - 3 h the available surface could no longer take up the continuously produced, condensable vapors and a second, quasi-continuous nucleation occurred. Another 3 h later this very wide

mode dominated the particle mass. For each experiment the HTDMA measured at least one full humidogram for each of the two particle modes. The CCN-C ran continuously in polydisperse mode.

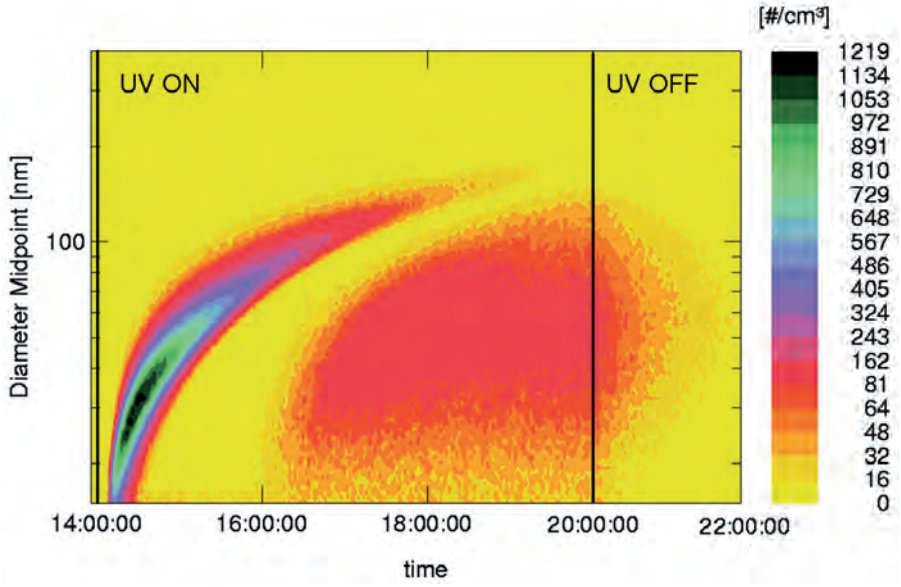

Figure 3.10: *Particle size distribution of a typical experiment in JPAC.*

List of experiments

In table 3.2 the experiment conditions are listed. A small mixed boreal stand was used in the PC consisting of 2 pines (pinus sylvestris), a spruce (picea abies), and a birch (betula pendula). The temperature in the RC was constant and the temperature of the PC was used to vary the VOC emissions. Each experiment type was performed at least twice.
These experiments were part of the EUCAARI campaign.

Table 3.2: *Experiments conducted in JPAC. The boreal stand consisted of 2 pines (pinus sylvestris), a spruce (picea abies), and a birch (betula pendula).*

Plants	VOCs [ppbC]	ozone [ppb]	T(PC) [°C]	T(RC) [°C]	vis lamps [UTC]	UV lamp [UTC]
boreal	85	90	15	15	2:00	12:00
boreal	380	90	20	15	2:00	12:00
boreal	240	90	25	15	2:00	12:00
boreal	730	90	30	15	2:00	12:00
boreal	120	90	35	15	off	12:00

4. Results

In this chapter the results obtained from hygroscopic growth and CCN activation measurements will be presented. Both, the measured CCN activation and hygroscopic growth data, will be converted into the parameters κ, ϕ and ρ_{ion}. Since κ will be used in chapter 5 to investigate trends in the data, the errors resulting from the measurement uncertainties will be discussed briefly.

4.1 CCN-C data

During the BMT experiments the CCN-C measurements were performed both in single-size selecting and polydisperse mode. During the α-pinene experiments (# 20 - 22) the size scanning method was used. Despite the different measurement methods, all data can be presented as SS_{crit} vs. $D50$ plots with the time scale of each experiment as color code (see appendix A.1). Equation 2.29 is used to fit the data and calculate the parameters ρ_{ion} , ϕ, and κ. Since the measurement errors are considered in the fit, the error of the derived parameter can be calculated from the 1 σ error of the fit parameter. For $\sigma(\kappa)$ Gaussian error propagation leads to:

$$\sigma(\kappa) = \sigma(p_0) \cdot \frac{2.56 \cdot 10^6 M_w^3}{27 R^3 T^3 \rho_w^3} \cdot \sigma^3 \cdot {p_0}^{-3} \tag{4.1}$$

The ρ_{ion} and ϕ can be treated accordingly. Since κ, ρ_{ion} , and ϕ are directly related by equations 2.13 and 2.24, their relative errors are the same. For all measurements the relative errors were between 2% and 7%.

4.1.1 SAPHIR data

The measured $SS_{crit}/D50$ data was fitted with equation 2.29 using a fixed exponent of -1.5. Additionally, the data was fitted with the same equation, but with the exponent as a second parameter. In almost all cases the exponent derived in this "free" fit was -1.5±0.05. This showed that the assumption made to derive equation 2.29 were valid. In Table 4.1 the fit parameter p_0 (for fits with -1.5 as exponent) and the deduced parameters are displayed for all experiments conducted in SAPHIR. If sufficient data was available, full time series were divided into three subsets and fitted individually. Ia is the data of the first 6 h of the experiments and II the data of the second day. As in experiment 11 the BMT was added in three portions, here Ia is the measurement until the second portion was added. For # 20 - 22 Ia is the data until the roof was opened (approx. 5 h) and Ib the data after the opening. To calculate κ and ρ_{ion} from the fit parameter, the surface tension of pure water was assumed (0.072 N/m). For the conversion

of ρ_{ion} into ϕ, a molecular weight of the solute of 200 g/mol and a density of 1400 kg/m^3 was assumed.
For the BMT experiments κ between 0.052 and 0.133 were determined. The values for the α-pinene experiments were generally higher (0.146 - 0.224). This compares quite well to the study by *Juranyi et al.* (2009) where κ of 0.09 were observed for SOA formed from photo-oxidation products of α-pinene and the study by *Engelhardt et al.* (2008) where κ of 0.15 were observed for SOA formed from ozonolysis products of α-pinene and a monoterpene mix similar to BMT.

Table 4.1: *Fitting parameter p_0, κ, ρ_{ion}, and ϕ for the CCN-C measurements in SAPHIR. For the fitting with equation 2.29 the data was divided in three subranges (see text above for details).*

#	$p_0 \cdot 10^{-11}$			κ		
	Ia	Ib	II	Ia	Ib	II
1	1.601		1.124	0.053		0.107
2	1.255		1.140	0.086		0.104
3	1.302		1.063	0.080		0.120
4	1.073		1.055	0.118		0.122
5	1.024			0.129		
6	1.040		1.127	0.126		0.107
7	1.134		1.173	0.106		0.099
8	1.381		1.418	0.071		0.068
9	1.100			0.112		
11	1.133	1.286	1.011	0.106	0.082	0.133
20	0.902	0.868	0.861	0.167	0.180	0.183
21	0.918	0.778		0.161	0.224	
22	0.939	0.963		0.154	0.146	
#	ρ_{ion} [mol/m^3]			ϕ		
1	3065		6219	0.44		0.89
2	4992		6050	0.71		0.86
3	4636		6955	0.66		0.99
4	6829		7057	0.98		1.01
5	7497			1.07		
6	7276		6188	0.81		1.04
7	6116		5711	0.87		0.82
8	4118		3910	0.59		0.56
9	6491			0.93		
11	6121	4753	7689	0.87	0.68	1.10
20	9662	10421	10602	1.38	1.49	1.51
21	9332	12986		1.33	1.86	
22	8913	8482		1.27	1.21	

The lowest κ values were observed for the ozonolysis experiment (8) and the first day of experiment 1. But experiment 1 also showed the highest increase in κ towards the second day. In experiments 2, 3 and 4 the hygroscopicity increased towards the second day as well. For experiments 5, 6, 7 and 8 the particles

became less hygroscopic on the second day. But for # 4, 7, and 8 the variation was less than 7%. In experiment 11 where the BMT was added in three steps κ starts at an average value. After the second addition of BMT the hygroscopicity decreased, but after the third addition it increased again and reached the highest value observed during the BMT experiments.
The α-pinene experiments of type B in the dry chamber (# 22) exhibited lower κ than the ones in the humidified chamber (# 20 and 21). Furthermore, a decrease instead of an increase was observed when the chamber roof was opened.
For all three α-pinene experiments the starting κ was already higher than the final values of the BMT experiments. κ increased even more when the roof was opened in experiments 20 and 21. A decrease was observed for experiment 22 where CO was added an hour before the roof was opened. On the second day the roof stayed closed in experiment 20 and the hygroscopicity varied only slightly. In experiment 21 where the roof was opened κ increased to the maximum of 0.224 on the second day.

4.1.2 JPAC data

In JPAC the total particle concentration was much lower than in SAPHIR, and the size distribution changed quite fast, therefore only the polydisperse measurement method was used. But in each experiment two separate particle formation events occurred, and the polydisperse method was not suitable for the time interval when the second particle mode began to form and the first was still present. Hence, the data sets were divided into two subranges: The first range included the first 2 h when only the first mode was present and the second range started after 4 - 5 h when the second mode was dominating and lasted until the end of the experiments. The HTDMA measurements were conducted in the same intervals (see section 4.2.2). The fitting parameter, ρ_{ion} , κ, and ϕ are given in Table 4.2. In Table 4.3 these three parameters are averaged over all experiments conducted under the same conditions (i.e. temperature in the PC).
All measured κ values were between 0.037 and 0.113 and thus only slightly smaller than those measured in the BMT experiments in SAPHIR. Except for experiments 20_2, 30_2, 25_2, and 20_4 the hygroscopicity was lower for particles formed in the second mode. The relative decrease of κ lay between 5 and 35%, but the absolute difference between first and second mode was small (maximum 0.04). Grouping the different measurements using the leaf temperature of the plants in the PC, revealed that with increasing leaf temperature (and therefore with increasing VOC emissions) κ decreased. This effect was bigger than the difference between the two modes in each experiment. The experiment at 35°C was conducted with no lights in the PC. Hence, the emitted VOC concentration was comparable to the experiments at 15° C.

Table 4.2: *Fitting parameter p_0, κ, ρ_{ion}, and ϕ for the CCN-C measurements in JPAC. For the fitting with equation 2.29 the data was divided in two subranges (see text above for details), the first two digits of the experiment number are the temperature in the PC.*

#	$p_0 \cdot 10^{-11}$		κ		ρ_{ion} [mol/m^3]		ϕ	
	I	II	I	II	I	II	I	II
20_1	1.332	1.392	0.076	0.070	4428	4054	0.63	0.58
20_2	1.510	1.471	0.060	0.063	3446	3633	0.49	0.52
30_1	1.281	1.448	0.083	0.065	4792	3749	0.68	0.54
30_2	1.911	1.690	0.037	0.048	2151	2751	0.31	0.39
15_1	1.200	1.287	0.094	0.082	5459	4744	0.78	0.58
15_2	1.107	1.386	0.111	0.071	5459	4092	0.78	0.68
15_3	1.278	1.417	0.083	0.068	4814	3912	0.69	0.56
25_1	1.317	1.685	0.078	0.048	4534	2768	0.65	0.40
25_2	1.468	1.097	0.063	0.113	3648	6535	0.52	0.93
25_3	1.396	1.404	0.070	0.069	4035	3985	0.58	0.57
35D_1	1.206	1.220	0.093	0.091	5400	5278	0.77	0.75
15_4	1.184	1.272	0.097	0.084	5607	4859	0.80	0.69
15_5	1.194	1.270	0.095	0.084	5508	4870	0.79	0.70
15_6	1.207	1.317	0.093	0.078	5390	4531	0.77	0.65
15_7	1.241	1.350	0.088	0.074	5101	4312	0.73	0.62
20_3	1.270	1.417	0.084	0.068	4874	3914	0.70	0.56
20_4	1.289	1.118	0.082	0.109	4731	6286	0.68	0.90
35D_2	1.144	1.299	0.104	0.080	6006	4656	0.86	0.67

Table 4.3: *κ, ρ_{ion}, and ϕ for the CCN-C measurements in JPAC group by temperature in PC. For the fitting with equation 2.29 the data was divided in two subranges (see text above for details). The given errors are the standard deviation from averaging the different measurements.*

PC T	κ	
	I	II
15°C	0.094 ± 0.009	0.077 ± 0.007
20°C	0.075 ± 0.011	0.077 ± 0.021
25°C	0.070 ± 0.008	0.076 ± 0.033
30°C	0.060 ± 0.032	0.056 ± 0.012
35°C, dark	0.098 ± 0.007	0.086 ± 0.008
	ρ_{ion} [mol/m^3]	
15°C	5470 ± 496	4474 ± 380
20°C	4370 ± 643	4472 ± 1222
25°C	4072 ± 444	4429 ± 1922
30°C	4792 ± 1868	3749 ± 706
35°C, dark	5703 ± 428	4967 ± 440
	ϕ	
15°C	0.78 ± 0.07	0.64 ± 0.05
20°C	0.62 ± 0.09	0.64 ± 0.17
25°C	0.58 ± 0.06	0.63 ± 0.27
30°C	0.68 ± 0.27	0.54 ± 0.10
35°C, dark	0.81 ± 0.06	0.71 ± 0.06

4.2 HTDMA data

4.2.1 SAPHIR data

In this study the HTDMA was used to measure full humidograms, i.e. within 1 to 2.5 h the RH was varied between $< 10\%$ and 97.5% and the GF determined as $f(RH)$. In Table 4.4 all measurements for the experiments in SAPHIR are listed. In the first column the experiment numbers are given as defined in chapter 3.5.1, Table 3.1. The consecutive measurements during one experiment are numbered 1 to 3 for the first day and 4 to 5 for the second day. The starting time of each GF-measurement is referenced to the starting time of the experiment. The experiment start is defined as the time of the O_3 addition and immediate opening of the roof (or just the O_3 addition for the ozonolysis experiment, respectively). Typically, the particle production started in the minutes thereafter. Additionally, the selected dry sizes of the particles are listed for each measurement.
By comparing the slope of the growth curves between 40% and 97.5%, the BMT experiments (1 to 11) are grouped in six different classes (groups 1 to 6). The hygroscopicity of the particles increases from group 1 to 6. The group for each measurement is listed in the last column of Table 4.4. In case that classification in one group is insufficient,"1/3" indicates that the growth curve is presented best by group 1 for $a_w < 0.9$ and group 3 for $a_w > 0.9$.

Table 4.4: *HTDMA measurements conducted at SAPHIR. The experiment numbers refer to Table 3.1. Time: start time of measurement in h since experiment start, # : measurement number, size: selected dry particle size, group: see text above.*

exp No.	date	#	time [h]	size [nm]	group
1	2008-06-04	1	1:30	100	4
		2	4:30	120	4
	2008-06-05	4	21:30	120	4
		5	26:15	100	4
2	2008-06-06	1	1:45	100	4
		2	4:30	120	4
	2008-06-07	4	24:00	120	4
3	2008-06-09	1	2:45	120	4
		2	5:30	150	4
	2008-06-10	4	23:30	150	4
		5	26:45	180	3
4	2008-06-11	1	2:30	100	1
		2	5:15	150	2
	2008-06-12	4	22:30	150	3
		5	26:45	180	3
5	2008-06-13	1	2:15	120	1
		2	5:00	150	2
		3	8:30	180	2
6	2008-06-16	1	1:45	120	2
		2	5:30	150	2
	2008-06-17	4	25:30	150	3
		5	28:15	180	3
7	2008-06-18	1	3:45	120	2
		2	6:30	150	2
	2008-06-19	4	23:00	150	3
		5	26:30	180	3
8	2008-06-20	1	1:00	180	1
		2	4:45	180	1
9	2008-06-24	1	4:45	50	5
11	2008-06-26	1	1:15	50	5
		2	4:45	80	6
		3	8:15	80	6
	2008-06-27	4	24:00	80	6
20	2009-05-20	1	1:15	100	-
		2	4:45	100	-
	2009-05-21	4	26:15	120	1/3
21	2009-05-22	1	2:30	100	-
		2	7:30	120	1/3
	2009-05-23	4	24:00	150	1/3
		5	26:30	150	1/3
		6	28:15	170	1/3
23	2009-05-26	1	1:15	120	-
		2	3:15	150	-
		3	7:0	150	1

All measured growth curves are shown in Appendix A.2. To eliminate the size depended Kelvin-effect, a_w is used instead of RH. a_w is calculated from equation 2.6 for each data point (pair of RH and D_{wet}) assuming surface tension of water:

$$a_w = \frac{RH}{100} \cdot exp\left(-\frac{4M_w\sigma_w}{R\,T\rho_w\,D_{wet}}\right) \tag{4.2}$$

The average growth curve for each class is determined by fitting the data with the UNIFAC-fit described in detail in section 5.2. The measured data and these fits are displayed in Figures 4.1 to 4.6. The measurement errors are shown only for one data set to enhance clarity.

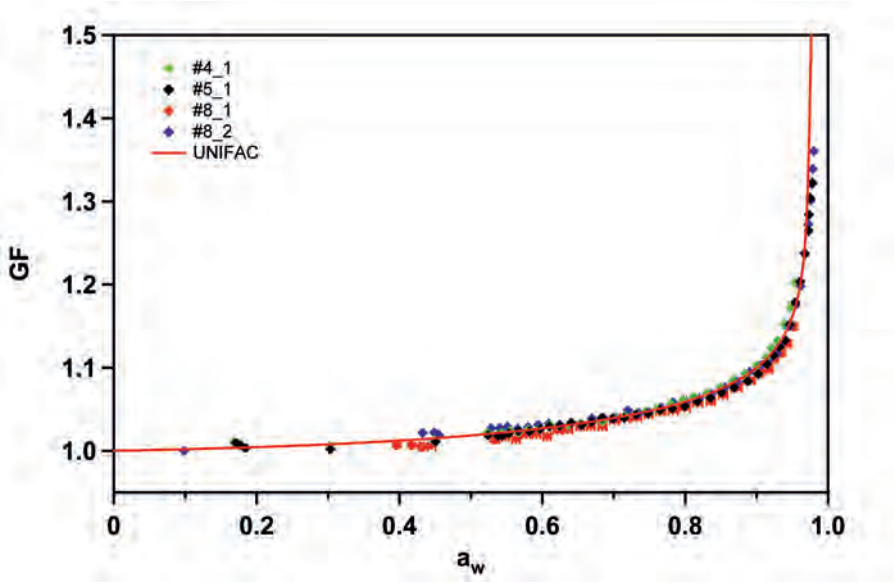

Figure 4.1: *Measured growth curves group 1: diamonds: measured data (for details on the experiment numbers see Tables 3.1 and 4.4), red line: fit to data using UNIFAC.*

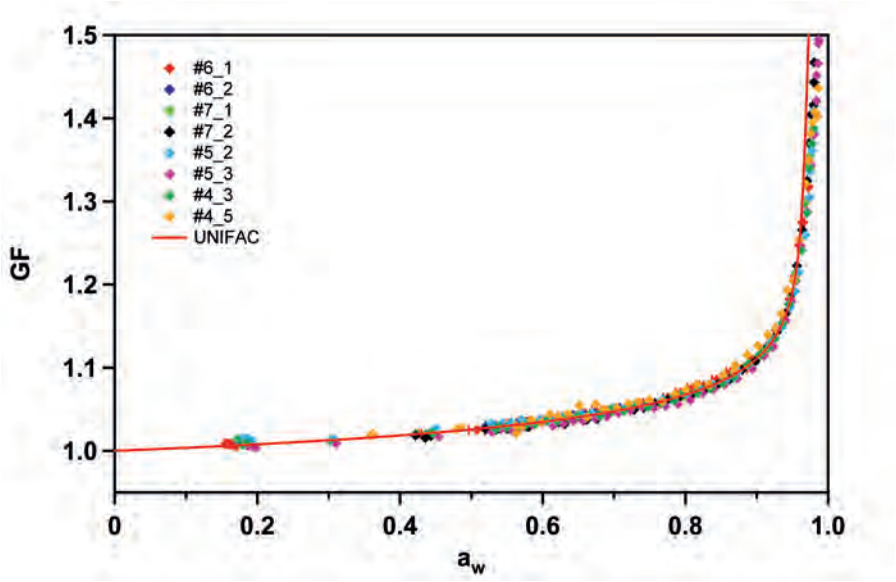

Figure 4.2: *Measured growth curves group 2: diamonds: measured data (for details on the experiment numbers see Tables 3.1 and 4.4), red line: fit to data using UNIFAC.*

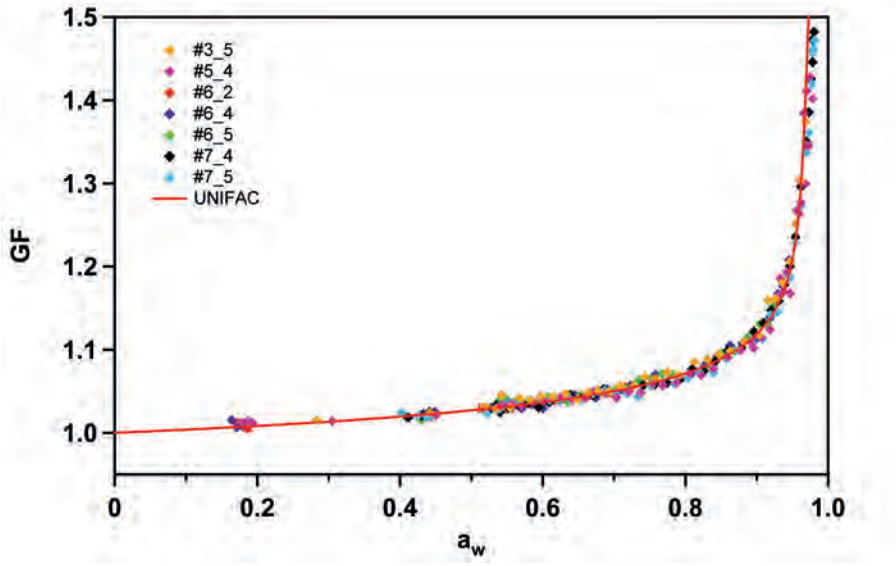

Figure 4.3: *Measured growth curves group 3: diamonds: measured data (for details on the experiment numbers see Tables 3.1 and 4.4), red line: fit to data using UNIFAC.*

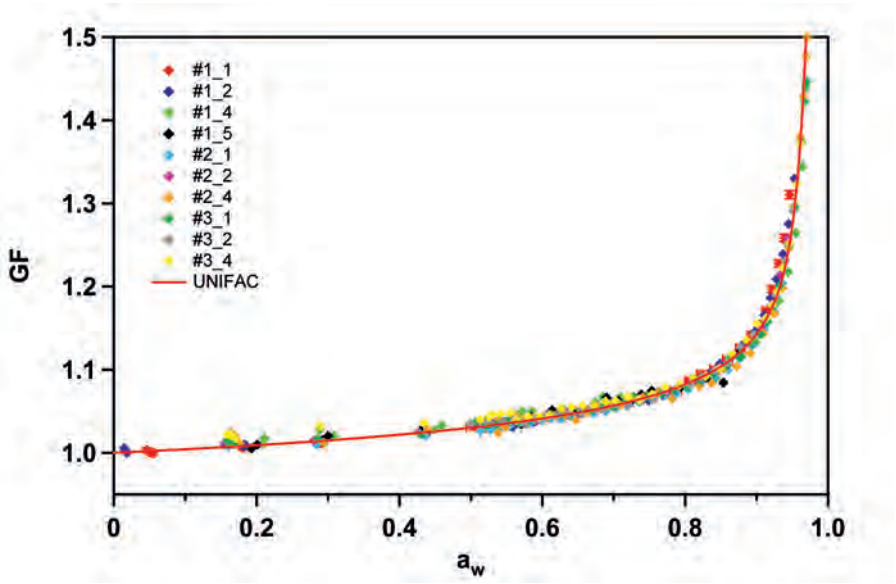

Figure 4.4: *Measured growth curves group 4: diamonds: measured data (for details on the experiment numbers see Tables 3.1 and 4.4), red line: fit to data using UNIFAC.*

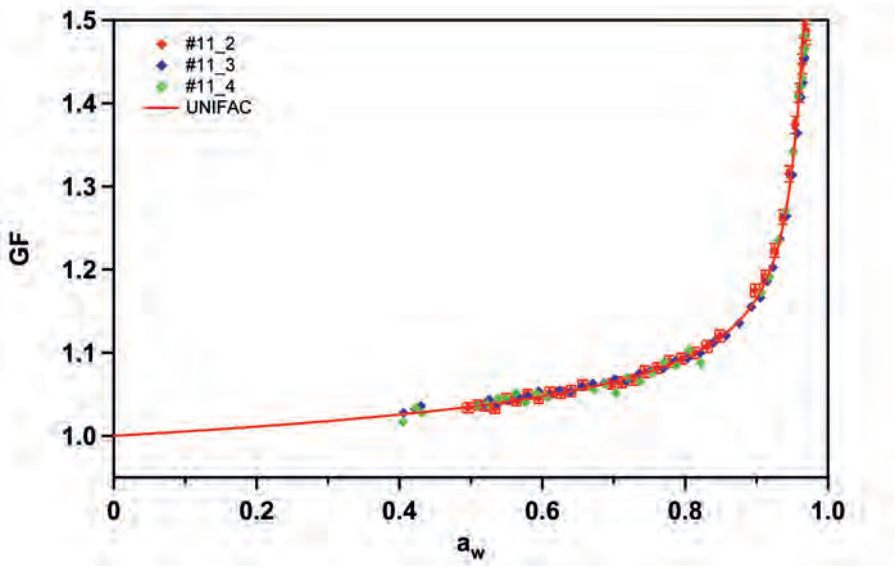

Figure 4.5: *Measured growth curves group 5: diamonds: measured data (for details on the experiment numbers see Tables 3.1 and 4.4), red line: fit to data using UNIFAC.*

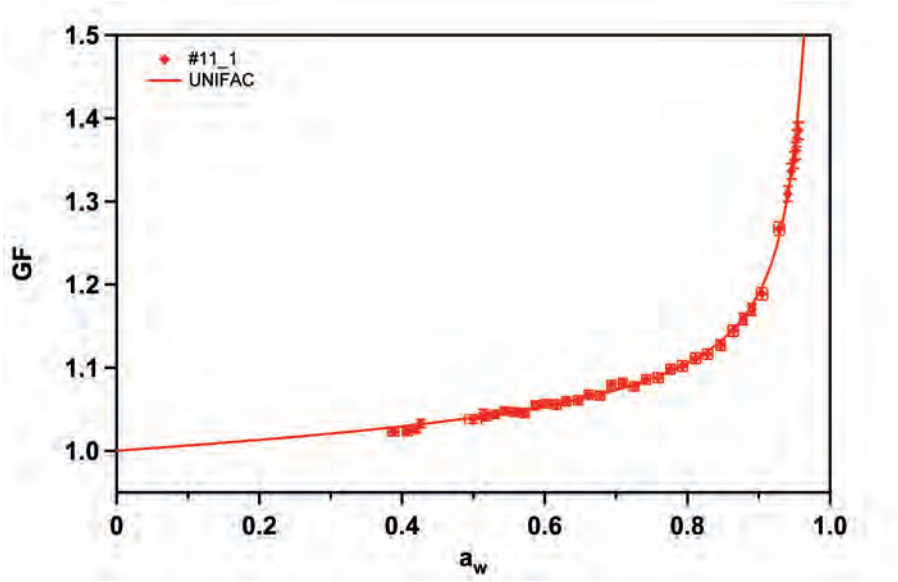

Figure 4.6: *Measured growth curves group 6: diamonds: measured data (for details on the experiment numbers see Tables 3.1 and 4.4), red line: fit to data using UNIFAC.*

Measurements during the first 4 h of the α-pinene experiments (20_1, 20_2, 21_1, 23_1, and 23_2) exhibit a different growth behavior than all others. First, the GF increases slightly with increasing a_w. But then it drops to a minimum between 0.45 and 0.48 a_w (see Figure 4.7). This feature is not captured by the UNIFAC-fit, thus, these measurements are not grouped together with the others.
An explanation for this behavior can be related to the different morphology of the particles. For all calculations it is assumed that the selected particles are compact spheres. However, if the particles contain voids, they may appear at a higher electro-mobility size than a solid sphere of the same mass. If a certain amount of water is taken up, the voids collapse. If the volume of the voids is larger than the water-uptake, the particles appear to shrink with increasing RH. As soon as the volume of the water taken up by the particles is larger than the volume of the voids, the particles appear to grow again. If this is the case, using the diameter measured under dry conditions to calculate GF will underestimate the GF and overestimate the amount of solute in the droplets. At the observed minimum of the growth curve the measured diameter is that of the compacted particle plus the absorbed amount of water. Therefore, it is still higher than the real D_{dry}, but close to it as the volume of the water taken up is small. As no independent information is available on how high the real GF should be at the observed minimum of the growth curve, the diameter at this minimum is used as D_{dry} to avoid GF less than 1, which would result in negative values for κ and ϕ. Such voids may be caused by the drying of the particles prior to the measurement. But they might also be an intrinsic problem as this feature was only observed for fresh particles and leveled off later in the experiment. As only α-pinene experiments of type B showed this feature, it may be either specific for α-pinene

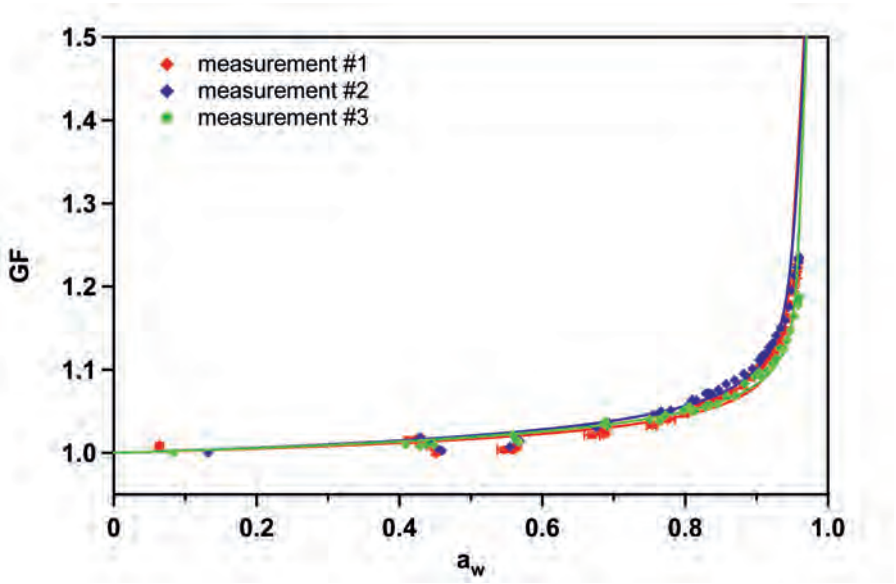

Figure 4.7: *Measured growth curves experiment 22: diamonds: measured data, red line: fit to data using UNIFAC.*

or related to the special reaction conditions in those experiments. All boundary conditions in the chamber such as temperature or humidity (both relative and absolute) occurred also during the BMT experiments where no such phenomenon in the growth curves was observed.

4.2.2 JPAC data

All measurements for the experiments in JPAC are listed in Table 4.5. In each JPAC experiment two separate particle formation events occurred. For measurements numbered 1 and 2 the particles were selected out of the first mode and for measurement # 3 from the second. In the same way as for the measurements at SAPHIR the growth curves were grouped (groups 1j to 6j, Figures 4.8 to 4.13). From group 1j to 6j the hygroscopicity increases. Comparing SAPHIR and JPAC data the groups 2 and 3j are almost identical, but the other groups exhibit a different curvature of the growth curves.

Table 4.5: *HTDMA measurements conducted at JPAC. The first two digits of the experiment number are the temperature in the PC. For further details see text above.*

exp No.	date	#	time [h]	size [nm]	group
20_1	2008-08-11	1	1:46	80	2j
		3	4:19	80	1j
20_2	2008-08-12	1	1:18	80	3j
		3	3:48	80	1j
30_1	2008-08-13	1	0:49	80	-
		3	3:34	80	1j
30_2	2008-08-14	1	0:48	80	-
		2	2:19	120	5j
		3	3:53	80	1j
15_1	2008-08-15	1	1:16	50	6j
25_1	2008-08-18	1	1:23	80	3j
		2	2:53	120	2j
		3	3:58	80	2j
25_2	2008-08-19	1	1:18	80	4j
		3	4:06	80	1j
25_3	2008-08-20	1	1:19	80	5j
		3	3:58	80	2j
35D_1	2008-08-21	1	1:30	80	6j
		3	4:56	80	3j
15_4	2008-08-22	1	1:48	80	-
		3	4:53	80	2j
15_5	2008-08-23	1	1:12	80	6j
		2	2:19	120	6j
		3	4:58	80	3j
15_6	2008-08-25	1	1:41	80	-
		3	4:01	80	3j
20_3	2008-08-26	1	1:55	80	4j
		3	4:58	80	2j
20_4	2008-08-27	1	1:32	80	5j
		3	4:02	80	2j
35D_2	2008-08-28	1	2:05	80	6j
		3	4:58	80	3j

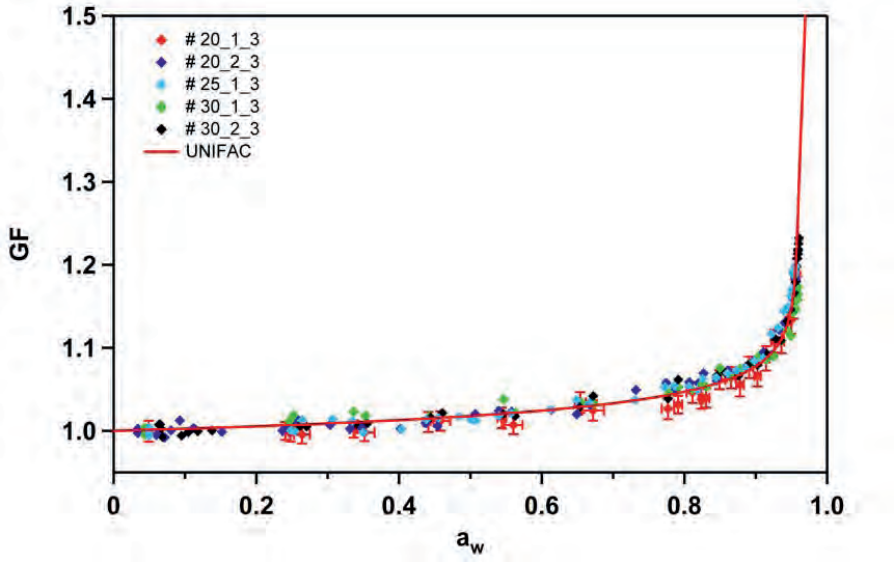

Figure 4.8: *Measured growth curves group 1j: diamonds: measured data (for details on the experiment numbers see Tables 3.2 and 4.5), red line: fit to data using UNIFAC*

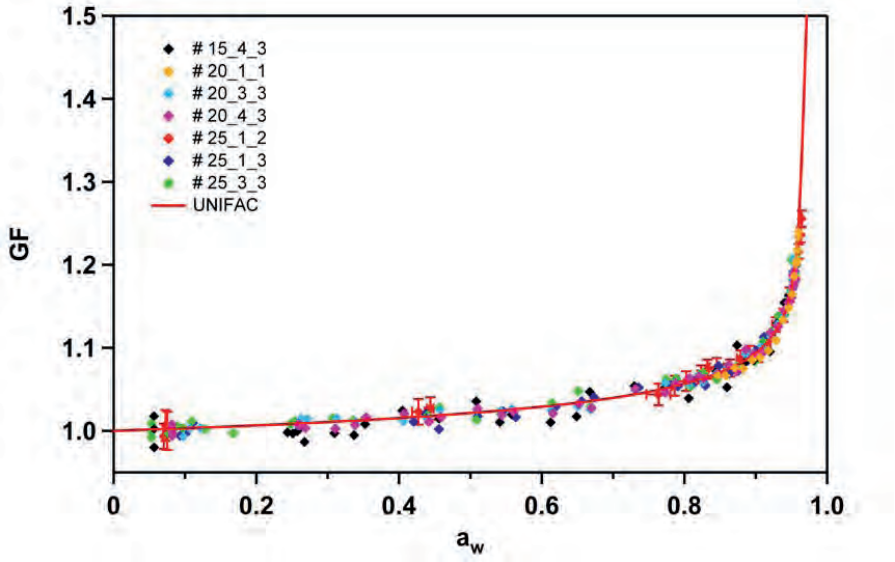

Figure 4.9: *Measured growth curves group 2j: diamonds: measured data (for details on the experiment numbers see Tables 3.2 and 4.5), red line: fit to data using UNIFAC*

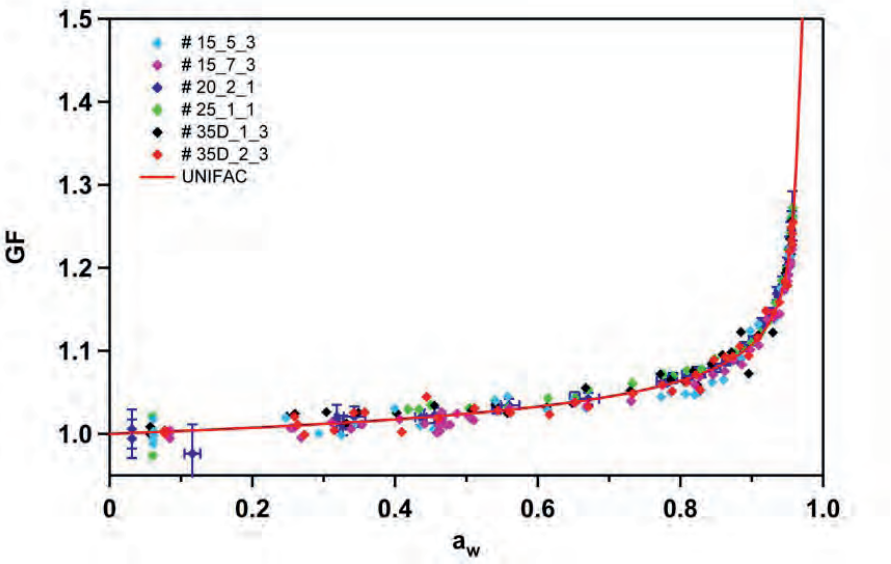

Figure 4.10: *Measured growth curves group 3j: diamonds: measured data (for details on the experiment numbers see Tables 3.2 and 4.5), red line: fit to data using UNIFAC*

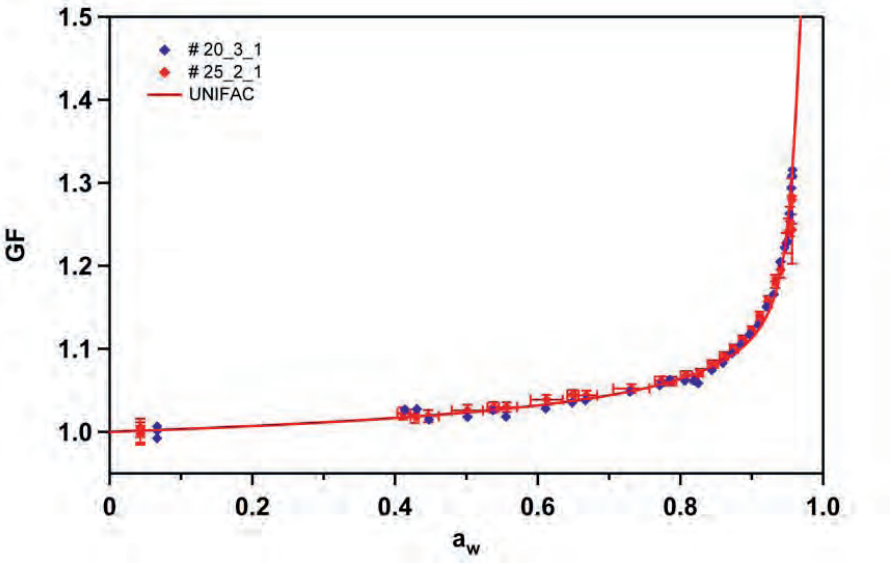

Figure 4.11: *Measured growth curves group 4j: diamonds: measured data (for details on the experiment numbers see Tables 3.2 and 4.5), red line: fit to data using UNIFAC*

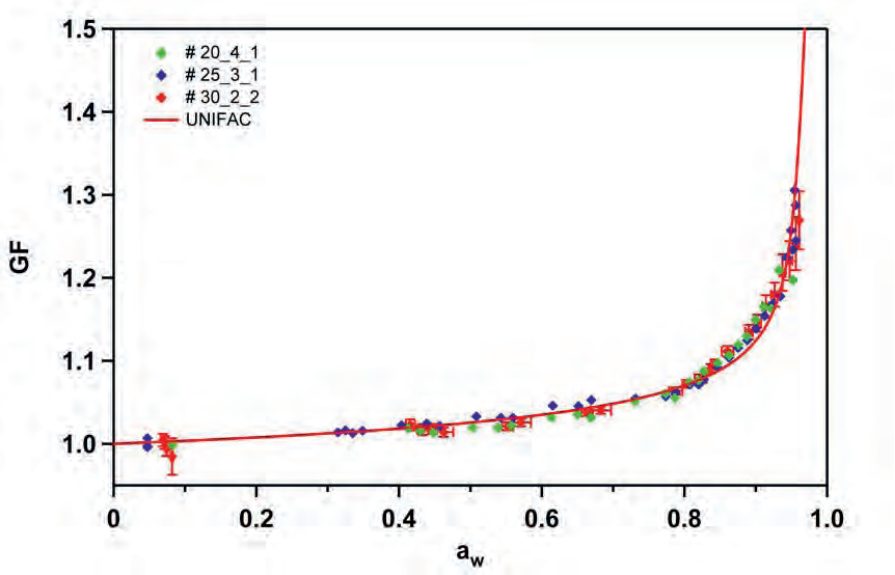

Figure 4.12: *Measured growth curves group 5j: diamonds: measured data (for details on the experiment numbers see Tables 3.2 and 4.5), red line: fit to data using UNIFAC*

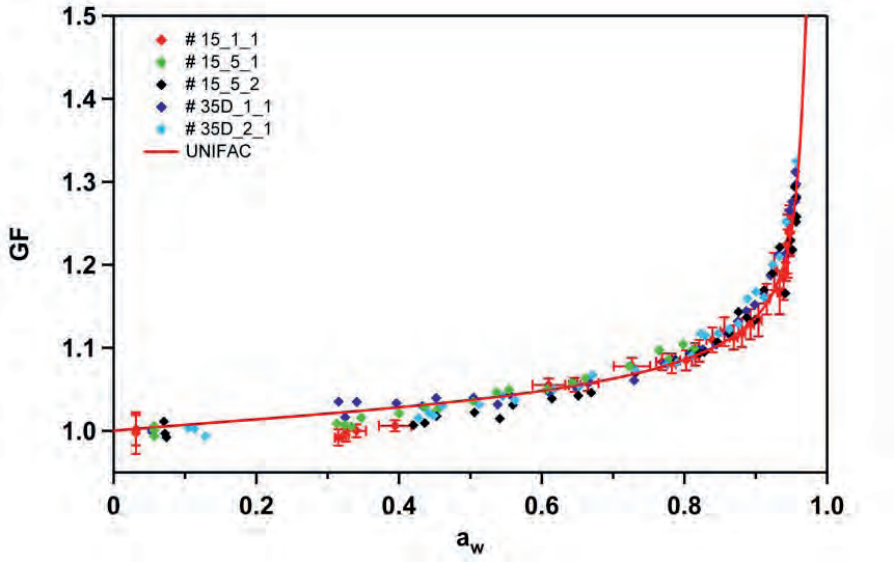

Figure 4.13: *Measured growth curves group 6j: diamonds: measured data (for details on the experiment numbers see Tables 3.2 and 4.5), red line: fit to data using UNIFAC*

Using equations 2.12 to 2.18, the parameters ϕ, ρ_{ion}, and κ were calculated from the measured data. The values at 90% *RH* are listed in Table A.1 and A.2 in the appendix. The average parameters calculated for the two sets of six groups are given in Table 4.6.

Table 4.6: *GF, κ, ρ_{ion}, and ϕ at 90% RH for the HTDMA measurements in SAPHIR using the grouping presented above. As error the standard deviation of the averaged measurements is given.*

group	GF	κ	ρ_{ion} [mol/m^3]	ϕ
1	1.092 ± 0.006	0.038 ± 0.002	1986 ± 91	0.28 ± 0.01
2	1.107 ± 0.005	0.044 ± 0.003	2315 ± 158	0.33 ± 0.02
3	1.112 ± 0.006	0.046 ± 0.003	2411 ± 173	0.34 ± 0.03
4	1.125 ± 0.006	0.055 ± 0.003	2864 ± 152	0.41 ± 0.02
5	1.142 ± 0.006	0.069 ± 0.004	3592 ± 191	0.51 ± 0.03
6	1.149 ± 0.006	0.078 ± 0.001	4046 ± 14	0.58 ± 0.002
1j	1.040 ± 0.006	0.018 ± 0.003	922 ± 143	0.13 ± 0.02
2j	1.060 ± 0.011	0.026 ± 0.005	1374 ± 262	0.20 ± 0.04
3j	1.067 ± 0.011	0.030 ± 0.005	1569 ± 255	0.22 ± 0.04
4j	1.072 ± 0.003	0.032 ± 0.001	1678 ± 42	0.24 ± 0.01
5j	1.097 ± 0.011	0.044 ± 0.004	2303 ± 195	0.33 ± 0.03
6j	1.106 ± 0.021	0.051 ± 0.010	2650 ± 538	0.38 ± 0.08

Some trends could be observed in the CCN-C measurements which also occurred in the HTDMA measurements. The ozonolysis experiment (9) showed the lowest and experiment 11 the highest hygroscopic growth of all measurements. The decrease in experiment 3 and the change during experiment 11 due to the stepwise addition of the BMT were also visible. In the JPAC experiments both, CCN-C and HTDMA measurements, showed higher κ values for particles selected out of the first particle mode than from the second. But there were certain differences. The α-pinene experiments exhibit a average κ, and during experiment 1 and 2 only a slight increase in κ was observed.

4.2.3 Measurement errors

κ given in Table 4.6, A.1, and A.2 was calculated applying equation 2.18 and solving it for κ:

$$\kappa = \frac{D_p^3 - D_{dry}^3}{D_{dry}^3} \left(\frac{exp\left(\frac{A}{D_p}\right)}{RH} - 1 \right) \tag{4.3}$$

$$\text{with } A = \frac{4 M_w \sigma_w}{R T \rho_w}$$

This equation can be simplified using GF instead of the particle size:

$$\kappa = (GF^3 - 1) \left(\frac{exp\left(\frac{A}{D_p}\right)}{RH} - 1 \right) \tag{4.4}$$

The error of κ can be derived from this equation with Gaussian error propagation.

$$\sigma(\kappa) = \pm \frac{\sqrt{\left(\sigma(GF)\cdot 3\,GF^2\left(\frac{100\cdot exp(A/D_p)}{RH}-1\right)\right)^2 + \left(\sigma(RH)\cdot(GF^3-1)\cdot\frac{100\cdot exp(A/D_p)}{RH^2}\right)^2 + \left(\sigma(D_p)\cdot(GF^3-1)\cdot\frac{100\,A\cdot exp(A/D_p)}{RH\,D_p^2}\right)^2} \quad (4.5)$$

The calculation of the statistical errors of GF, RH and D_p is described in section 3.2.3. Using these statistical errors leads to rather small $\sigma(\kappa)$ (relative $\sigma(\kappa) \sim 5\%$ in each measurement).
To estimate the accuracy κ, the systematic errors of the measured quantities are used in equation 4.5. Applying $\sigma(GF)_{sys} = 0.01$, $\sigma(RH)_{sys} = 1.5\%$, and $\sigma(D_p)_{sys} = 1\% \cdot D_p$ leads to average $\sigma(\kappa)_{sys}$ of $\sim 20\%$ (see Tables A.1 and A.2). Note that this is the upper limit of measurement uncertainty. For example: calibration measurements with $(NH_4)_2SO_4$ aerosol were conducted frequently to measure the systematic offset of the RH sensors. The observed variations between these measurements was within the reported statistical error. The derived correction factors for the RH measurement were constant for up to 6 weeks (see section 3.2.2 for details on calibration). The HTDMA was run under the same conditions during the SOA measurements and the calibration. Consequetly, $\sigma(RH)_{sys}$ would be reduced to the uncertainty of the calibration procedure, which is equal to the much smaller statistical error.
The errors of ρ_{ion} and ϕ are calculated in a similar way starting from equation 2.12 and 2.14. As κ, ρ_{ion} , and ϕ are directly related by equations 2.13 and 2.24, the relative errors are the same for all three parameters.

5. Discussion

In this chapter the results from the BMT experiments in the SAPHIR chamber will be discussed with respect to the closure between hygroscopic growth and CCN-activity measurements. Thereafter the relation of hygroscopicity and the formation conditions of the SOA will be investigated. Then chemical aging of the particles will be discussed. Last the findings for the SAPHIR chamber experiments will be transfered to the data from JPAC experiments.

5.1 Closure between the sub- and super-saturated regime

In this section the discrepancies between HTDMA and CCN-C measurements - if a constant κ is used for each measurement - will be described. Two possible explanations using one additional single parameter are proposed.

5.1.1 Comparing CCN-C and HTDMA data

Apart from the minor different trends in the HTDMA and CCN-C measurements, the main difference is that all κ values calculated from HTDMA measurements at 90% RH ($\kappa(90\%)$) are up to a factor of 3 lower than those from CCN-C measurements. This discrepancy is much larger than the calculated statistical error of κ (CCN-C: 2 - 6%, HTDMA: 5%). For most experiments it is also larger than the accuracy estimated from the systematic measurement errors ($\sigma(\kappa)_{sys} \leq$ 20%). When using the $\kappa(90\%)$ values to extrapolate the Koehler curve (equation 2.18) to the super-saturated regime, much higher SS_{crit} are predicted for a given size than measured with the CCN-C. These calculations were performed for all data sets and the results are shown in the SS_{crit} vs. $D50$ plots in appendix A.1 (black triangles). Below in Figure 5.1 a representative example is shown.
The values predicted from hygroscopic growth can be fitted with the same method as the measured $SS_{crit}/D50$ (equation 2.29). As the variation in $\kappa(90\%)$ during one experiment is minimal compared to κ(CCN), all HTDMA measurements of one experiment are fitted together. The fitting parameter p_0 is listed in Table 5.1. The $SS_{crit}(90\%)$ calculated from this fit are plotted versus the fits of the measured SS_{crit}(CCN) in Figures 5.2 and 5.3. The ozonolysis experiment exhibits the largest overprediction of SS_{crit} (by a factor of 2). On the second day SS_{crit} is only overestimated by 33 - 66%. This is not in agreement with findings of *Rissler et al.* (submitted). They found an overprediction of SS_{crit} of maximal 34% for comparable aerosols.

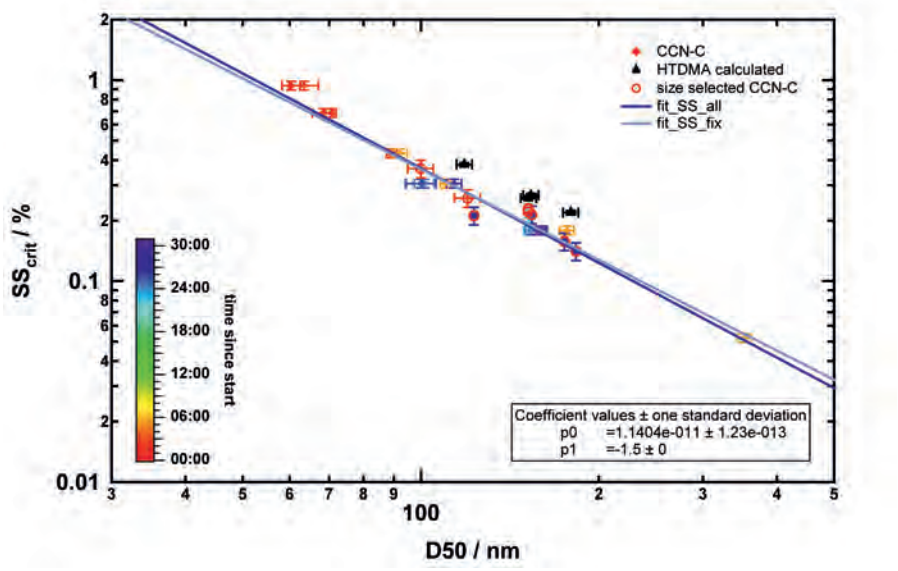

Figure 5.1: *SS_{crit} and D50 measured with CCN-C and calculated from HTDMA data for experiment 3 using a constant κ.*

Table 5.1: *Fitting parameter p_0 for SS_{crit}/D50 predicted from HTDMA data.*

experiment	$p_0 \cdot 10^{-11}$
1	1.53 ± 0.01
2	1.57 ± 0.01
3	1.58 ± 0.02
4	1.76 ± 0.01
5	1.800 ± 0.009
6	1.86 ± 0.01
7	1.72 ± 0.01
8	1.86 ± 0.02
11	1.337 ± 0.009

There are two approaches to explain these discrepancies which both introduce another single parameter into the Koehler equation: A) The parameter κ is underestimated when calculated from HTDMA data. This is equivalent to overestimating the amount of solute entities in the solution e.g. caused by limited solubility. B) The parameter κ is overestimated when calculated from CCN-C data as the surface tension of pure water was used, which was too high. The surface tension of the solution droplet could be reduced by surface active organic compounds which have been found in atmospheric aerosol by e.g. *Facchini et al.* (2000) and *Dinar et al.* (2006) .

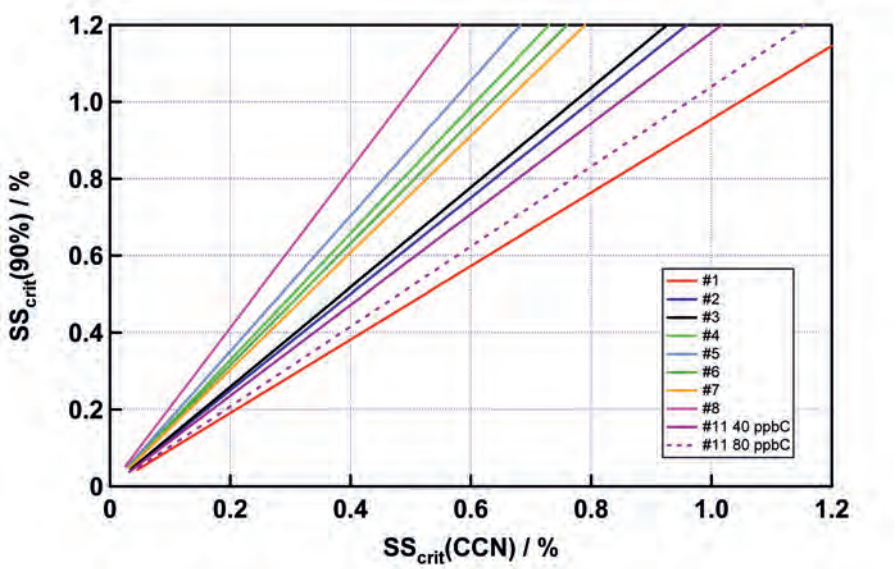

Figure 5.2: *SS_{crit} predicted from hygroscopic growth measurements at 90% RH vs. SS_{crit} measured with the CCN-C in the first 6h of the experiments.*

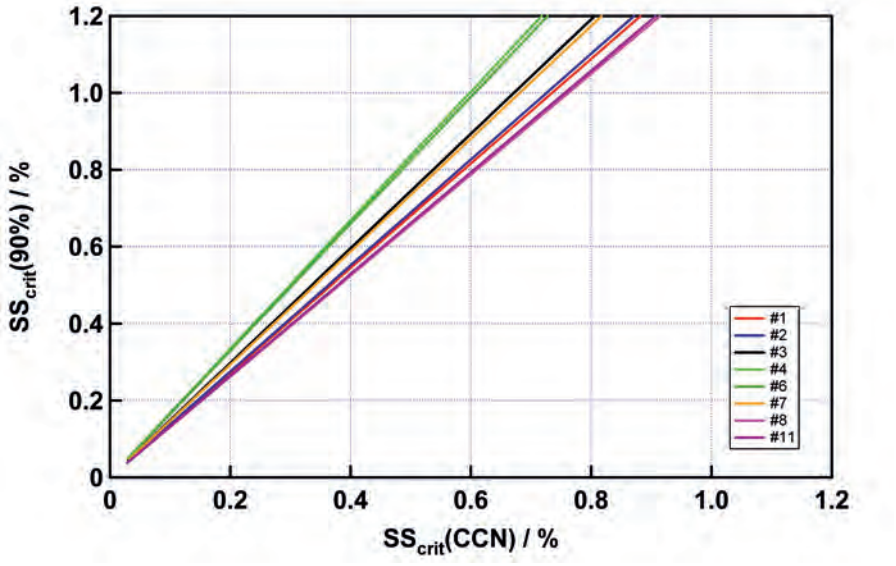

Figure 5.3: *SS_{crit} predicted from hygroscopic growth measurements at 90% RH vs. SS_{crit} measured with the CCN-C on the second day of the experiments.*

5.1.2 Solute entities in solution

When calculating $\kappa(90\%)$ from HTDMA data with equation 2.18 the volume of water and the dry solute are derived from the measured particle diameters. If the dry particle dissolves only partially, V_w is still described by equation 2.17 using the measured dry diameter as D_{dry}. But the volume of the solute is only the fraction f_s of the dry particle that dissolved. With this equation 2.18 changes to:

$$S = \left(1 + \kappa \frac{f_s \cdot D_{dry}^3}{\left(D_p^3 - D_{dry}^3\right)}\right)^{-1} \cdot exp\left(\frac{4 M_w \sigma_w}{R\,T \rho_w D_p}\right) \tag{5.1}$$

Thus, the dissolved volume fraction of the dry particle equals:

$$f_s = \frac{\kappa(90\%)}{\kappa(\mathrm{CCN})} \tag{5.2}$$

$\kappa(90\%)$: κ derived from growth curves at 90% RH
$\kappa(\mathrm{CCN})$: κ derived from fitting equation 2.29 to $SS_{crit}/D50$ data

The calculated dissolved volume fractions are 0.27 to 0.83 for BMT, 0.16 to 0.30 for α-pinene, and 0.18 to 0.70 for JPAC experiments. The average values for the six groups for BMT and α-pinene experiments are listed in Table 5.2. In the JPAC experiments the values for the second particle mode are 10 to 65% lower than for the first mode. For the SAPHIR experiments no clear trend comparing first and second day measurements could be observed. Using the grouped HTDMA data, the first three groups exhibit a 35 - 45% lower dissolved fraction than the last three. But the spread within the groups is to some extend bigger than this difference. This might indicate that the dissolved volume fraction is not directly correlated to the absolute value of κ.

5.1.3 Surface tension of the solution

In the previous calculation of κ the surface tension of pure water was assumed for the droplet. In the sub-saturated regime the influence of the Kelvin term (surface tension dependent term in Koehler equation) is minimal. Therefore, changing the surface tension does not change the κ values calculated from HTDMA measurements. But in the super-saturated regime decreasing σ_w by a factor of f_σ, reduces κ by a factor of $(f_\sigma)^3$ (equations 2.30 and 2.24).

$$f_\sigma = \left(\frac{\kappa(90\%)}{\kappa(\mathrm{CCN})}\right)^{\frac{1}{3}} \tag{5.3}$$

Using κ from the HTDMA measurements, the surface tension reduction can be calculated for all CCN-C measurements. The values derived for the grouped hygroscopic growth data are shown in Table 5.2. Instead of 0.073 N/m (pure water) values between 0.041 and 0.065 N/m for BMT, between 0.039 and 0.048 N/m for α-pinene, and between 0.041 and 0.065 N/m for JPAC experiments were observed. In the JPAC experiments the calculated σ was 10 to 25 % lower for the

second particle mode than for the first mode. Generally, the same trends are observed as described above for the limited solubility approach.
Measurements extending over the same range can be found in literature. *Ziese et al.* (2008) found surface tensions of 0.052 to 0.069 N/m for aerosols containing humic acid like substances. For aerosol produced by photo oxidation of α-pinene surface tensions of 0.0553 and 0.0578 N/m depending on the precursor concentration were observed (*Juranyi et al.* (2009)). For ozonolysis of α-pinene aerosol *Wex et al.* (2009) calculated surface tensions of ∼30 N/m if hygroscopic growth data measured below 98% *RH* was used. If the calculations were based on data with $RH > 98\%$, the surface tension was reduced only to 0.052 to 0.065 N/m.

5.1.4 Deducing M_s from κ

The two parameterizations f_s and f_σ describe two completely different physical phenomena. But with the approach presented above they cannot be separated. It could also be a combination of both effects leading to a κ in between $\kappa(90\%)$ and κ(CCN). To evaluate the two approaches, equation 2.21 is used to calculate the average molecular mass of the solute. The effective particle density measured with the HR-Tof-AMS is used for ρ_s. In Table 5.2 the calculated values are listed for the grouped HTDMA data. The CCN-C data was grouped accordingly using the same time intervals as the HTDMA measurements. $M_s(\sigma)$ is the molecular weight of the solute calculated with reduced surface tension and $\kappa(90\%)$, and M_s(sol) is calculated with limited solubility at 90% *RH* and κ(CCN).

Table 5.2: *Calculated reduced surface tension of the droplet, dissolved fraction, and molecular weights for the different approaches. The given errors are the standard deviation from averaging in the groups.*

group	σ_s	f_s	$M_s(\sigma)$ [g/mol]	M_s(sol) [g/mol]
1	0.053 ± 0.006	0.42 ± 0.14	721 ± 28	305 ± 102
2	0.052 ± 0.002	0.39 ± 0.05	616 ± 16	238 ± 27
3	0.054 ± 0.003	0.42 ± 0.05	648 ± 40	271 ± 34
4	0.063 ± 0.007	0.68 ± 0.24	507 ± 62	333 ± 94
5	0.064 ± 0.001	0.72 ± 0.03	343 ± 6	246 ± 8
6	0.063 ± 0.006	0.69 ± 0.19	367 ± 40	264 ± 86

The values calculated with reduced surface tension are between 343 and 721 g/mol. As the molecular weight of the gas-phase precursors was 140 g/mol and only oxygen is added due to oxidation, these high M_s could only be reached by oligomers of the primary oxidation products. Evidence for oligomerization in aerosol particles during smog chamber experiments has been observed (e.g. *Mueller et al.* (2009), *Kalberer et al.* (2004)). But here the particles would have to consist almost completely of those oligomers. Assuming that only the fraction f_s of the dry particle is dissolved, this leads to much lower M_s between 246 and 324 g/mol. This is the upper end of the range of M_s determined with the APCI-MS.
From this deliberation the approach with limited solubility seems more likely to be true. While both approaches are able to achieve closure between hygroscopic

growth and CCN activation measurements, they cannot be used to predict the CCN activation from GF data. In both cases the additional parameter (the solved fraction or reduced surface tension) can only be derived if data from sub- and super-saturated regime is already available.

5.2 UNIFAC model calculations

Although the discrepancies in the hygroscopicity parameters derived for sub- and super-saturated regime can be explained with an additional parameter (solubility or surface tension reduction), there is already a strong indication that there is a dependency on the RH (i.e. the concentration in the droplet). In this section the need for a concentration (RH) dependent parametrization of the Koehler theory will be described. The use of the UNIFAC model to fit the measured data will be explained and tested with surrogates for the most likely compounds in the particles.

5.2.1 a_w dependence of κ and ϕ

With equation 2.18 κ is calculated for each data point on the growth curve (see Figure 5.4 and appendix A.3). This reveals that the hygroscopicity decreases with increasing a_w. Between a_w 0.9 and 0.95 the curves reach a minimum before it increases again. The position of this minimum (both a_w and κ values) is characteristic for the different growth curves groups. This upward trend for very high a_w can explain the overprediction of SS_{crit} when using HTDMA data. Since the observed increase after the minimum is less than the maximum systematic error (black error bars in Figure 5.4), it might be a measurement artifact.

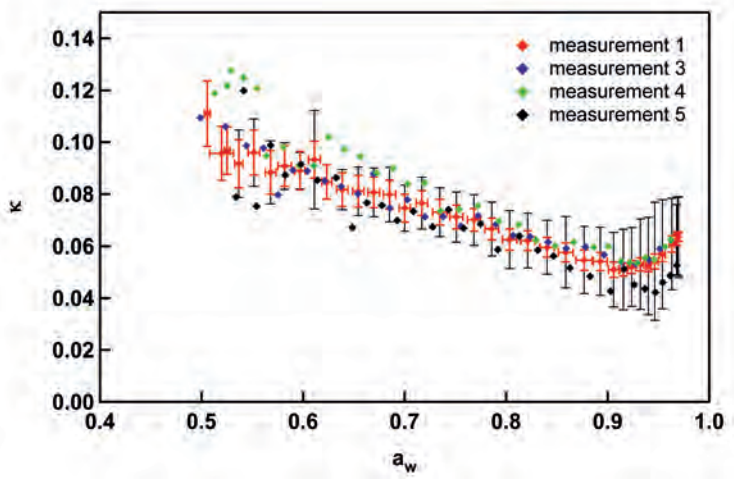

Figure 5.4: *κ calculated for the complete growth curve measured in experiment 3. Error bars in red represent the statistical error, and black error bars are the accuracy (details in section 4.2.3). The shown error bars are representative for all measurements.*

Although κ is a powerful tool for comparing sub- and super-saturated data, it has the disadvantage that the limit for $a_w \rightarrow 1$ does not approach the same value for all possible compounds (see equation 2.21). In addition no physical-chemical model exists for the exact course of κ as $a_w \rightarrow 1$ for a wide range of organic compounds. Thus, it can not be generally answered if the observed minimum is real.
If ϕ is used instead, the characteristics of the ϕ vs. a_w curve can be approximated with the UNIFAC model (see section 2.3) and for dilute solutions ($a_w \rightarrow 1$) $\phi \rightarrow 1$. To calculate ϕ from the hygroscopic growth data or rather from ρ_{ion} , values for M_s ρ_s, and ν must be known (or assumed). The effective density of the particles can be calculated from the electro-mobility diameter measured in the SMPS and the aerodynamic diameter measured in the HR-Tof-AMS (see equation 3.25). For the BMT experiments effective densities between 1440 and 1730 kg/m^3 were determined. The average M_s was deduced from measurements with a APCI-MS (*Reinnig* (2009)). As a starting value 210 g/mol was used. Further it is assumed that the organic compounds do not dissociate and are completely dissolved in the available amount of water (i.e. no deliquescence/efflorescence). Therefore, $\nu = 1$. With these values ϕ is calculated for each measured data point on the growth curves (see Figure 5.5 and appendix A.3). The trend is the same as for the $\kappa(a_w)$.

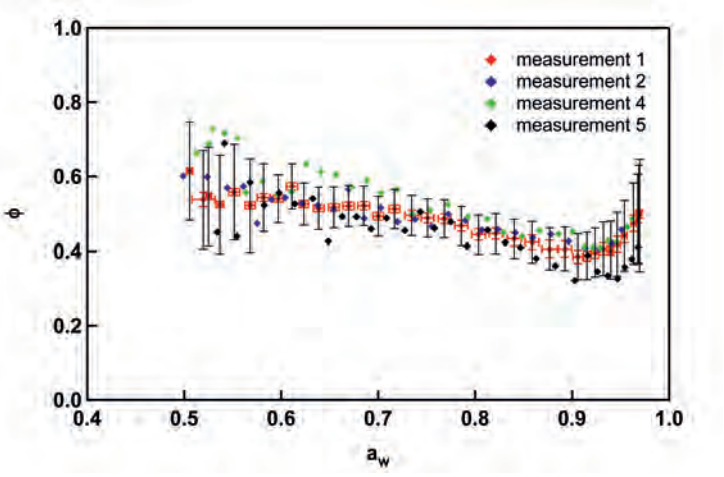

Figure 5.5: *ϕ calculated for the complete growth curve measured in experiment 3. $M_s = 210$ g/mol and $\rho_s = 1460$ kg/m^3 are used. Error bars in red represent the statistical error, and black error bars are an estimate for the accuracy (details in section 4.2.3). The shown error bars are representative for all measurements.*

5.2.2 UNIFAC calculations with surrogates for SOA compounds

The UNIFAC model calculates the corresponding a_w for a given molar fraction of water. Applying equation 2.8, this can be converted into ϕ. The UNIFAC model can be used both to calculate binary (single organic compound + water) and

complex multi-component mixtures. The organic compounds are represented as the sum of their functional groups. The functional groups and parameters used in this study are listed in Tables 2.1 and 2.2.
SOA particles can consist of a large number of different compounds and the exact composition cannot be determined. *Larsen et al.* (2001) identified a range of different particle phase products of the photo oxidation of single MTs. The most abundant were C_{10}-keto-aldehydes, C_{10}-keto-carboxylic acids, C_{10}-hydroxy-keto-carboxylic acids, and C_{10}-hydroxy-keto-aldehydes for MTs with a endocyclic double bond (e.g. α-pinene) and C_9-ketones, C_9-dicarboxylic acids, and C_{10}-hydroxy-keto-carboxylic acids for MTs with an exocyclic double bond (e.g. β-pinene). The common feature of these compounds is a hydrocarbon backbone of 9 or 10 carbon atoms carrying two or three oxidized groups. The molecular weights are between 150 and 200 g/mol, and the O/C ratio is between 0.2 and 0.5.

Homologue series of dicarboxylic acids

Before the measured data was fitted with the UNIFAC model, the prediction of $\phi = f(a_w)$ of the model was tested with a set of surrogates. The series of dicarboxylic acids from oxalic to sebacic acid was chosen as they have the same degree of functionality (two oxidized groups) and similar M_s and O/C values. For this investigation the solubility was ignored, i.e. the metastable efflorescence branch was calculated. The $\phi(a_w)$ curves calculated for binary mixtures of one acid and water are shown in Figure 5.6.

Table 5.3: *Dicarboxylic acids used in UNIFAC calculations.*

acid	CH_2	M_s [g/mol]	O/C
oxalic	0	90	2.00
malonic	1	104	1.33
succinic	2	118	1.00
glutaric	3	132	0.80
adipic	4	146	0.67
pimelic	5	160	0.57
suberic	6	174	0.50
sebacic	8	202	0.40

As the chain length of the acids increases, ϕ at a given a_w decreases. This was to be expected as the CH_2 groups are hydrophobic compared to oxidized groups. By increasing the hydrophobic fraction in the organic molecules, the interactions with the surrounding water become less ideal. Thus, ϕ, the parameter for the ideality of the solution, diverges more strongly from one.
Except for oxalic and malonic acid all curves show a minimum between a_w 0.9 an 0.99. With increasing chain length the position of the minimum moves towards higher a_w and lower ϕ. Also the minimum becomes more distinct and almost turns into a step function. The slope of the curve leading towards the minimum increases as well. Note that this behavior is similar to that of the measured data.

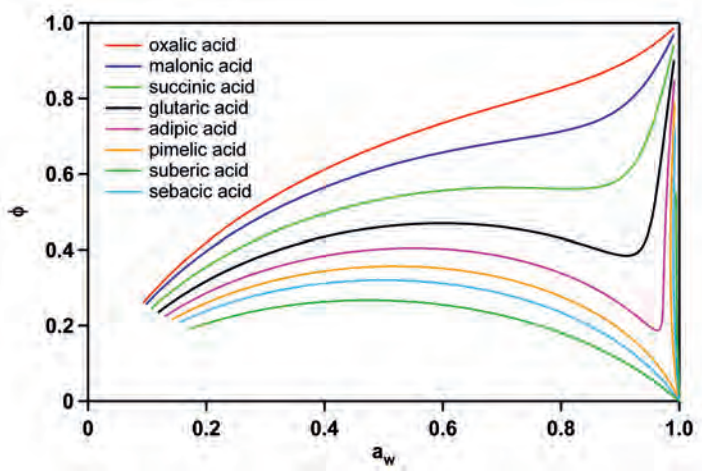

Figure 5.6: *$\phi(a_w)$ curves calculated for binary dicarboxylic acid/water mixtures with UNIFAC.*

Dependence of ϕ on O/C ratio

The O/C ratio is a commonly used indicator for the oxidation degree of compounds in aerosol particles as it can be derived from AMS data. Generally, the O/C ratio of the identified compounds increases with aging, i.e. higher oxidized compounds are more abundant in the particles. The O/C ratio is also used as a proxy for the hygroscopicity. With increasing O/C ratio (i.e. increasing degree of oxidation) the hygroscopicity increases. As shown in Figure 5.6, this is the case for a series of compounds where only the occurrence of one functional group varies (here CH_2). Thus, the change in the O/C ratio is only due to the change in the ratio of the two different groups.
To further investigate the interrelation of ϕ on the O/C ratio, the $\phi(a_w)$ curves for a series of "derivatives" of suberic acid were calculated. To the suberic acid backbone the four oxidized groups used in this UNIFAC version were added creating C_{10} compounds with three oxidized groups. As the keto group can only be added to the model with an additional methyl group, there is a methyl group added in all cases. UNIFAC is not sensitive to the exact position of a group in a molecule therefore no additional structure information is needed. The used compounds are listed in Table 5.4 and the calculated curves are shown in Figure 5.7.
Introducing another oxidized group always led to larger ϕ for the same a_w , i.e. it increases the $\phi(a_w)$ curve, even though the O/C ratio stays constant for the methyl aldehyde and the methyl ketone and even decreases for the hydroxy ethyl compound. The effect of the groups on $\phi(a_w)$ increases in the following order: $CH_3CO < OH < COOH \ll CHO$. Adding the aldehyde group has by far the largest effect on $\phi(a_w)$.
From the results for these simple systems it can be concluded that the O/C ratio can be used as an indicator for the hygroscopicity of aerosol particles only under certain conditions. In a system where the chemical aging (oxidation) only

adds more oxidized groups to the basic molecules an increase in the O/C ratio is most likely correlated to an increase in the hygroscopicity. But if aerosol particles from different gas-phase precursors and different oxidation regimes (e.g. ozonolysis vs. photo chemistry) are compared, the connection between O/C ratio and hygroscopicity might not be straightforward.

Table 5.4: *Suberic acid derivatives calculated with UNIFAC. M_s is given in g/mol.*

organic component	CH_2	CH	COOH	CHO	CH_3CO	OH	M_s	O/C
suberic acid	6	0	2	0	0	0	174	0.50
+ aldehyde	5	1	2	1	0	0	202	0.56
+ methyl aldehyde	6	1	2	1	0	0	216	0.50
+ methyl ketone	5	1	2	0	1	0	216	0.50
+ hydroxy ethyl	7	1	2	0	0	1	201	0.40
+ methyl carboxylic	6	1	3	0	0	0	232	0.60

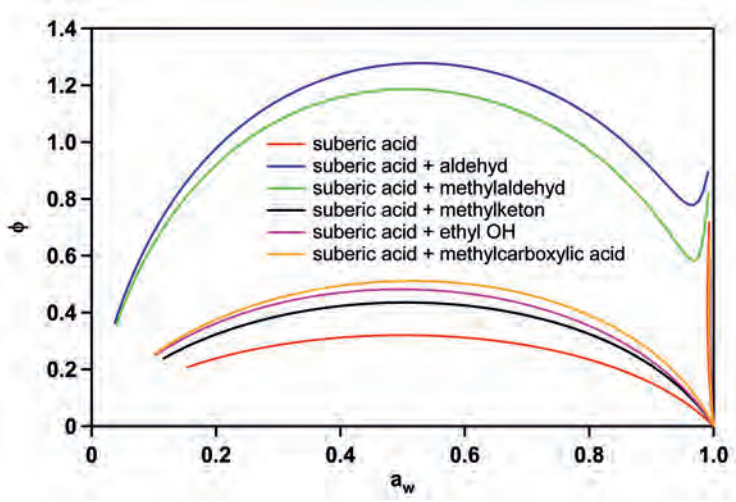

Figure 5.7: *$\phi(a_w)$ curves calculated for binary "suberic acid derivatives"/water mixtures with UNIFAC.*

5.2.3 Fitting the measurement data

The UNIFAC model calculates a_w for a given x_w in dependency on the organic molecule(s) defined in the system. Therefore, the measured RH is converted to a_w applying equation 4.2 and the measured GF is converted to x_w:

$$x_w = \left(1 + \frac{n_s}{n_w}\right)^{-1} \tag{5.4}$$

n_s and n_w can be expressed by equations 2.10, 2.11, and GF can be used instead of the particle diameters.

$$x_w = \left(1 + \frac{\rho_s M_w D_{dry}^3}{M_s \rho_w (D_p^3 - D_{dry}^3)}\right)^{-1} \tag{5.5}$$

$$x_w = \left(1 + \frac{\rho_s M_w}{M_s \rho_w} \left(GF^3 - 1\right)^1\right)^{-1} \tag{5.6}$$

For M_s and ρ_s the values derived from HR-Tof-AMS and APCI-MS measurements are used (210 g/mol and 1460 kg/m^3 see section 5.2.1).
It is more than likely that there is a large number of different organic compounds in the particles. But as no information on the exact number of different compounds in the solution is available, it is assumed that only one organic component exists in the aerosol particles. The variations in $\phi(a_w)$ due to the interaction of different compounds will be attributed to this single molecule. To fit the x_w/a_w data calculated from the measurements, the contribution of the functional groups to this molecule is varied. The occurrences of the functional groups are not limited to integer values, i.e. the sum of functional groups does not add up to a real existing molecule, but rather to a hypothetical compound representing the properties of the aerosol particles. For the fitted hypothetical molecule a_w can be calculated for $0 < x_w < 1$. To convert x_w back into GF equation 5.6 is solved for GF. The dry diameter can be chosen freely as GF is a relative quantity.
This method was used to fit each growth curve individually (see appendix A.2) and to calculate the average growth curve for the grouped data. The parameters for each group (1 - 6 and 1j - 6j) are listed in Table 5.5. The resulting averaged growth curves are shown in Figures 4.1 to 4.8 together with the measured data and for better comparison the six curves derived from BMT and α-pinene experiments are shown without the measured data in Figure 5.8.

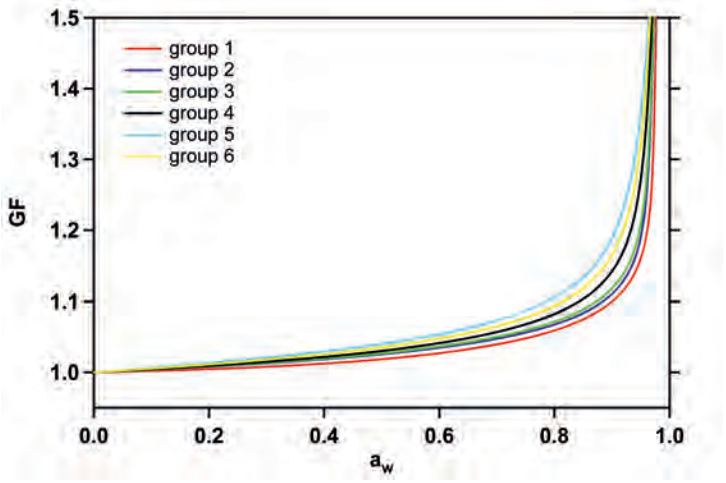

Figure 5.8: *Fitted growth curves of the 6 groups identified in the BMT and α-pinene experiments.*

Table 5.5: *UNIFAC fitting parameters for the groups 1 - 6 and 1j - 6j. The errors are the fitting errors of the parameters.*

group	CH_3	CH_2	CH	C	COOH	CH_3CO	CH_2CO	CHO	OH
1	2.13 ± 0.02	0 ± 0	0 ± 0	0 ± 0	0 ± 0	1.93 ± 0.06	0 ± 0	0 ± 0	0.36 ± 0.02
2	0 ± 0	0 ± 0	0 ± 0	4.80 ± 0.02	2.99 ± 0.01	0 ± 0	0 ± 0	0 ± 0	0 ± 0
3	0 ± 0	0 ± 0	2.39 ± 0.03	2 ± 0	2.69 ± 0.01	0 ± 0	0 ± 0	0 ± 0	0 ± 0
4	0 ± 0	0 ± 0	1.98 ± 0.03	2 ± 0	2.84 ± 0.01	0 ± 0	0 ± 0	0 ± 0	0 ± 0
5	0.06 ± 358	0.52 ± 3476	1.34 ± 496	2 ± 0	0.87 ± 219	0 ± 0	0.54 ± 2181	0.41 ± 168	0.26 ± 345
6	0 ± 0	0.64 ± 17945	1.44 ± 44269	1.75 ± 31120	1.30 ± 195	0 ± 0	0.54 ± 6099	0.47 ± 1391	0 ± 0
1j	0 ± 0	0 ± 0	0 ± 0	4.32 ± 0.07	2.23 ± 0.05	0 ± 0	0 ± 0	0 ± 0	0 ± 0
2j	2.74 ± 0.05	0 ± 0	0 ± 0	0 ± 0	1.58 ± 0.03	0 ± 0	0 ± 0	0 ± 0	0 ± 0
3j	0 ± 0	0 ± 0	1.22 ± 7786	3.16 ± 9217	2.54 ± 234	0 ± 0	0 ± 0	0.006 ± 107	0 ± 0
4j	0 ± 0	0 ± 0	0 ± 0	4.05 ± 0.12	2.56 ± 0.08	0 ± 0	0 ± 0	0 ± 0	0 ± 0
5j	0 ± 0	0 ± 0	0 ± 0	4.08 ± 0.13	2.75 ± 0.09	0 ± 0	0 ± 0	0 ± 0	0 ± 0
6j	0 ± 0	0 ± 0	1.70 ± 15473	3.90 ± 2485	0.61 ± 887	0 ± 0	0.58 ± 7657	0.5 ± 660	0.74 ± 0.50

The RH range from 50% to 97.5% was used for the fitting as all measurements covered this range. Up to 97.5% RH the data is represented very well by the averaged growth curves even though the errors of the parameters for group 5, 6, 3j, and 6j are several orders of magnitudes larger than the actual parameters, i.e. the group composition is not well defined. For groups 1 - 3 the fit overestimates GF at RH higher than 98%. For the groups identified in the JPAC experiments this cannot be verified as there are no valid data points above 97.5%. The overprediction in $GF(RH)$ is caused by an overestimation of $\phi(a_w)$ as the minimum of $\phi(a_w)$ is predicted at too low a_w and the following increase is too steep.
The reason for this can be related to the availability of data for the fitting algorithm in the critical parts of the curve. For groups 1 and 2 the measured $\phi(a_w)$ curves are the lowest and have not reached their minimum. For group 3 only very few data points with a rather wide spread show the upward trend. The calculations with the surrogates (section 5.2.2) show that for absolutely lower $\phi(a_w)$ curves the minimum should be rather sharp. With the few available data points the fitting algorithm is unable to determine the correct position of the minimum, and due to the steepness of the $\phi(a_w)$ function the deviation of the derived growth curve is significant. Alternatively, it may well be that the UNIFAC model is unable to fit the course of the $\phi(a_w)$ curve as the general properties of the solution change. If below 98% RH the particle was not dissolved completely and an additional, less hygroscopic compound was dissolved in the solution above 98%, the measured GF above 98% RH would be lower than predicted. As the UNIFAC model is set up with only one type of organic molecules, such behavior could not be fitted.

Table 5.6: *M_s and O/C ratio from the free UNIFAC fit. No constrains were applied to the occurrence of the functional groups.*

group	M_s [g/mol]	O/C
1	121	0.38
2	192	0.77
3	195	0.79
4	177	0.83
5	166	0.50
6	147	0.56
1j	152	0.68
2j	112	0.73
3j	168	0.73
4j	164	0.78
5j	173	0.81
6j	148	0.39

Although the calculated fit does not represent a "real" organic compound, the M_s and O/C ratio can be calculated (see Table 5.6) and intercompared for the different hygroscopicity classes. The calculated M_s are in the range of the MT oxidation products identified by *Larsen et al.* (2001). But the M_s value of 210 g/mol used to calculate ϕ is not reached. The O/C ratio increases for groups 1 to 4 and

1j to 5j. But the groups with the highest particle hygroscopicity (5, 6, 6j) have rather low O/C ratios.
As shown in section 5.2.2 the O/C ratio can only be used to compare particle hygroscopicity when looking at similarly composed compounds. Thus, the BMT experiment data is fitted with a restricted model allowing only CH_2 and COOH groups. The fit parameters and calculated M_s and O/C ratios are listed in Table 5.7. The quality of the fit is reduced, but it is still sufficiently good. With these restrictions the increasing particle hygroscopicity is correlated with increasing M_s and O/C increase. But M_s is even further away from the value deployed for the initial calculation of ϕ and x_w from GF and RH.

Table 5.7: *Fitting parameters, M_s, and O/C ratio from restrained UNIFAC fit. Only CH_2 and COOH groups were used.*

group	CH_2	COOH	M_s [g/mol]	O/C
1	3.21 ± 0.02	1.62 ± 0.01	118	0.67
2	3.60 ± 0.02	2.05 ± 0.01	142	0.72
3	3.57 ± 0.02	2.13 ± 0.01	146	0.75
4	3.26 ± 0.02	2.27 ± 0.01	148	0.82
5	3.11 ± 0.05	2.53 ± 0.02	157	0.90
6	2.97 ± 0.05	2.80 ± 0.02	167	0.97

5.2.4 Prediction of CCN activation

a_w calculated for the fit must be converted back to RH (or rather S) with equation 4.2 to determine the activation point for the fitted growth curves.

$$S = \frac{RH}{100} = a_w \cdot exp\left(\frac{4M_w\sigma_w}{R\,T\rho_w\,GF\,D_{dry}}\right) \tag{5.7}$$

In this context D_{dry} from HTDMA measurements and $D50$ from CCN-C measurements describe the same quantity: the dry diameter of the particles that are activated. With equation 5.7 SS_{crit} for any dry particle diameter can be derived from a_w calculated with UNIFAC. In Figure 5.9 the predicted curves are shown extrapolated to the activation point($D50 = 100$ nm). Despite the quite different course of the growth curves in the sub-saturated regime all groups predict almost the same SS_{crit}.
The position of the activation point is described by equations 2.29 and 2.30. Applying the definition of ρ_{ion} (equation 2.13) to equation 2.30 leads to:

$$\begin{aligned} SS_{crit} &= p_0 \cdot D_{dry}^{-\frac{3}{2}} \\ &= \left(\frac{2.56 \cdot 10^6 M_w^2}{27R^3T^3\rho_w^2} \cdot \frac{\sigma^3 M_s}{\phi_{crit}\,\nu\,\rho_s}\right)^{\frac{1}{2}} \cdot D_{dry}^{-\frac{3}{2}} \end{aligned} \tag{5.8}$$

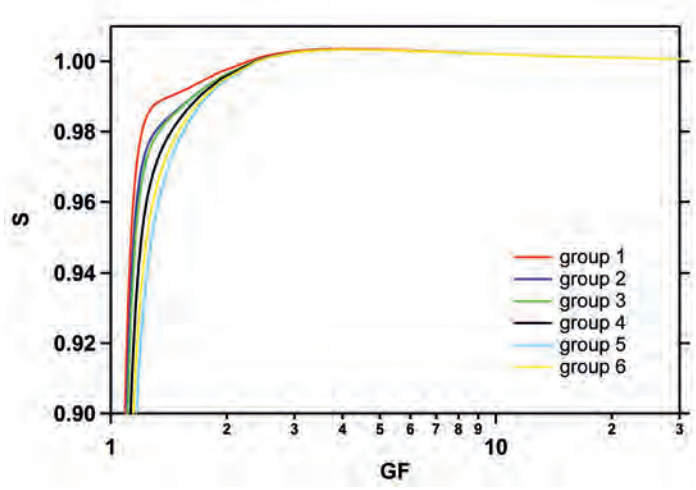

Figure 5.9: *Extrapolation of growth curves of the 6 groups identified in the BMT and α-pinene experiments to the activation point with D50 = 100 nm. The GF axis is in logarithmic scale*

ϕ_{crit} is the value of ϕ at the activation point. For a given dry particle diameter SS_{crit} depends on the parameter p_0. Assuming that the dissociation (ν), the molar mass (M_s), and the density (ρ_s) of the solute are constant, the ratio of $SS_{crit,1}$ and $SS_{crit,2}$ calculated with two different values $\phi_{crit,1}$ and $\phi_{crit,2}$ equals:

$$\frac{SS_{crit,1}}{SS_{crit,2}} = \sqrt{\frac{\phi_{crit,1}}{\phi_{crit,2}}} \tag{5.9}$$

Groups 1 and 6 are used to estimate the maximum difference in predicted SS_{crit} as they exhibit the largest difference in ϕ_{crit} (0.964 and 0.982, respectively). In this case $SS_{crit,1}$ is larger than $SS_{crit,2}$ by a factor of 1.009. A 100 nm particle then activates at 0.336% instead of 0.339% SS. This difference is less than the uncertainty in SS set in the CCN-C.

This behavior is due to the fact that at the activation point the properties of the droplet are governed by the Kelvin effect. As the UNIFAC model calculates the non-ideality in the solution, it solely influences the Raoult term. The implication of these findings is that different hygroscopic behavior in the sub-saturated regime will always predict the same SS_{crit} as long as $\frac{\sigma^3 M_s}{\nu \rho_s}$ is constant. On the other hand two identical growth curves will predict different SS_{crit} if the absolute value of the quotient changes. Closure between measured CCN-C and HTDMA data can be achieved by adjusting $\frac{\sigma^3 M_s}{\nu \rho_s}$. The $D50/SS_{crit}$ data from the CCN-C is used to determine the value of the quotient. The value for σ was assumed (e.g. σ_w) and $\frac{M_s}{\nu \rho_s}$ was used to calculate ϕ from the HTDMA data. The resulting curve was fitted as described above and the correct SS_{crit} was predicted.

For an independent prediction of CCN activity from HTDMA data the particle density and average molecular weight must be known. The effective density of the particles is calculated from HR-Tof-AMS and SMPS measurements

(*Spindler* (2010), see Figure 5.10). In all experiments the density increases continuously from the initial value of ∼1350 kg/m^3 to the final value between 1500 and 1700 kg/m^3. The spread within each data set is larger than the variations between the experiments. From APCI-MS measurements the average M_s is estimated to be between 150 and 350 g/mol. For the surface tension of the droplet the value for pure water is assumed. Then the lower and upper limit for ϕ calculated from hygroscopic growth data is obtained using the two combinations 350 g/mol/1350 kg/m^3 and 150 g/mol/1700 kg/m^3. This corresponds to ρ_{ion} of 3857 and 11333 mol/m^3, respectively (for $\phi = 1$ and $\nu = 1$). The $\phi(a_w)$ curves calculated with these extreme values for $\frac{\sigma^3 M_s}{\nu \rho_s}$ are fitted with the UNIFAC model and the activation point is predicted. In Figure 5.11 the upper and lower limit for the prediction of SS_{crit} from HDMA data are shown (dark and light green line) together with the data measured with the CCN-C (colored diamonds). The prediction using the UNIFAC model and any combination of M_s and ρ_s is always closer to the measured CCN activity than the prediction using a constant κ (black triangles).

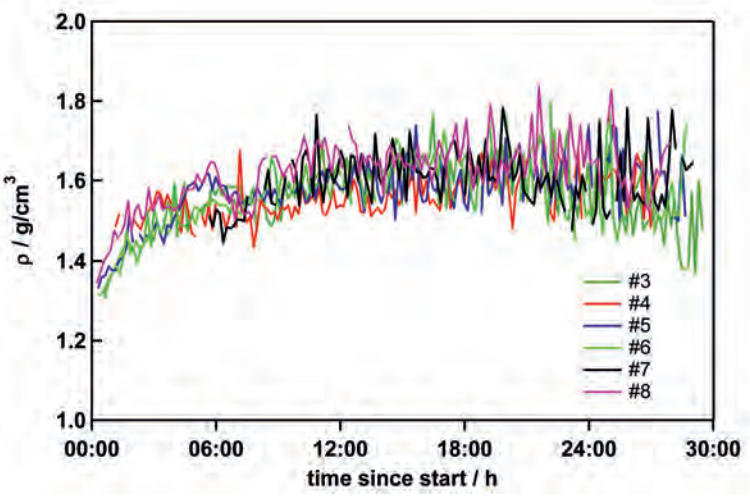

Figure 5.10: *Effective particle density ρ calculated with equation 3.25 from SMPS and AMS data (Spindler (2010)).*

With this approach we tried to explain the observed deviation from ideal Koehler theory solely by the non-ideal behavior of the solution in the droplet at subsaturation. Although the thermodynamic model applied was rigorous, it turned out that de facto the approach is equivalent to the ones presented above using surface tension reduction (section 5.1.3) or limited solubility (section 5.1.2) with a constant hygroscopicity factor κ. It is more than likely that all three factors (surface tension, solubility, ideality) play a role in the droplet and that their contribution depends on the solute concentration in the droplet. Through equation 5.8 the parameters are linked, and by assuming (or using measured) values for two of them the other one can be calculated. For each new set of σ_w and $\frac{M_s}{\nu \rho_s}$ the $\phi(a_w)$ curve can be calculated from the HTDMA data. If the activation data is

used to determine σ_w and $\frac{M_s}{\nu\rho_s}$, the predicted SS_{crit} will always match the CCN-C measurements.

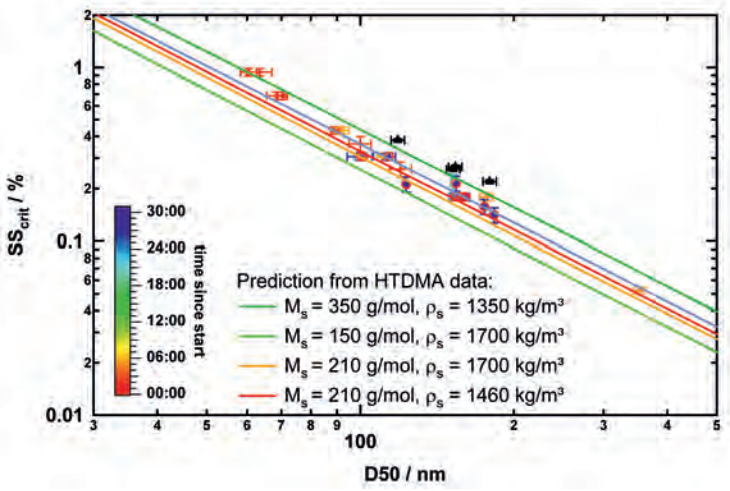

Figure 5.11: *Measured and predicted D50/SS_{crit} for experiment 3. Colored diamonds: measured CCN-C data, blue line: fit to this data with equation 2.29, black triangles: SS_{crit} predicted from κ(90%), colored lines: prediction applying the UNIFAC model with different values for M_s and ρ_s (see legend)*

Irrespective of the thermodynamic implications discussed above the fitting with the UNIFAC model is a powerful tool to calculate the average growth curve for both a single and several measurements.

5.3 Influence of the experiment conditions on the properties of the formed SOA

In section 5.1 and 5.2 it was shown that the CCN activity of aerosol particles depends on the combination of M_s, ρ_s, and σ_s. Overall, the variations of the hygroscopic growth data did not necessarily influence the activation behavior. In detail these variations can reveal information about the influence of the oxidation conditions on the chemical composition of the particles and the manifestation in hygroscopic growth and CCN activation.
The formation and composition of SOA particles depends on several different factors. In the SAPHIR chamber some of them were held constant (initial NO_x, O_3 and water concentration). Others were varied intentionally (initial VOC concentration, composition of the mixture). As SAPHIR is an outdoor chamber, the photochemical activity (photolysis and OH formation) depends on the natural solar radiation. In principle, all of these changing conditions should influence the chemical and microphysical properties of the formed particles. In the following sections the changes in reaction conditions are compared to the observed differences (or similarities) between measurements of hygroscopic growth and CCN activity.

5.3.1 Oxidant to VOC ratio

There are two major processes in the SAPHIR chamber competing to oxidize the VOCs: ozonolysis and reaction with OH radicals. Experiment 8 was conducted in the dark chamber and with enhanced O_3 concentration so that ozonolysis clearly dominated in the VOC oxidation. Since the particles formed in the dark chamber exhibited the lowest hygroscopicity and CCN activation, it can be concluded that SOA consisting almost completely of ozonolysis products are less hygroscopic than SOA containing a significant fraction of photo-oxidation products. The actinic flux on an overcast day is already enough to increase the hygroscopicity of the particles (compare experiment 8 (ozonolysis) and 5 (overcast) in Table A.1).
The relative importance of the two oxidation processes depends on the radiation conditions. As OH radicals are formed from photolysis of HNO_2 and O_3 (via O^1D and subsequent reaction with H_2O), increasing illumination of the chamber will increase the production of OH. The ozonolysis is a non-photochemical process (i.e. no radiation is needed to enable the reaction). However, one has to consider that apart from the initially added O_3, it is also formed photochemically by reaction of NO with peroxy radicals. Thus, increasing radiation will increase the photochemical production of O_3. An increasing O_3 concentration will enhance the turnover of VOC by ozonolysis. But the OH concentration increases due to the photolysis to O^1D as well. Therefore, at the NO_x level present in the experiments an increase of the actinic flux will favor the OH reaction path over the ozonolysis.
The best way to quantify the effect of the OH concentration over a longer time period, is to measure the OH dosage present during the experiments. Due to the low NO_x level in all experiments, the OH steady state concentration was below the detection limit of the used differential optical absorption spectrometer on the first day of most experiments. Hence, the primary production of OH from O_3 photolysis is calculated as a proxy for the oxidation potential. The primary production rate of OH ($P(OH_{pot})$) depends on the formation of O^1D, the consecutive reaction with H_2O, and the quenching of O^1D with N_2 and O_2 (*Hofzumahaus et al.* (1992), rate constants from *DeMore et al.* (1997)).

$$P(OH_{pot}) = \frac{k_1 \cdot [H_2O]}{k_2 \cdot [N_2] + k_3 \cdot [O_2] + k_1 \cdot [H_2O]} \cdot 2 \cdot j(O^1D) \cdot [O_3] \qquad (5.10)$$

k_1 :	rate constant for reaction with H_2O	$2.2 \cdot 10^{-10}$ cm^3/s
k_2 :	rate constant for quenching with N_2	$2.6 \cdot 10^{-11}$ cm^3/s
k_3 :	rate constant for quenching with O_2	$4.0 \cdot 10^{-11}$ cm^3/s

By integrating $P(OH_{pot})$ over the time interval from experiment start to the end of each HTDMA measurement the concentration of OH produced from O_3 photolysis ($[OH_{pot}]$) is calculated. The values for experiment 3 and 5 are given in Table 5.8 together with the integrated $j(O^1D)$ and $[O_3]$. For 1000 ppbC VOC concentration three radiation conditions were investigated (# 8 dark chamber, # 5 cloudy, # 3 bright). For all measurements of experiment 3 the integrated $j(O^1D)$ and $[O_3]$ are already a factor of 2.2 - 2.7 larger than those determined for experiment 5. The $[OH_{pot}]$ is also larger (by a factor of 4.7 - 5.4). Thus, the higher hygroscopicity

for SOA formed under bright conditions can be attributed to the much higher $[OH_{pot}]$ level.

Table 5.8: *Integrated $j(O^1D)$, $[O_3]$, and potential OH ($[OH_{pot}]$) for experiment 3 and 5.*

exp.	meas.	$\int j(O^1D)$	$\int [O_3]$	$[OH_{pot}]$ / 10^{10} cm^{-3}
# 3	1	0.255	623342	8.1
	2	0.294	1131903	10.5
	4	0.506	4027854	18.9
	5	0.629	4560468	18.9
# 5	1	0.104	278976	1.7
	2	0.119	421166	1.9
	3	0.119	490075	1.9

As the influence of the irradiation can be quantified with $[OH_{pot}]$, the influence of varying the gas-phase precursor concentration can be investigated. With the pure standard BMT mixture experiments with 500 ppbC and 1000 ppbC were conducted under bright conditions (# 1 and # 3). All measured growth curves are very similar (classified in group 4). Only the last measurement of # 3 exhibited slightly lower GF. The CCN-C measurements show a 30% lower κ for the experiment 1 with only 500 ppbC BMT. (For general explanations of the discrepancies of CCN-C and HTDMA measurement see section 5.1.) When only 3 x 40 ppbC BMT were used, both, the HTDMA and CCN-C, measured much higher hygroscopicity than for 500 and 1000 ppbC.

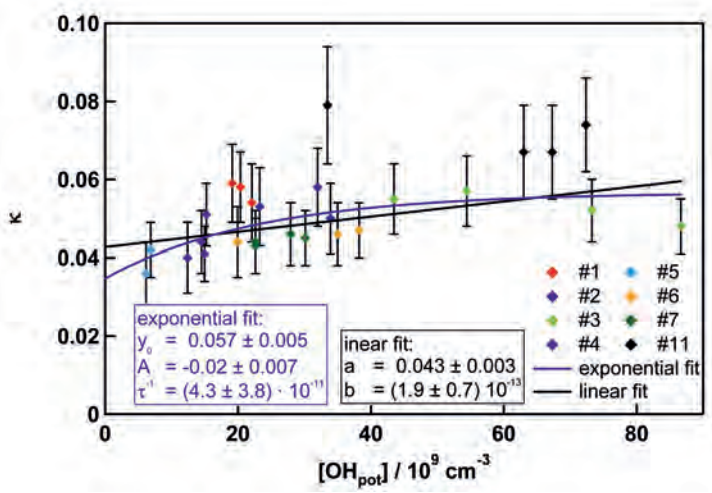

Figure 5.12: *Measured $\kappa(90\%)$ vs. calculated $[OH_{pot}]$. Each experiment is represented in one color (see legend in graph). The data is fitted with $\kappa = a + b \cdot [OH_{pot}]$ (black line) and $\kappa = y_0 + A\, exp(-[OH_{pot}]/\tau)$ (blue line).*

To separate the influence of the different irradiation during the experiments, $j(O^1D)$, $[O_3]$, and $[OH_{pot}]$ are calculated for each measurement (see Table A.3).

In Figure 5.12 κ derived for 90% RH (as listed in Table A.1) are mapped versus the integrated $[OH_{pot}]$ of each measurement. Fitting the data of all the experiments with a linear ($\kappa = a + b \cdot [OH_{pot}]$) or exponential function ($\kappa = y_0 + A\, exp(-[OH_{pot}]/\tau)$), leads to large error in the fit parameters thus indicating a poor correlation between hygroscopic growth and oxidation potential. Moreover, a detailed examination of single experiments reveals no obvious connection. Experiment 1 exhibits much lower $[OH_{pot}]$ than experiment 3 even though they show almost the same hygroscopic growth (both are classified group 4). The low concentration experiment (# 11), which produced by far the most hygroscopic particles, lies in the same range as experiment 3.
To include the gas-phase precursor concentration, $[OH_{pot}]$ is scaled with the initially added amount of VOCs in ppbC ($[VOC]^0$).

$$[OH^s_{pot}] = [OH_{pot}]/[VOC]^0 \tag{5.11}$$

These values are listed in the last column in Table A.3. In Figure 5.13 $\kappa(90\%)$ is plotted versus $[OH^s_{pot}]$. There is a clear correlation for the whole data set. The $[OH^s_{pot}]$ values for experiment 1 and 3 (500 and 1000 ppbC VOC) fall closely together (red and green diamonds, respectively). Corresponding to the largest GF the low concentration experiment (#11) exhibits the largest $[OH^s_{pot}]$ values (black diamonds).

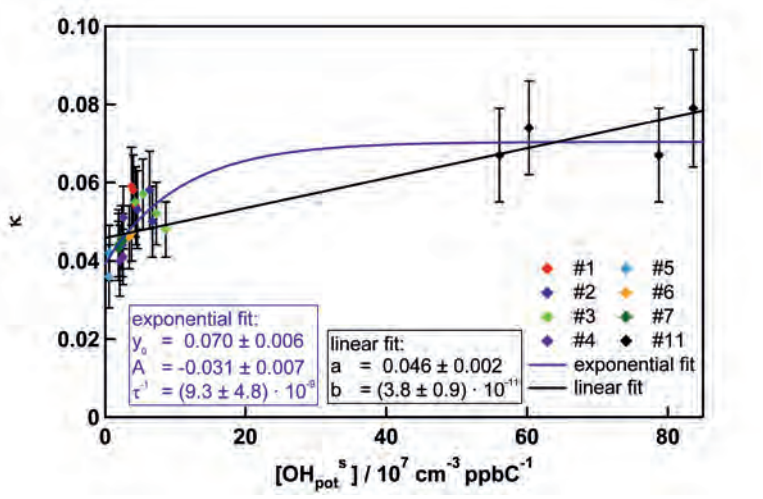

Figure 5.13: *Measured $\kappa(90\%)$ vs. calculated $[OH_{pot}]$. Each experiment is represented in one color (see legend in graph). The data is fitted with $\kappa = a + b \cdot [OH^s_{pot}]$ (black line) and $\kappa = y_0 + A\, exp(-[OH^s_{pot}]/\tau)$ (blue line).*

The κ vs. $[OH^s_{pot}]$ data can be fitted very well with an exponential fit. The parameters for the fit are included in Figure 5.13. This result has two implications. First, the observed increase in hygroscopicity and CCN activation at low [VOC] can be attributed to increasing the OH to VOC ratio. In experiment 1 only half of $[VOC]^0$ was applied, but $[OH_{pot}]$ was also reduced by a factor of 2 (first day) to 4 (second day). Thus, no change in $[OH^s_{pot}]$ and hygroscopic growth was observed

on the first day. Second, the $\kappa([OH^s_{pot}])$ function shows saturation, i.e. above a further increase of $[OH^s_{pot}]$ will not or only slowly increase κ. The OH radical concentration seems to be no longer the limiting factor of the evolution of the hygroscopic properties in time. In the low concentration experiment (# 11) the OH steady state concentration was measured to be as high as $1.4 \cdot 10^7$ molecules per cm^3. This is an order of magnitude higher than the maximum observed in all other experiments.
As experiment 8 was conducted in the dark chamber, the OH production due to photochemistry is 0. These data points were not considered for the fitting. From the fitting parameters the value of κ at $[OH^s_{pot}] = 0$ is calculated to be 0.040±0.006. This is the same within errors as the κ of 0.038 measured for the ozonolysis experiment.

5.3.2 Chemical composition of the gas-phase precursors

The basic composition of the gas-phase precursors is the BMT mix (an equal mixture of α-pinene, β-pinene, limonene, ocimene, Δ-3-carene), which supposedly is simulating the emissions of a boreal forest. To mimic different stress levels of a boreal forest, experiments were conducted with the BMT mixture without ocimene and with 13% SQTs added (α-humulene and β-farnesene).
No significant trend could be attributed to the change in the chemical composition of the precursors. Apparently, the conducted variations in composition were too small to influence the hygroscopic properties of the formed particles in a detectable way. The case of JPAC experiments will be discussed below (section 5.5.1). This is promising for atmospheric applications since details of the biogenic VOC precursor mix seem to be unimportant for prediction of microphysical properties of biogenic SOA.

5.4 Aging of SOA

5.4.1 Discussion of the general trends in the BMT experiments

One of the objectives of this study was to investigate the influence of chemical aging on the microphysical properties of biogenic SOA. Overall, there is no obvious common trend. In some experiments the hygroscopic growth increased on the first day and decreased again on the second (# 2 and 3) while the CCN activation ability increased monotonously. On the other hand, during experiments 5, 6, and 7 the CCN activation decreased while the hygroscopic growth increased on the second day. Moreover, there is no direct relation of this behavior to the precursor conditions (i.e. presence of SQT or ocimene).
These observations seem to contradict the correlation of κ and the potential OH scaled with [VOC] found in the previous section. A higher $[OH^s_{pot}]$ should lead to larger κ values (for $[OH^s_{pot}] < 3 \cdot 10^8$, see Figure 5.13). $[OH^s_{pot}]$ can only increase with time. Thus, an increase (or remaining constant) of κ would be expected during each experiment. Even if κ was close to the saturation limit, no decrease of κ should occur.

From HR-Tof-AMS measurements there is information about the temporal evolution of chemical and physical properties of the particles. *Spindler* (2010) demonstrated that both the effective particle density and the O/C ratio increase with time (see Figures 5.10 and 5.14). Except for the ozonolysis experiment (# 8), where the increase of the O/C ratio is much slower, the time evolution is similar for all experiments. Therefore, the parallel evolution of the hygroscopic properties for all experiments would be expected. But the CCN activation depends on the quotient $\frac{\sigma^3 M_s}{\nu \rho_s}$. If only the density of the particles increases, SS_{crit} will decrease, i.e. the CCN activity increases (see red and orange lines in Figure 5.11). But if M_s increases as well, the CCN activation could stay constant or even decrease. If the components in the particle become more surface active, σ_s will also decrease and consequently the particles will become less CCN active. In the sub-saturated regime the non-ideality of the compounds is dominant (Raoult term in Koehler equation), but this is not necessarily correlated to $\frac{\sigma^3 M_s}{\nu \rho_s}$.

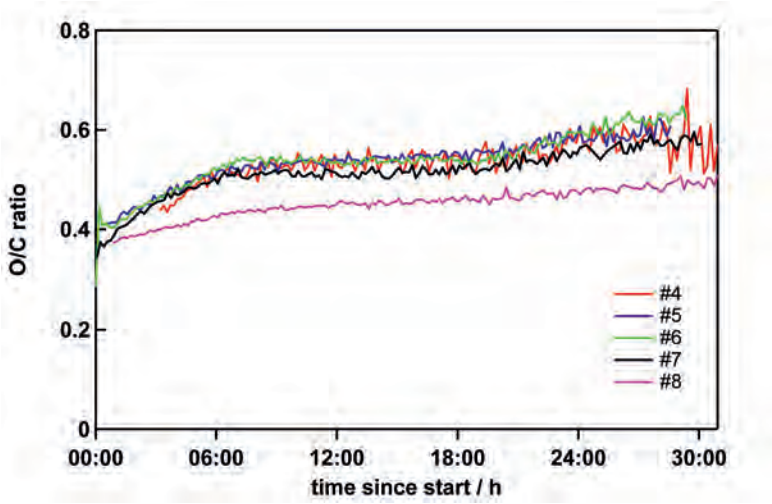

Figure 5.14: *O/C ratio calculated from HR-Tof-AMS data (Spindler (2010)).*

All except one HTDMA measurement were full humidogram measurements, i.e. the SOA particles were probed four to five times with several hours in between. In the exceptional measurement the HTDMA was set to a constant RH of (92.2±0.15)% and GF was measured for 120 nm particles during the first three hours of experiment 7. κ calculated from that data is shown in Figure 5.15. After an initial steep increase the curve levels off. The temporal behavior of κ can be fitted very well with an exponential function. Although only the data points of the measurement with the fixed RH are used for the fit, the κ values derived from the later humidogram measurements (green diamonds in Figure 5.15) are predicted correctly. Assuming that this behavior is representative for all experiments of type A, it can be concluded that during the first three hours of the experiments the major changes occur in the particles causing a significant increase in hygroscopicity. Generally, the humidogram measurement started 1 to 2h after the start of the experiments and took up to 2.5h. Due to the intrinsically small GF of SOA changes are only visible for higher RH (>∼85%). As

the highest RH are reached at the end of each measurement, only the last part of the initial aging can be captured. If the initial aging is slow, κ will not have reached its final value when the first humidogram is measured. As a consequence the second measurement should show an increase in the hygroscopicity.

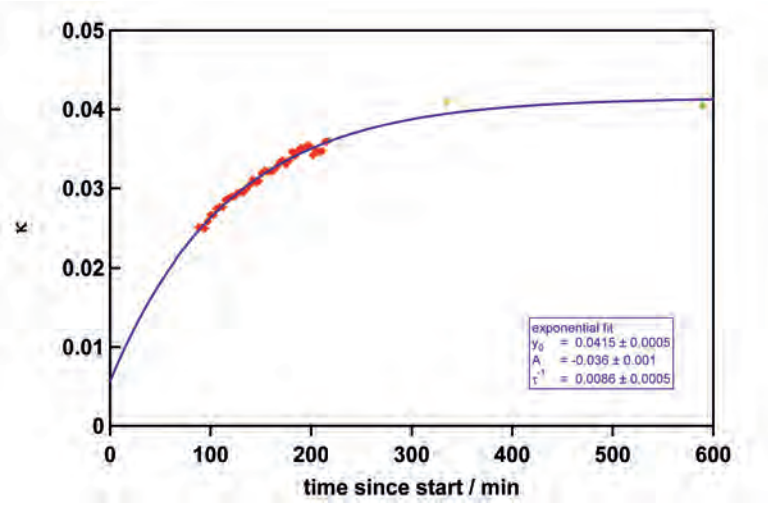

Figure 5.15: *κ(92%) measured during the first hours of experiment 8. The 1 σ standard deviation of the measured RH was $\pm$0.15%. Red: measurement with fixed RH, green: data points from full humidogram measurement.*

The CCN-C was operated continuously beginning with the start of the experiment. However, as the initially formed particles were very small, they could not be activated at the available SSs set in the CCN-C until 1 or 2h after the particle formation started. The period until the particles grew to sufficient size to be activated depended on the condensational growth rate of the particles. Again, experimental conditions determined if observations during the first hours of the experiment could be evaluated.
There are two processes that can explain the fast increase in hygroscopicity in the beginning of the experiments. Either an increasing amount of compounds with a higher hygroscopicity is introduced into the particles (either from gas phase or heterogeneous reactions) or less hygroscopic compounds evaporate from the particles. If high precursor and oxidant concentrations are used in chamber experiments, primary reaction products will be produced fast and their concentration is high. Compounds with low volatility will always reside in the particle phase. But the partitioning of the semi-volatile compounds will be favored by fast formation as they can reach large super-saturations. If OH radicals are present, the primary reaction products will continue to react. As no new VOCs are added to the chamber, the gas-phase concentration of the semi-volatile intermediate will be diminished as they react with OH. The gas/particle partitioning will adjust continuously according to the new gas-phase concentration reducing the amount of semi-volatiles in the particles and condensing more higher order oxidation products. Generally, for a molecule with roughly the same hydrocarbon backbone the

volatility decreases with increasing functionality. Thus, reducing the amount of semi-volatile compounds will increase the O/C ratio.
As this reduction of semi-volatiles is related to further oxidation of the intermediates in the gas phase and the reaction with O_3 is limited to C-C double bonds, it should correlate with $[OH^s_{pot}]$. The higher $[OH^s_{pot}]$ the faster the semi-volatile intermediates should be consumed and the faster the initial change is completed. The next generation of products is most likely less volatile, therefore, they will condense on the particles and increase the oxidation grade of the particle even further. Hence, the two processes are connected to $[OH^s_{pot}]$ in the same way.
As described above, the faster the change the less the instrumentation will be able to capture it. Therefore, experiments with low $[OH^s_{pot}]$ (# 4, 5, and 6) show a monotonous increase in κ derived from HTDMA measurements while κ varied only slightly in experiments with very high $[OH^s_{pot}]$ (# 1, 2, and 3). This is also supported by the fact that experiments 4 to 6 started with significantly lower κ. The data from CCN-C measurements indicates the opposite relation. Experiments 1 to 3 show a significant increase in κ on the second day and in # 6 the initially κ is higher than in # 1 to 3. Furthermore, a significant decrease is observed for experiment 6.
To minimize the effect of semi-volatiles being forced into the particle phase, experiment 11 was started with only 40 ppbC BMT. The hygroscopic growth was significantly higher than for all other experiments while the CCN activity was average. This corresponds to the findings of *Juranyi et al.* (2009). Also *Duplissy et al.* (2008) observed concentration dependence of the hygroscopic growth, but also in CCN activation. But the increase in hygroscopicity is much higher in those studies (up to $\kappa = 0.13$) whereas the maximum κ from HTDMA measurements observed here was 0.079. After the second portion of 40 ppbC BMT was added the hygroscopicity and CCN activation decreased significantly. The oxidation condition for the fresh VOCs is almost the same as for the first portion. This proves that the first product generation that will enter the particle phase is less hygroscopic than those present in the particles after 3 h of photochemical and ozonolysis reaction.

5.4.2 Implications of the α-pinene experiments

The setup of the α-pinene experiments allowed further investigations on the processes contributing to chemical aging. In all experiments (# 20 - 22) pre-existing seed aerosols were produced by ozonolysis reaction of α-pinene. The initially added VOC concentration was reduced to less than the detection limit of the PTR-MS (<0.01 ppbC) before the photochemistry was started by opening the roof of the SAPHIR chamber. The CCN activity of particles generated by ozonolysis of α-pinene is higher than measured during the BMT experiments. But it has to be noted that only mixing ratios of 100 and 400 ppbC α-pinene were used here. With the beginning of the photochemistry the CCN activation increases even further. After 4.5 h of illumination the chamber was dark for 18 h. During the dark period the hygroscopicity was constant. A possible explanation for this is that α-pinene has only a single C-C double bond that can react with O_3 . For any further reactions (and thus changes in composition of the particles) OH is needed. As NO_x was low, NO_3 chemistry in the dark can be neglected. The

ozonolysis produces a small quantity of OH but as soon as the MT is consumed completely, this source ceased. That OH radicals are responsible for the observed aging can be deduced from experiment 22. Here 300 ppm of CO were added before the opening of the roof in order to shift the HO_x equilibrium almost completely towards HO_2. Without the OH a slight decrease in CCN activation is observed. This excludes a major role of HO_2 in the aging process.
In the HTDMA the α-pinene ozonolysis particles exhibit a different growth behavior than all other SOA particles (see section 4.2.1). A minimum of the growth curve is observed between 0.45 and 0.48 a_w (see Figure 4.7). This feature is persistent in the dark chamber, but is smoothed out when the SAPHIR chamber is illuminated for a certain time. This also happens if CO is present. Pure ozonolysis particles are solid containing voids (see section 4.2.1). Condensation of vapors restructures the particles filling the voids. This process is independent of the chemical composition of the condensing vapors, i.e. the gas-phase reaction that produced it. But if OH is present, more condensable vapor is produced (higher condensational growth rate of the particles). Thus, the restructuring should happen faster and monotonous hygroscopic growth should be measured with the HTDMA.

5.5 Transfer to JPAC data

The discussion presented above is based on the SAPHIR chamber experiments. In this section the data gathered in JPAC is evaluated in regard to the same aspects.

5.5.1 Influence of the oxidation pathway

First vs. second particle formation

The course of the experiments was quite different from that in the SAPHIR chamber and therefore considered first. In the BMT experiments O_3 and OH were added to the chamber within minutes, as the chamber roof was opened as soon as the O_3 addition was finished. Photochemistry started immediately. In JPAC experiments, however, O_3 was already present in the RC, and the VOCs could react with O_3 for several hours before the UV light was switched on. No particle formation took place and the ozonolysis products stayed in the gas phase. Only when OH was produced particle formation took place. The ozonolysis products were also oxidized by OH and could contribute to the nucleation and growth of the new particles.
The particles from this first nucleation burst were flushed out of the RC continuously. This caused a reduction of the total particle surface which was available as a sink for the condensable vapors. VOCs continuously enter the RC and the photochemical oxidation produced condensable vapors. Once the available total particle surface was small enough, this generated a super-saturation of VOC oxidation products, and new particles were formed. The interplay of photochemical production of vapors, generating and reducing the condensational sink by nucleation and flush out of particles generated a quasi steady state system with continuously ongoing new particle production. As there were no precondition

vapors from ozonolysis, the oxidation grade in the particles was lower. Since a higher grade of oxidation in the organic compounds is generally correlated with higher hygroscopicity and CCN activation, this explains the measured differences between the less hygroscopic particles from the second and more hygroscopic particles from the first mode. Note that the JPAC experiments were still different from the SAPHIR experiments of type B, where particles were already formed from the ozonolysis products.

VOC concentration

As shown in section 5.3.1, $[OH_{pot}]/[VOC]$ is an important parameter to characterize biogenic SOA. In JPAC a UV lamp is used for OH production. During the experiments, the irradiation was constant. As the O_3 concentration varied only slightly, the produced OH concentration was the same for all experiments. As this chamber was run as a continuous flow reactor and $[O_3]$ and water vapor concentration were held at a constant level, the OH production was the same for the course of each experiment. Therefore, the OH to VOC ratio depends solely on the VOC concentration entering the RC. In Figure 5.16 the average VOC concentrations measured with the GC-MS system are displayed. The identified compounds are classified into MT, SQT, and oxidized MT (OMT).

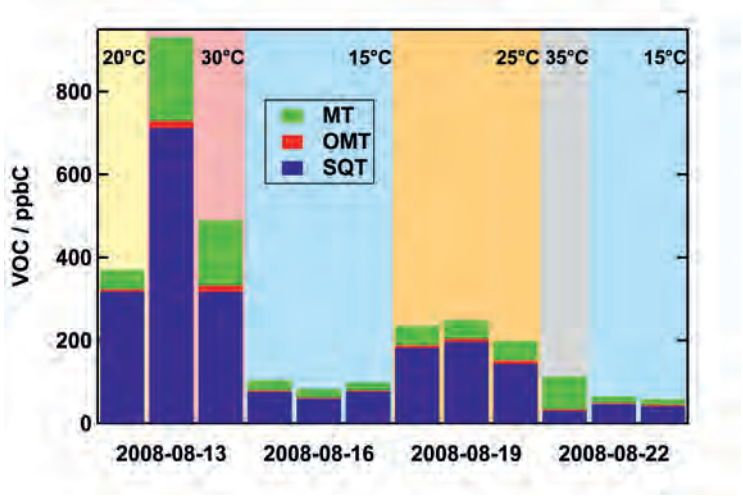

Figure 5.16: *[VOC] measured in JPAC sorted by experiment date. Background colors indicate the temperature in the PC. OMT: oxidized monoterpenes. The lights in the PC were off for the experiment at 35° C (gray background).*

In Table 5.9 the average VOC concentration and $\kappa(90\%)$ measured for first mode particles are listed. As the identified hygroscopicity groups 3j to 6j consist almost completely of measurements from the first mode, they can be used to simplify the comparison. j' indicates that the few later measurements are not regarded in the averaging. From group 3j' to 6j' the hygroscopicity increases and [VOC] decreases. This is equivalent to the trend observed in the BMT experiments. For

measurements from the second mode this trend is not as clear because the overall differences are much smaller.

Table 5.9: *κ(90%) and [VOC] for first mode particles.*

group	κ(90%)	[VOC] / ppbC
3j'	0.028	302.6
4j'	0.032	249.7
5j'	0.043	198.4
6j'	0.051	91.6

5.5.2 Chemical composition

Although the identified major components are the same in the BMT and JPAC experiments, they were observed in quite different ratios. In the JPAC experiments 64 to 85% of the emissions were SQT (related to ppbC) while in the BMT experiments only 13% SQTs were added. In the BMT experiments, both, adding SQTs or omitting ocimene in the precursor mixture only had a minimal effect. Overall, the differences observed in JPAC are small and the variability is explained by the initial VOC concentration. However, reducing the SQT contribution to the emissions to 25% or less increased the hygroscopicity and CCN activation.

The reason for this effect of SQTs can be explained by the chemical structure of the gas-phase precursors. Atmospheric oxidation of cyclic monoterpenes form mainly C_{10} or C_9 bi-functional compounds in the particle phase (*Larsen et al.* (2001)). Accordingly, the same number of oxidation steps would lead to C_{15} or C_{14} bi-functional products for cyclic SQTs (such as α-humulene). Due to the larger hydrocarbon backbone (hydrophobic part of the molecules) the hygroscopicity will be much lower than for C_{10} or C_9 compounds carrying the same functional groups (compare UNIFAC calculations in section 5.2). Thus, to reach the same hygroscopic growth and CCN activation, more oxidation steps are needed for introducing more functional groups. Acyclic SQTs (like farnesene) will be split into mono-functional compounds. The carbon chain length depends on the position of the split C-C double bond. But as only low-volatile compounds will end up in the particle phase and volatility increases with carbon chain length, the products found in the particle phase from this reaction will also have a low hygroscopicity. In total the same amount of SQT and MT will form less oxidized (and hence less hygroscopic) compounds after the same number of oxidation steps. Additionally, the average M_s of the products from SQT oxidation is larger. Hence, there are less molecules per volume solid SOA (when applying a constant effective density). This alone will decrease the measured hygroscopicity and CCN activity.

6. Summary and Conclusions

For a given aerosol size distribution the hygroscopic properties and cloud condensation nuclei (CCN) activation of aerosol particles determine their influence on the radiation budget of the atmosphere and thus on the climate. Especially, for particles near the critical activation dry diameter their composition determines if they are activated or not. Organic compounds provide up to 70% of the particle mass (*Zhang et al.* (2007)). In many environments these organic compounds are mainly products of the oxidation of biogenic VOCs (*Hallquist et al.* (2009)).
In this work, the hygroscopic growth and CCN activation of SOA particles formed by the oxidation of complex mixtures of biogenic emissions close to natural oxidation conditions were investigated. For this purpose SOA particles were produced in two different simulation chambers. In JPAC particles were produced from photo-oxidation and ozonolysis of VOC emissions from real trees. In the SAPHIR chamber pure α-pinene or a 1:1 mixture of α-pinene, β-pinene, limonene, ocimene, Δ-3-carene (BMT-mix) were used as gas-phase precursors. SOA was produced from the oxidation with O_3 and photochemically formed OH radicals. The hygroscopic growth of the formed particles was measured with a self-built HTDMA and the CCN activation with a CCN-C (DMT). The measured hygroscopic growth and CCN activation were analyzed applying different parameterizations of the ideal Koehler theory. The temporal evolution and relations to properties of the gas-phase precursors were studied. Furthermore, the hygroscopic growth measurements of the sub-saturated regime were compared to the CCN activation measurements at super-saturation.
All SOA produced in this work could be characterized as slightly hygroscopic. GF at 90% RH were between 1.03 and 1.15. For 0.31% SS the measured $D50$ varied between 96 and 113 nm. For easier comparison to findings in the literature we also present the hygroscopicity parameter κ from the one parameter representation of the Koehler equation proposed by *Petters and Kreidenweis* (2007). This approach assumes ideality, thus volume additivity, complete dissolution of the solute, and surface tension of water. The measured GF at 90% RH and CCN activity convert to κ(90%) between 0.013 and 0.079 and κ(CCN) = 0.037 - 0.224, respectively. This is in good agreement with HTDMA and CCN-C data reported for similar experiments in literature.
In an ideal case there should be closure between measurements in the sub- and super-saturated regime, i.e. it is assumed that the final value of κ is reached already at 90% RH and κ(90%) equals κ(CCN). Within the experiments κ(90%) was up to a factor of 3 lower than κ(CCN). Moreover, in several experiments opposite trends were observed for hygroscopic growth and CCN activation. This is not in agreement with the findings of *Rissler et al.* (submitted) who observed

a maximal overprediction of 34%.
Three possible reasons for the non-closure were investigated in this study: limited solubility, surface tension reduction, and concentration dependent non-ideality of the solution. If only a fraction of the solid particle is dissolved at 90% RH, κ is underestimated. Then the dissolved fraction may serve as a free parameter since the it is experimentally not assessible. Reducing the dissolved fraction to 27% - 82% of the dry particle volume led to the same values of κ(90%) as κ(CCN). For these calculations the surface tension of pure water was used. However, it is likely that the organic solutes are surface active. Therefore we can assume that κ(90%) is valid and vary the surface tension of the solutions until κ(CCN) matches κ(90%). Closure between HTDMA and CCN-C measurements was achieved with surface tension values between 0.039 and 0.067 N/m^2. Similar values between 0.03 and 0.072 N/m^2 can be found in literature.
To model the non-ideality of the solution in the droplets, κ was converted to the molal osmotic coefficient ϕ and RH to the water activity a_w assuming the average particle density (ρ_s) and average molecular mass (M_s) from AMS/SMPS and APCI-MS measurements. The parameter ϕ has an expectation value of 1 at infinite dilute solution. With the UNIFAC model a hypothetical organic molecule was determined for each measured growth curve whose functionality and corresponding $\phi(a_w)$ reproduced the observed hygroscopic growth. Additionally, real molecules, which can be thought of as surrogates for organics in SOA, were calculated with UNIFAC. The surrogates exhibited the same general functionality of $\phi(a_w)$ ($\kappa(RH)$, respectively) as the measured data with a distinct minimum between $a_w = 0.90 - 0.96$. Furthermore, the calculations reveal that the hygroscopicity is related to the degree of functionality and not generally to the O/C ratio in the molecule, i.e molecules with identical O/C ratio but different functional groups can exhibit a different hygroscopic growth.
All three explanations were equivalent in their ability to achieve closure between the data measured in the sub- and super-saturated regime. From the available data it could not be determined if one of them dominates or, more likely, if a combination of all three processes is responsible for the observations. The UNIFAC model has the advantage of being thermodynamically rigorous and already including concentration dependence. Moreover, the behavior in the sub-saturation regime is decoupled from the one in the super-saturated. Using the UNIFAC approach, the activation behavior predicted from the sub-saturated measurements depends only on the chosen $\frac{M_s}{\nu\rho_s}$ and σ. Assuming the surface tension of water and applying the measured range for M_s and ρ_s improves the prediction of the CCN activity compared to the single parameter (i.e. constant κ) approach. For a better understanding of the interplay of limited solubility, surface tension reduction, and the ratio $\frac{M_s}{\nu\rho_s}$, however, direct measurements of these quantities and their concentration dependence would be needed.

The detailed chemical composition of the gas-phase precursors had only little effect on both, hygroscopic growth and CCN activity. Changes within the group of MTs and SQTs were barely recognizable in the hygroscopic properties. Only if the precursors changed from MT to SQT dominated mixtures, κ decreased significantly.

In the SAPHIR chamber experiments the observed κ values were correlated to the ratio of produced OH and initial VOC concentration. With increasing exposure to OH the hygroscopicity increased. The higher OH/VOC level also explained the higher κ for low precursor concentrations. Although the absolute value of produced OH for the JPAC experiments cannot be compared to the experiments in SAPHIR due to the different reaction conditions, a similar correlation was observed: at constant OH production in the chamber the hygroscopicity increased with decreasing VOC concentration.

In the BMT experiments in SAPHIR the hygroscopic growth increased fast in the first 3 h of the experiments and leveled off afterwards. This was due to semi-volatile products leaving the particles and higher oxidized compounds condensing on the particles. This initial aging was strongly connected to the OH production. The evolution of the CCN activity depended on whether σ_s, M_s or ρ_s changed significantly with time. The density increased in the same way in all experiments. This should increase CCN activity if σ_s and M_s are constant. For cases where decreasing CCN activity was observed, either M_s must have increased more strongly than ρ_s or the compounds became less surface active with time. For example: the formation of oligomers in the particles will easily increase M_s. Organic compounds are surface active if they consist of a hydrophilic (oxidized functional groups) and a hydrophobic part (hydrocarbon backbone). If the hydrocarbon backbone is oxidized with time, i.e. becomes more hydrophilic, the molecules would lose their amphiphilic character. Thus, their impact on the surface tension of the solution would be reduced.

It is important to bridge the gap between sub- and super-saturated measurements to further understand the processes involved in hygroscopic growth and CCN activation of SOA particles. To estimate the contribution of SOA particles to the microphysical properties of all aerosol particles in global models, it is sufficient to use an average κ of 0.10 ± 0.02 for these compounds.

Bibliography

Ackerman, A. S., O. B. Toon, J. P. Taylor, D. W. Johnson, P. V. Hobbs, and R. J. Ferek (2000), Effects of aerosols on cloud albedo: Evaluation of Twomey's parameterization of cloud susceptibility using measurements of ship tracks, *Journal of the Atmospheric Sciences*, *57*(16), 2684–2695.

Albrecht, B. A. (1989), Aerosols, cloud microphysics, and fractional cloudiness, *Science*, *245*(4923), 1227–1230.

Asa-Awuku, A., A. Nenes, S. Gao, R. C. Flagan, and J. H. Seinfeld (2010), Water-soluble SOA from alkene ozonolysis: composition and droplet activation kinetics inferences from analysis of CCN activity, *Atmospheric Chemistry and Physics*, *10*(4), 1585–1597.

Bares, R. (2003), Untersuchung zur Ozonolyse einfacher Alkene in der Atmosphären-simulationskammer SAPHIR, *Tech. rep.*, Forschungszentrum Jülich.

Buchholz, A. (2007), Entwicklung eines Geräts zur Untersuchung des hygroskopischen Wachstums von organischen Aerosolen, Diplomarbeit, University of Cologne.

DeMore, W. B., S. P. Sander, D. M. Golden, C. E. Kolb, R. F. Hampson, M. J. Kurylo, C. J. Howard, A. R. Ravishankara, and M. J. Molina (1997), *Chemical Kinetics and Photochemical Data for Use in Stratospheric Modeling*, Jet Propulsion Laboratories.

Dinar, E., I. Taraniuk, E. R. Graber, S. Katsman, T. Moise, T. Anttila, T. F. Mentel, and Y. Rudich (2006), Cloud condensation nuclei properties of model and atmospheric HULIS, *Atmospheric Chemistry and Physics*, *6*(9), 2465–2482.

Duplissy, J., M. Gysel, M. R. Alfarra, J. Dommen, A. Metzger, A. S. H. Prevot, E. Weingartner, A. Laaksonen, T. Raatikainen, N. Good, S. F. Turner, G. McFiggans, and U. Baltensperger (2008), Cloud forming potential of secondary organic aerosol under near atmospheric conditions, *Geophysical Research Letters*, *35*(3).

Engelhardt, G., A. Asa-Awuku, A. Nenes, and S. Pandis (2008), CCN activation and droplet growth kinetics of fresh and aged monoterpene secondary organic aerosol, *Atmospheric Chemistry and Physics*, *8*, 3937–3949.

Facchini, M. C., S. Decesari, M. Mircea, S. Fuzzi, and G. Loglio (2000), Surface tension of atmospheric wet aerosol and cloud/fog droplets in relation to their

organic carbon content and chemical composition, *Atmospheric Environment*, *34*(28), 4853–4857.

Finlayson-Pitts, B., and J. Pitts (2000), *Chemistry of the upper and lower atmosphere*, Academic Press, San Diego.

Forster, P., V. Ramaswamy, P. Artaxo, T. Berntsen, R. Betts, D. Fahey, J. Haywood, J. Lean, D. Lowe, G. Myhre, J. Nganga, R. Prinn, G. Raga, M. Schulz, and R. V. Dorland (2007), *Changes in Atmospheric Constituents and in Radiative Forcing. In: Climate Change 2007: The Physical Science Basis. Contribution of Working Group I to the Fourth Assessment Report of the Intergovernmental Panel on Climate Change*, Cambridge University Press, Cambridge, United Kingdom and New York, NY, USA.

Fredenslund, A., J. Gmehling, M. L. Michelsen, P. Rasmussen, and J. M. Prausnitz (1977), Computerized design of multicomponent distillation-columns using UNIFAC group contribution method for calculation of activity-coefficients, *Industrial and Engineering Chemistry Process Design and Development*, *16*(4), 450–462.

Goldstein, A. H., and I. E. Galbally (2007), Known and unexplored organic constituents in the earth's atmosphere, *Environmental Science and Technology*, *41*(5), 1514–1521.

Guenther, A., C. N. Hewitt, D. Erickson, R. Fall, C. Geron, T. Graedel, P. Harley, L. Klinger, M. Lerdau, W. A. McKay, T. Pierce, B. Scholes, R. Steinbrecher, R. Tallamraju, J. Taylor, and P. Zimmerman (1995), A global-model of natural volatile organic-compound emissions, *Journal of Geophysical Research-Atmospheres*, *100*(D5), 8873–8892.

Gunn, R., and R. H. Woessner (1956), Measurements of the systematic electrification of aerosols, *Journal of Colloid Science*, *11*(3), 254–259.

Hallquist, M., J. C. Wenger, U. Baltensperger, Y. Rudich, D. Simpson, M. Claeys, J. Dommen, N. M. Donahue, C. George, A. H. Goldstein, J. F. Hamilton, H. Herrmann, T. Hoffmann, Y. Iinuma, M. Jang, M. E. Jenkin, J. L. Jimenez, A. Kiendler-Scharr, W. Maenhaut, G. McFiggans, T. F. Mentel, A. Monod, A. S. H. Prevot, J. H. Seinfeld, J. D. Surratt, R. Szmigielski, and J. Wildt (2009), The formation, properties and impact of secondary organic aerosol: current and emerging issues, *Atmospheric Chemistry and Physics*, *9*(14), 5155–5236.

Heald, C. L., D. J. Jacob, R. J. Park, L. M. Russell, B. J. Huebert, J. H. Seinfeld, H. Liao, and R. J. Weber (2005), A large organic aerosol source in the free troposphere missing from current models, *Geophysical Research Letters*, *32*(18).

Hofzumahaus, A., T. Brauers, U. Platt, and J. Callies (1992), Latitudinal variation of measured O_3 photolysis frequencies j(O^1D) and primary OH productionrates over the atlantic-ocean between 50° N and 30° S, *Journal of Atmospheric Chemistry*, *15*(3-4), 283–298.

Hyland, R., and A. Wexler (1983), Formulation for the thermodynamic properties of dry air (from 173.15 K to 473.15 K) and of saturated moist air (from 173.15 K to 372.15 K), at pressures to 5 MPa, *Ashrae Journal-American Society of Heating Refrigerating and Air-Conditioning Engineers*, *25*(5), 64–64.

Jayne, J. T., D. C. Leard, X. F. Zhang, P. Davidovitis, K. A. Smith, C. E. Kolb, and D. R. Worsnop (2000), Developement of an aerosol mass spectrometer for size and compositiob analysis of submicron particles, *Aerosol Science and Technology*, *33*, 49–70.

Juranyi, Z., M. Gysel, J. Duplissy, E. Weingartner, T. Tritscher, J. Dommen, S. Henning, M. Ziese, A. Kiselev, F. Stratmann, I. George, and U. Baltensberger (2009), Influence of gas-to-particle conversion on the hygroscopic and droplet activation behaviour of α-pinene secondary organic arerosol, *Physical Chemistry Chemical Physics*, *11*, 8091–8097.

Kalberer, M., D. Paulsen, M. Sax, M. Steinbacher, J. Dommen, A. S. H. Prevot, R. Fisseha, E. Weingartner, V. Frankevich, R. Zenobi, and U. Baltensperger (2004), Identification of polymers as major components of atmospheric organic aerosols, *Science*, *303*(5664), 1659–1662.

Kanakidou, M., J. H. Seinfeld, S. N. Pandis, I. Barnes, F. J. Dentener, M. C. Facchini, R. Van Dingenen, B. Ervens, A. Nenes, C. J. Nielsen, E. Swietlicki, J. P. Putaud, Y. Balkanski, S. Fuzzi, J. Horth, G. K. Moortgat, R. Winterhalter, C. E. L. Myhre, K. Tsigaridis, E. Vignati, E. G. Stephanou, and J. Wilson (2005), Organic aerosol and global climate modelling: a review, *Atmospheric Chemistry and Physics*, *5*, 1053–1123.

Köhler, H. (1936), The nucleus in and the growth of hygroscopic droplets, *Transactions of the Faraday Society*, *32*(2), 1152–1161.

Larsen, D., D. di Bella, M. Glasius, R. Winterhalter, N. Jensen, and J. Hjorth (2001), Gas phase OH oxidation of monoterpenes: Gasous and particulate products, *Journal of Atmosperic Chemistry*, *38*, 231–276.

Mentel, T. F., J. Wildt, A. Kiendler-Scharr, E. Kleist, R. Tillmann, M. Dal Maso, R. Fisseha, T. Hohaus, H. Spahn, R. Uerlings, R. Wegener, P. T. Griffiths, E. Dinar, Y. Rudich, and A. Wahner (2009), Photochemical production of aerosols from real plant emissions, *Atmospheric Chemistry and Physics*, *9*(13), 4387–4406.

Mueller, L., M.-C. Reinnig, H. Hayen, and T. Hoffmann (2009), Characterization of oligomeric compounds in secondary organic aerosol using liquid chromatography coupled to electrospray ionization fourier transform ion cyclotron resonance mass spectrometry, *Rapid Communications in Mass Spectrometry*, *23*(7), 971–979.

Padro, L. T., A. Asa-Awuku, R. Morrison, and A. Nenes (2007), Inferring thermodynamic properties from CCN activation experiments: single-component and binary aerosols, *Atmospheric Chemistry and Physics*, *7*, 5263–5274.

Petters, M. D., and S. M. Kreidenweis (2007), A single parameter representation of hygroscopic growth and cloud condensation nucleus activity, *Atmospheric Chemistry and Physics*, *7*(8), 1961–1971.

Pincus, R., and M. B. Baker (1994), Effect of precipitation on the albedo susceptibility of clouds in the marine boundary-layer, *Nature*, *372*(6503), 250–252.

Poling, B. E., J. M. Prausnitz, and J. O'Connell (2000), Fluid phase equilibria in mulitcomponent systems, in *The properties of gases and liquids*, 5th ed., McGraw-Hill, New York.

Prisle, N. L., T. Raatikainen, R. Sorjamaa, B. Svenningsson, A. Laaksonen, and M. Bilde (2008), Surfactant partitioning in cloud droplet activation: a study of C_8, C_{10}, C_{12} and C_{14} normal fatty acid sodium salts, *Tellus Series B-Chemical and Physical Meteorology*, *60*(3), 416–431.

Reinnig, C. (2009), Massenspektrometrische Untersuchungen und Nachweis von organischen Peroxiden und höhermolekularen Verbindungen im biogenen sekundären organischen Aerosol, Ph.D. thesis, Johannes Gutenberg-Universität.

Rissler, J., B. Svenningsson, E. Fors, M. Bilde, and E. Swietlicki (submitted), An evaluation and comparison of CCN activity models - predicting particle critical saturation from growth at sub saturation, *Journal of Geophysical Research*.

Roberts, G. C., and A. Nenes (2005), A continuous-flow streamwise thermal-gradient CCN chamber for atmospheric measurements, *Aerosol Science and Technology*, *39*(3), 206–221.

Rose, D., S. S. Gunthe, E. Mikhailov, G. P. Frank, U. Dusek, M. O. Andreae, and U. Poschl (2008), Calibration and measurement uncertainties of a continuous-flow cloud condensation nuclei counter (DMT-CCNC): CCN activation of ammonium sulfate and sodium chloride aerosol particles in theory and experiment, *Atmospheric Chemistry and Physics*, *8*(5), 1153–1179.

Spindler, C. (2010), Charakterisierung Biogener Sekundärer Organischer Aerosole mit statistischen Methoden, Ph.D. thesis, Bergische Universität Wuppertal.

Strathmann, L. (2009), Entwicklung und Charakterisierung eines kompakten Wolkenkeimspektrometers, Diplomarbeit, Fachhochschule Aachen.

Twomey, S. (1974), Pollution and planetary albedo, *Atmospheric Environment*, *8*(12), 1251–1256.

Wex, H., T. Hennig, I. Salma, R. Ocskay, A. Kiselev, S. Henning, A. Massling, A. Wiedensohler, and F. Stratmann (2007), Hygroscopic growth and measured and modeled critical super-saturations of an atmospheric HULIS sample, *Geophysical Research Letters*, *34*(2), 5.

Wex, H., M. D. Petters, C. M. Carrico, E. Hallbauer, A. Massling, G. R. McMeeking, L. Poulain, Z. Wu, S. M. Kreidenweis, and F. Stratmann (2009), Towards

closing the gap between hygroscopic growth and activation for secondary organic aerosols: Part 1 - evidence from measurements, *Atmospheric Chemistry and Physics*, *9*, 3987–3997.

Whitby, K., and G. Sverdrup (1980), California aerosols: Their physical and chemical characteristics, *Advances in Environment Science and Technology*, *8*, 477–525.

Wiedensohler, A. (1988), An approximation of the bipolar charge-distribution for particles in the sub-micron size range, *Journal of Aerosol Science*, *19*(3), 387–389.

Wittig, R., J. Lohmann, and J. Gmehling (2003), Vapor-liquid equilibria by UNIFAC group contribution: 6th Revision and extension, *Industrial & Engineering Chemistry Research*, *42*(1), 183–188.

Zhang, Q., J. L. Jimenez, M. R. Canagaratna, J. D. Allan, H. Coe, I. Ulbrich, M. R. Alfarra, A. Takami, A. M. Middlebrook, Y. L. Sun, K. Dzepina, E. Dunlea, K. Docherty, P. F. DeCarlo, D. Salcedo, T. Onasch, J. T. Jayne, T. Miyoshi, A. Shimono, S. Hatakeyama, N. Takegawa, Y. Kondo, J. Schneider, F. Drewnick, S. Borrmann, S. Weimer, K. Demerjian, P. Williams, K. Bower, R. Bahreini, L. Cottrell, R. J. Griffin, J. Rautiainen, J. Y. Sun, Y. M. Zhang, and D. R. Worsnop (2007), Ubiquity and dominance of oxygenated species in organic aerosols in anthropogenically-influenced northern hemisphere midlatitudes, *Geophysical Research Letters*, *34*(13).

Ziese, M., H. Wex, E. Nilsson, I. Salma, R. Ocskay, T. Hennig, A. Massling, and F. Stratmann (2008), Hygroscopic growth and activation of HULIS particles: experimental data and a new iterative parameterization scheme for complex aerosol particles, *Atmospheric Chemistry and Physics*, *8*(6), 1855–1866.

A. Recorded CCN-C and HTDMA data

In the following all data measured with the CCN-C and HTDMA is presented.

A.1 CCN-C data

The CCN-C data is shown as SS_{crit} vs. $D50$ with time since experiment start as color code. For all SAPHIR experiments this is the addition of ozone (for type A almost at the same time the camber roof was opened). For all JPAC experiments this is the time when the UV lamp was turned on (i.e. the start of the photochemistry). Data measured with the single-size selection mode are indicated with red circles. All other data was measured using the polydisperse or size-scanning method.
The CCN-C data was fitted with equation 2.29. The dark blue line is a "free" fit and the light blue line is calculated with a fixed exponent of -1.5. The coefficients for this fixed fit are shown in the graph.
The $D50$ and SS_{crit} values calculated from HTDMA measurements in the same experiment are shown as black triangles (see section 5.1 for details).

A.1.1 BMT- and α-pinene experiments in SAPHIR

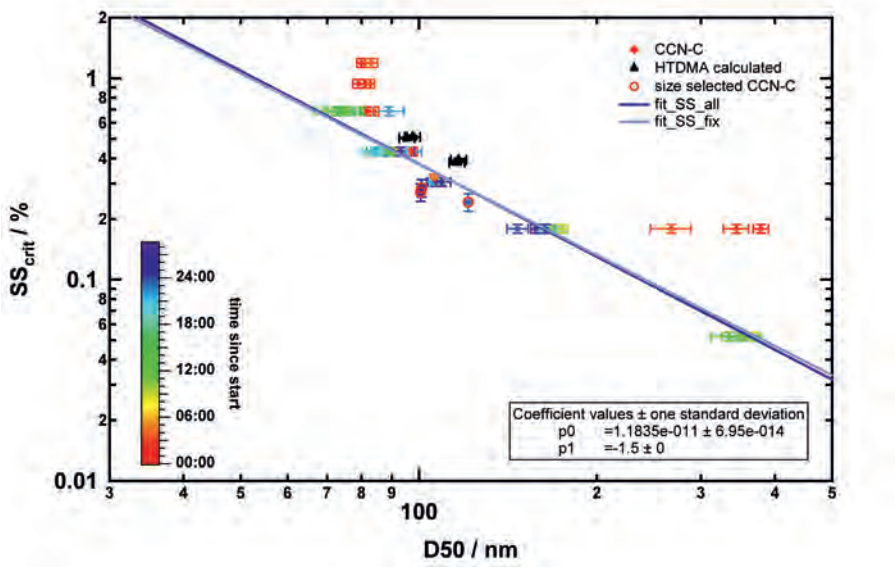

Figure A.1: *Measured SS_{crit}/D50 pairs for experiment 1: SAPHIR, 500 ppbC BMT, type A, b/c.*

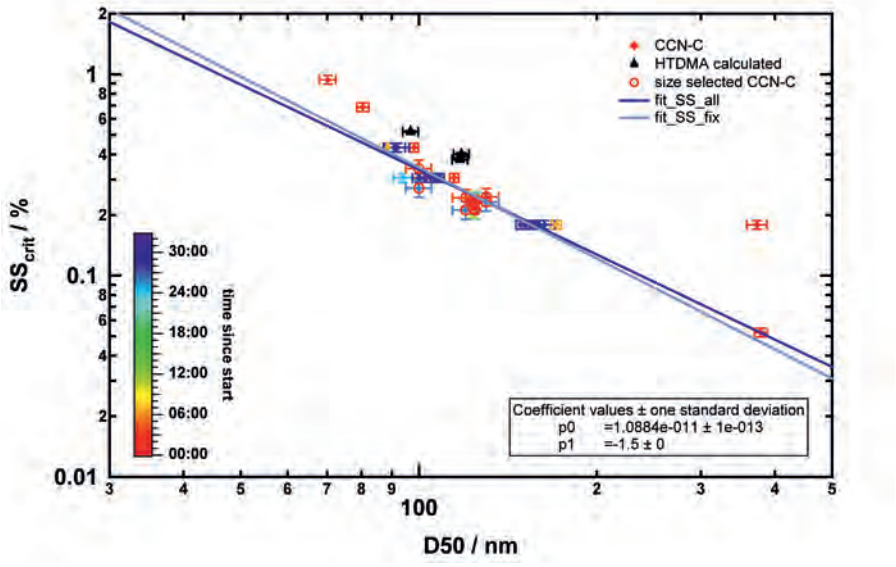

Figure A.2: *Measured SS_{crit}/D50 pairs for experiment 2: SAPHIR, 500 ppbC BMT without ocimene, type A, b/c.*

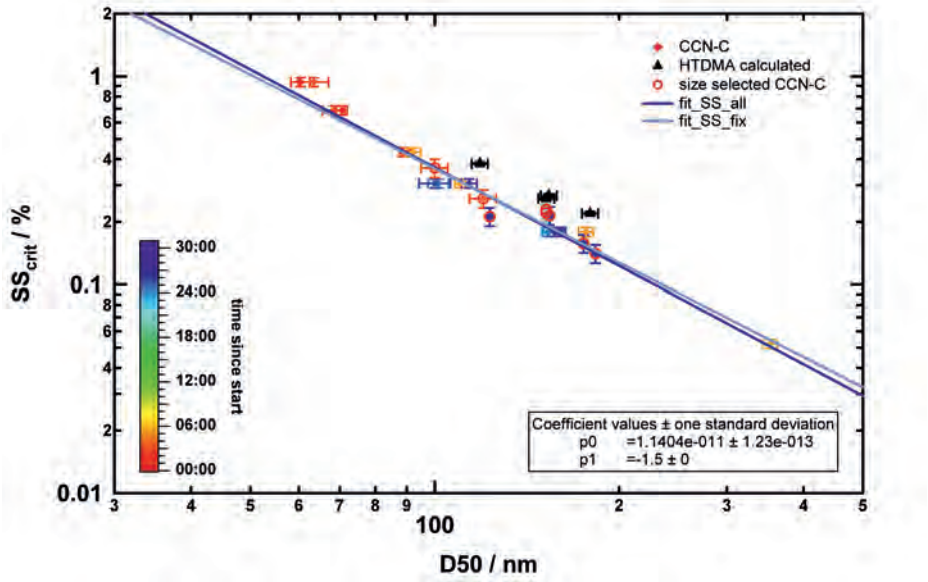

Figure A.3: *Measured SS_{crit}/D50 pairs for experiment 3: SAPHIR, 1000 ppbC BMT, type A, b/b.*

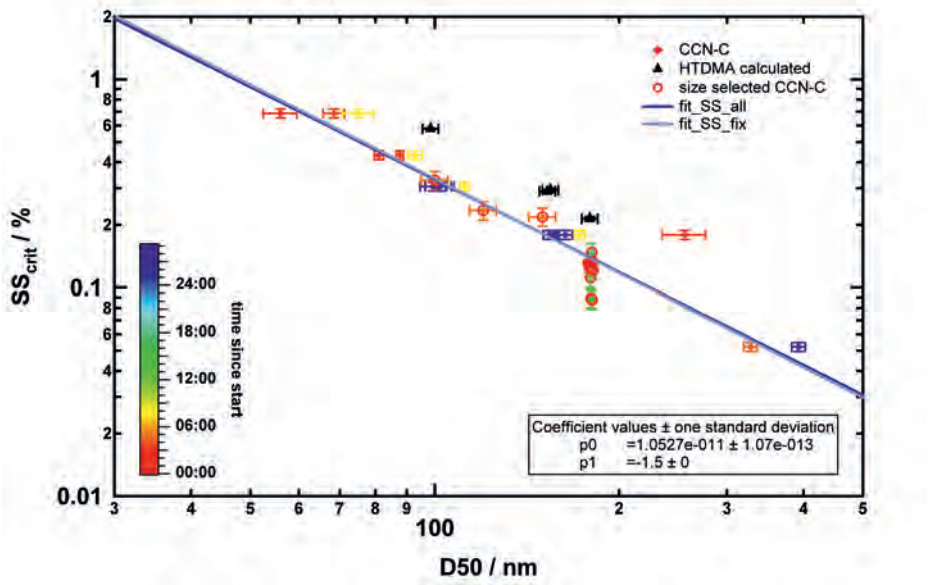

Figure A.4: *Measured SS_{crit}/D50 pairs for experiment 4: SAPHIR, 500 ppbC BMT + 45 ppbC SQT, type A, c/c.*

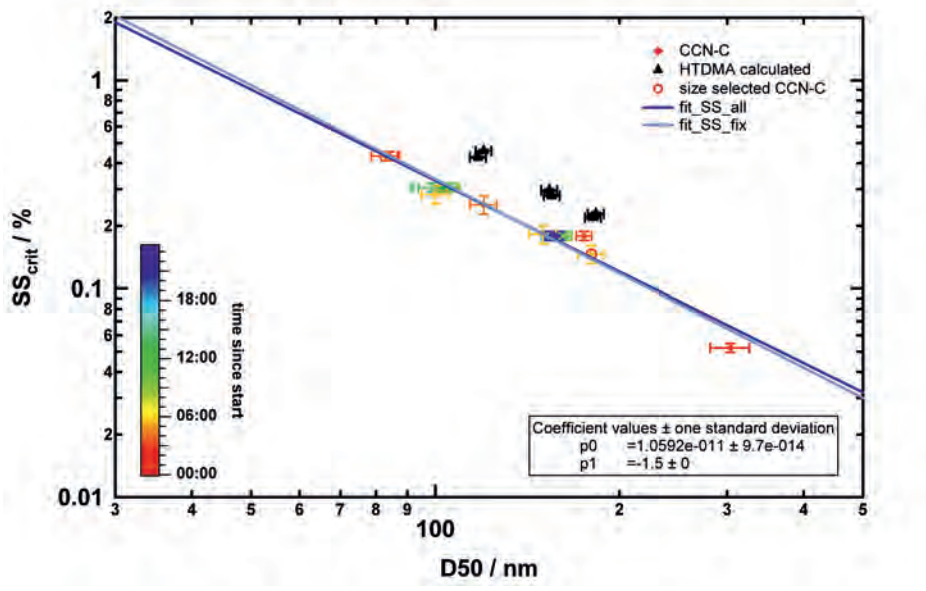

Figure A.5: *Measured SS_{crit}/D50 pairs for experiment5: SAPHIR, 1000 ppbC BMT, type A, c/c.*

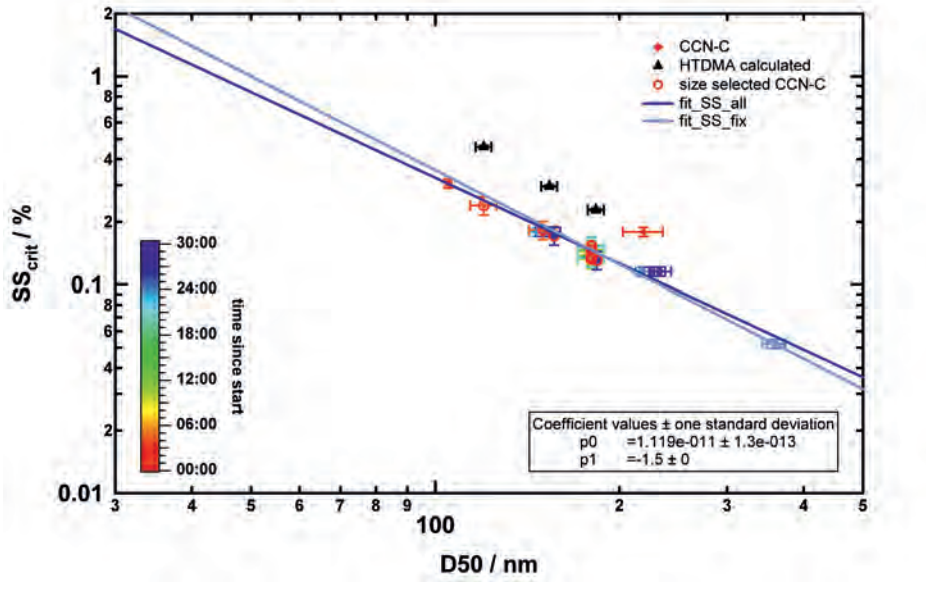

Figure A.6: *Measured SS_{crit}/D50 pairs for experiment 6: SAPHIR, 1000 ppbC BMT without ocimene, type A, c/b.*

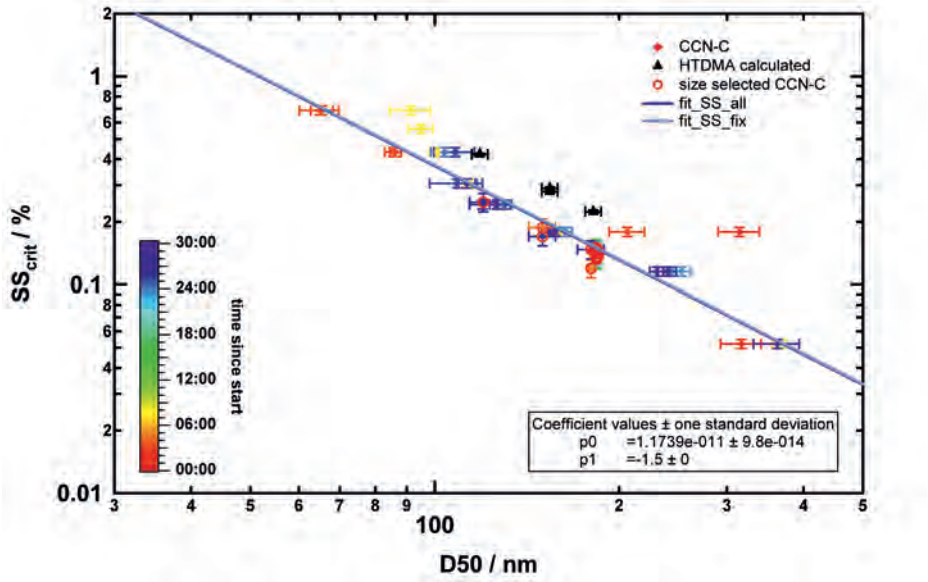

Figure A.7: *Measured SS_{crit}/D50 pairs for experiment 7: SAPHIR, 1000 ppbC BMT + 45 ppbC SQT, type A, b/b.*

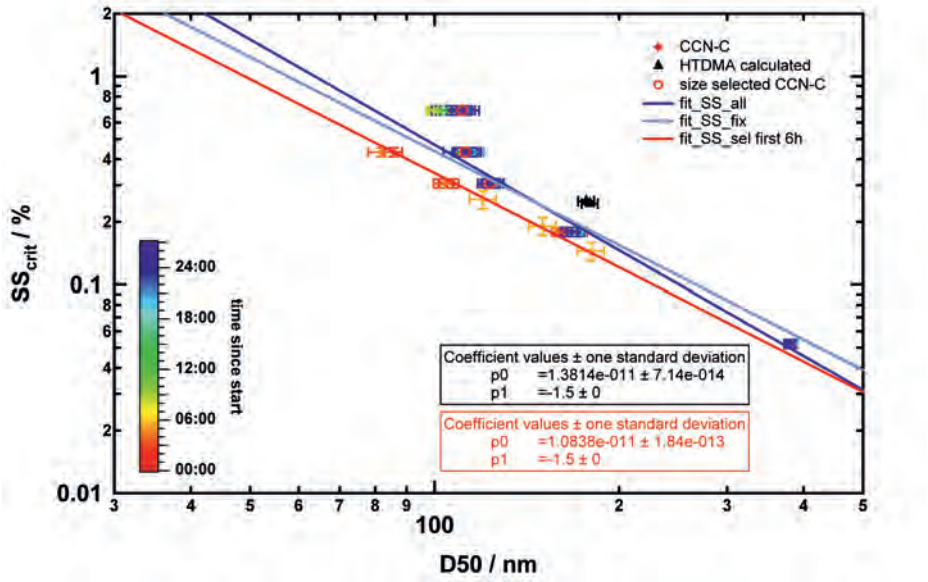

Figure A.8: *Measured SS_{crit}/D50 pairs for experiment 8: SAPHIR, 1000 ppbC BMT, 200 ppb O_3, type B*, dark. Red line is a fit with fixed exponent to the data of the first 6h.*

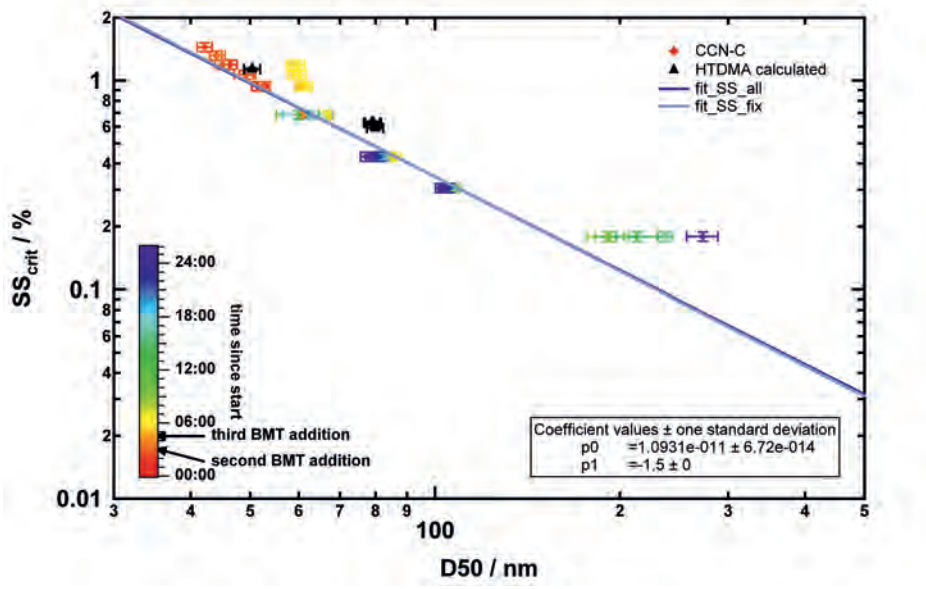

Figure A.9: *Measured SS_{crit}/D50 pairs for experiment 11: SAPHIR, 3x40 ppbC BMT, type A, b/b.*

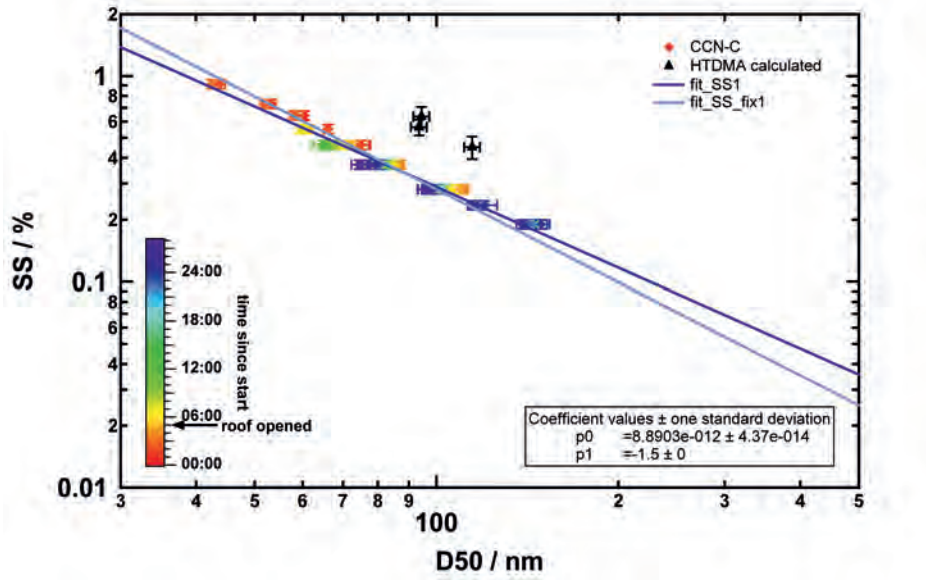

Figure A.10: *Measured SS_{crit}/D50 pairs for experiment 20: SAPHIR, 100 ppbC α-pinene, type B, b/dark.*

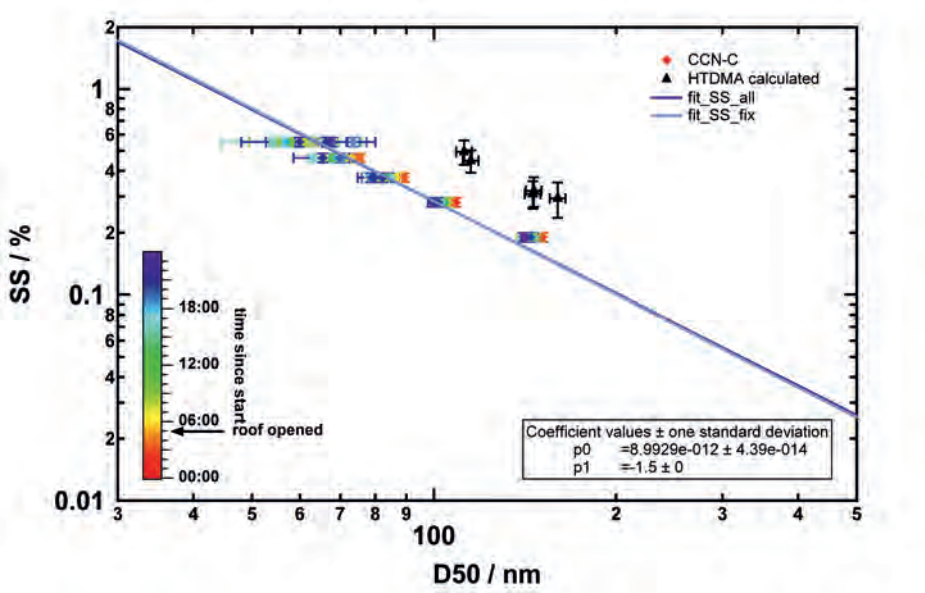

Figure A.11: *Measured SS_{crit}/D50 pairs for experiment 21: SAPHIR, 400 ppbC α-pinene, type B, b/b.*

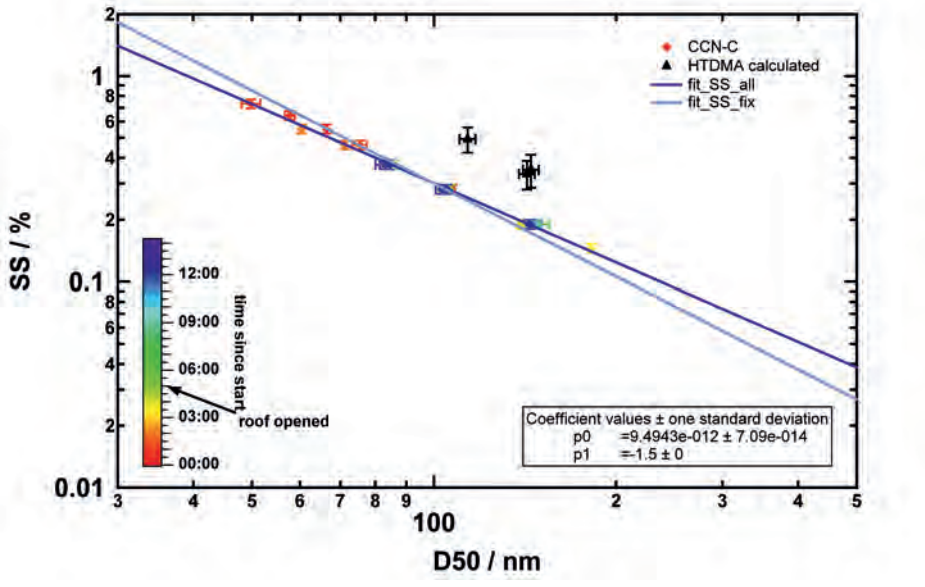

Figure A.12: *Measured SS_{crit}/D50 pairs for experiment 22: SAPHIR, 400 ppbC α-pinene + 300 ppm CO, type B, b/b.*

A.1.2 JPAC experiments

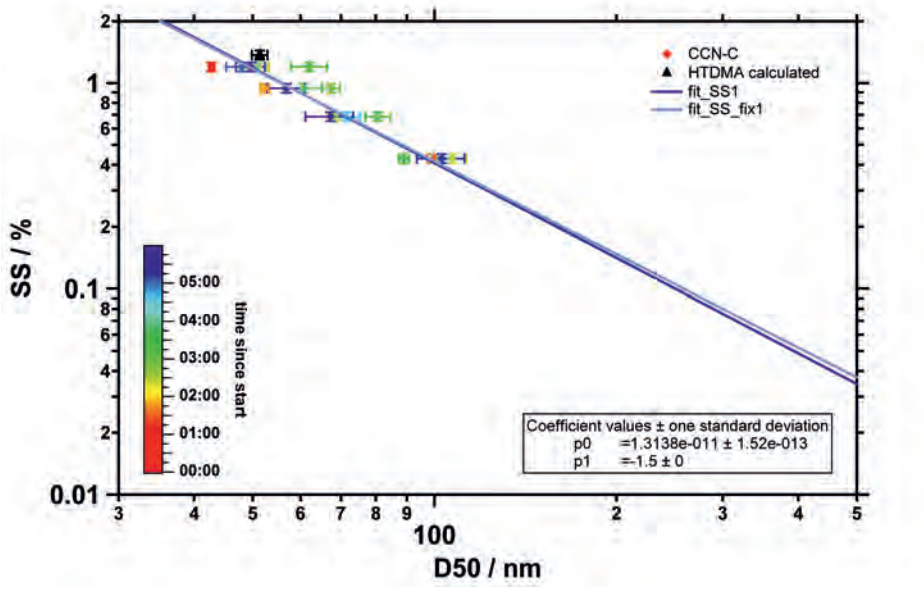

Figure A.13: *Measured SS_{crit}/D50 pairs for experiment 15_1: JPAC, PC 15° C.*

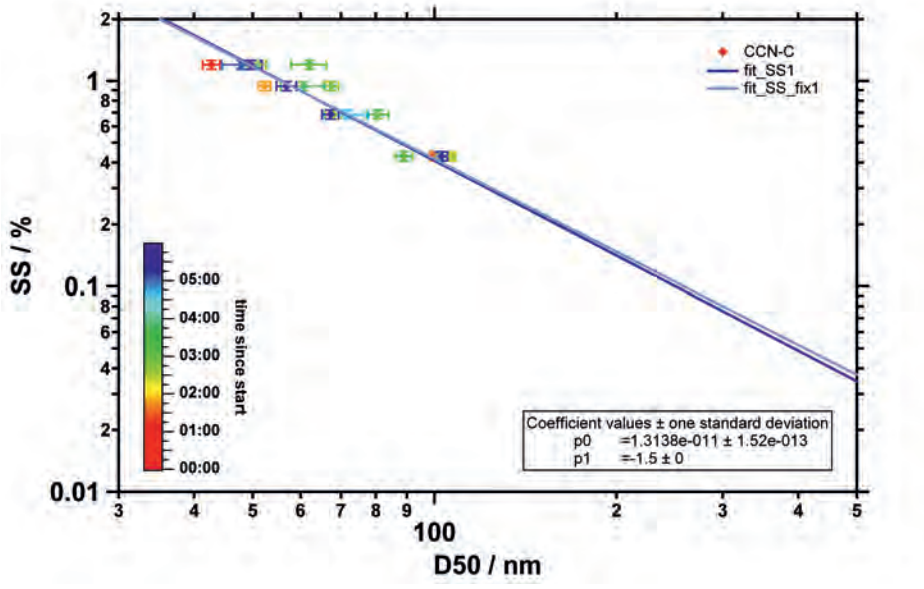

Figure A.14: *Measured SS_{crit}/D50 pairs for experiment 15_2: JPAC, PC 15° C.*

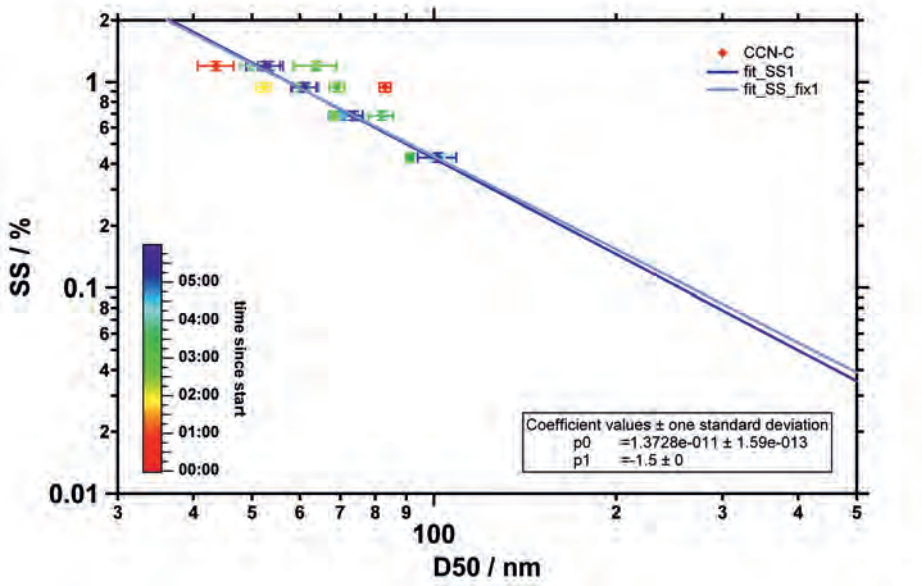

Figure A.15: *Measured SS_{crit}/D50 pairs for experiment 15_3: JPAC, PC 15° C.*

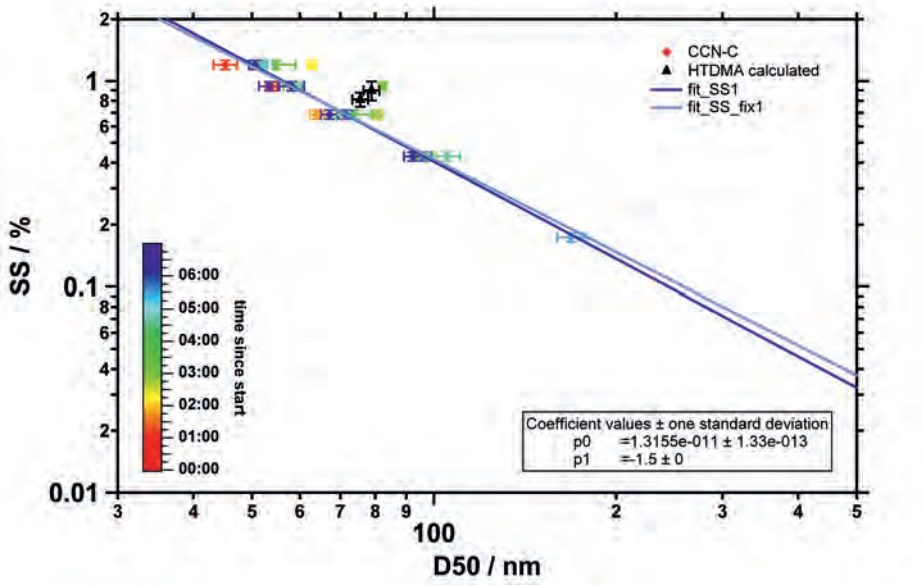

Figure A.16: *Measured SS_{crit}/D50 pairs for experiment 15_4: JPAC, PC 15° C.*

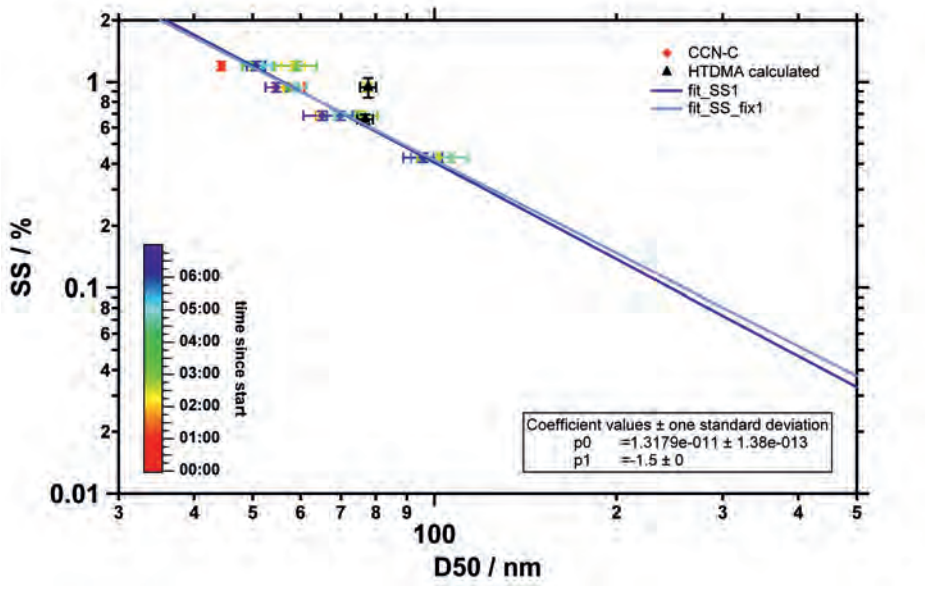

Figure A.17: *Measured SS_{crit}/D50 pairs for experiment 15_5: JPAC, PC 15° C.*

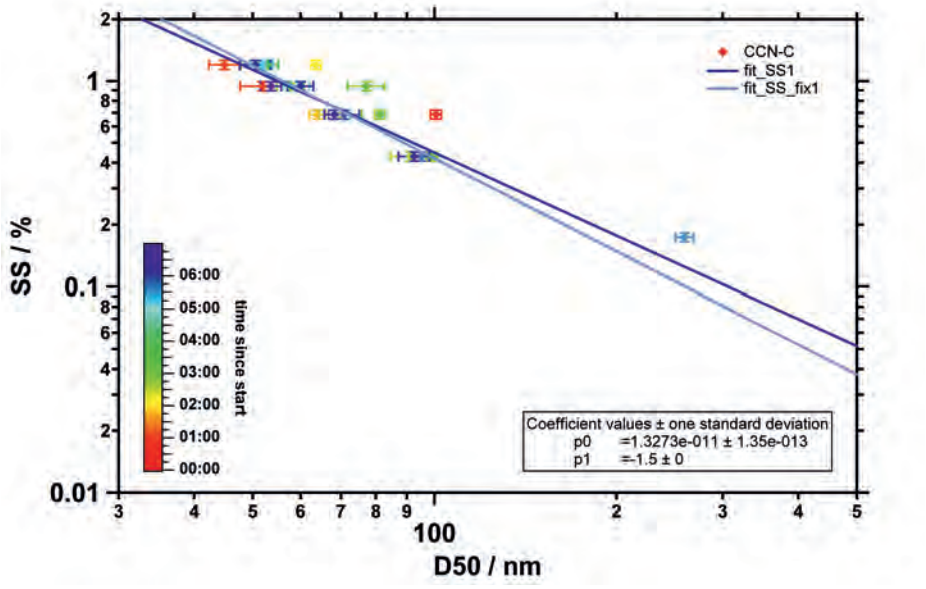

Figure A.18: *Measured SS_{crit}/D50 pairs for experiment 15_6: JPAC, PC 15° C.*

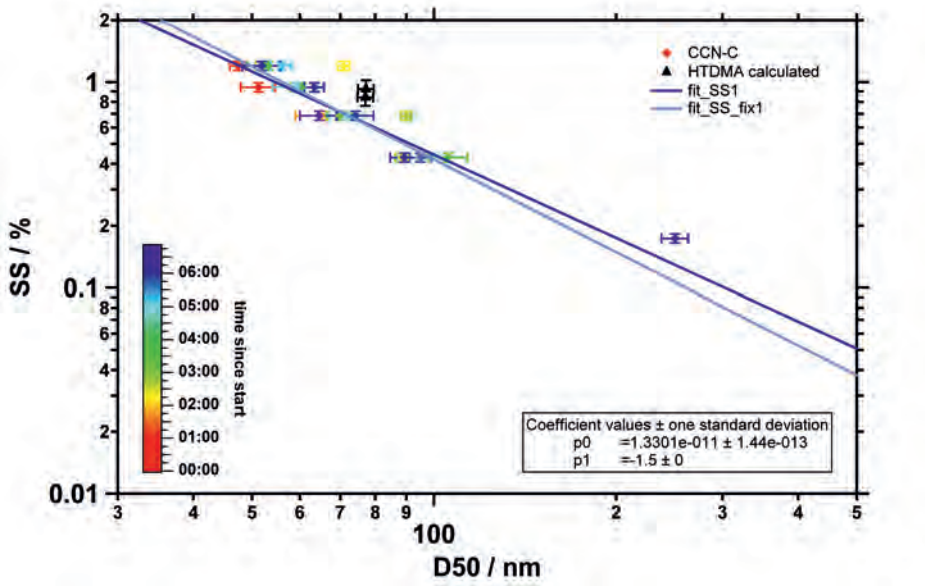

Figure A.19: *Measured $SS_{crit}/D50$ pairs for experiment 15_7: JPAC, PC 15° C.*

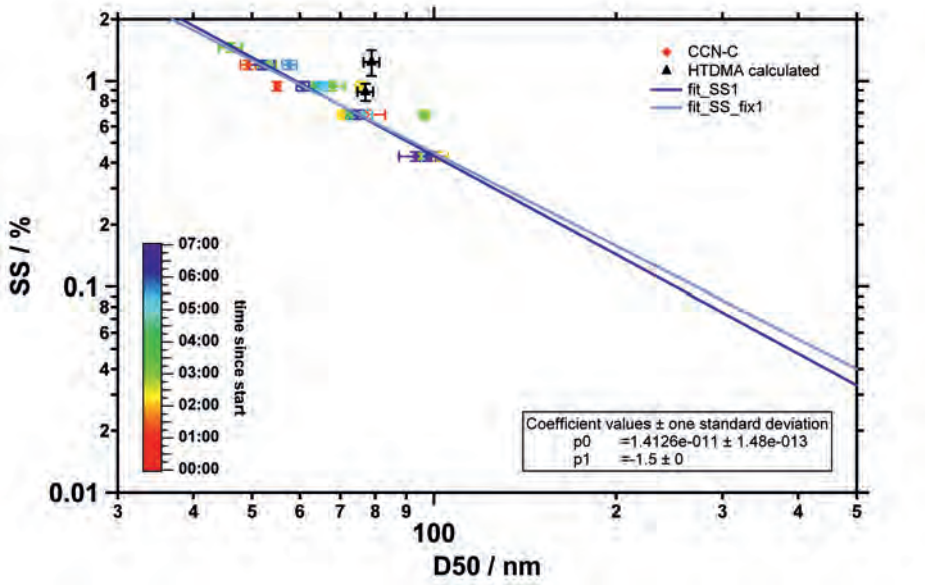

Figure A.20: *Measured $SS_{crit}/D50$ pairs for experiment 20_1: JPAC, PC 20° C.*

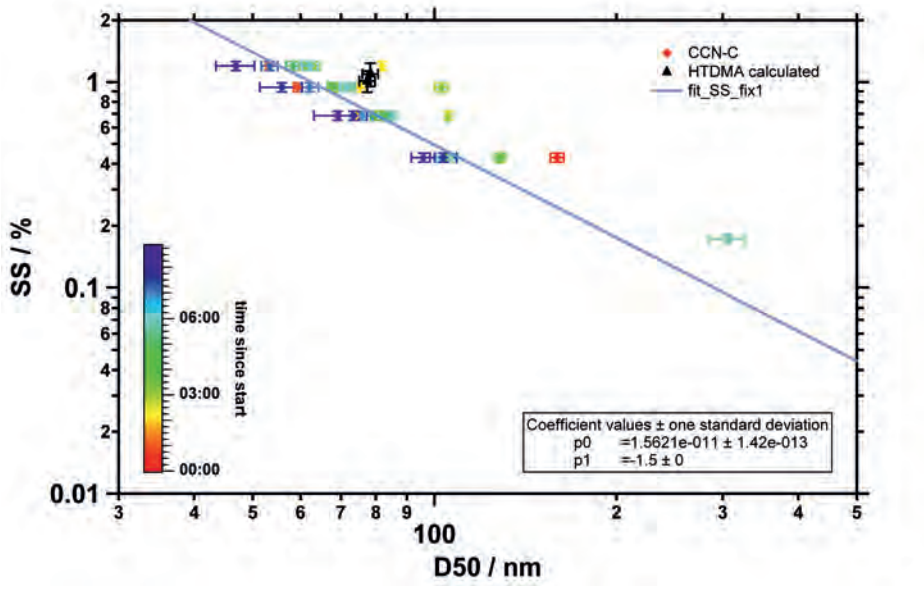

Figure A.21: *Measured SS_{crit}/D50 pairs for experiment 20_2: JPAC, PC 20° C.*

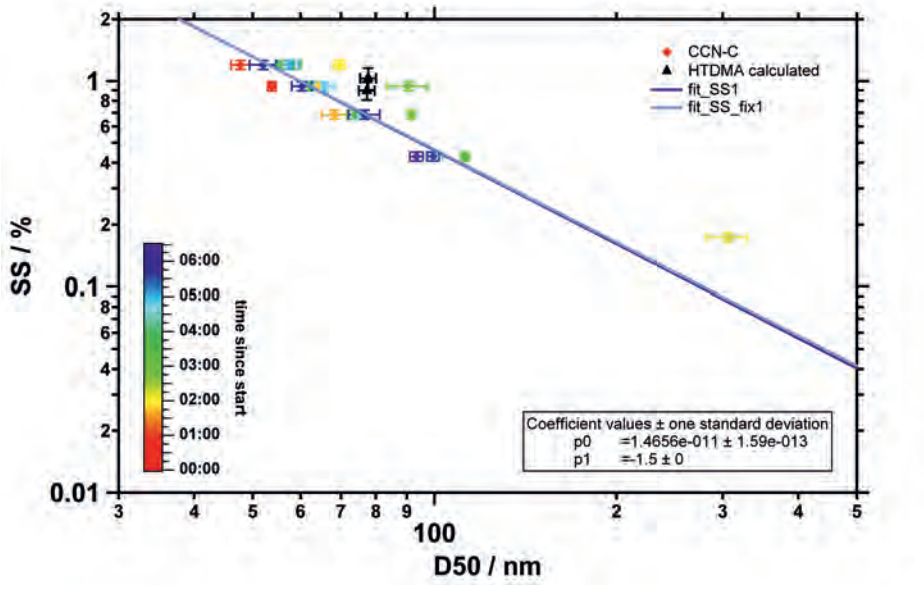

Figure A.22: *Measured SS_{crit}/D50 pairs for experiment 20_3: JPAC, PC 20° C.*

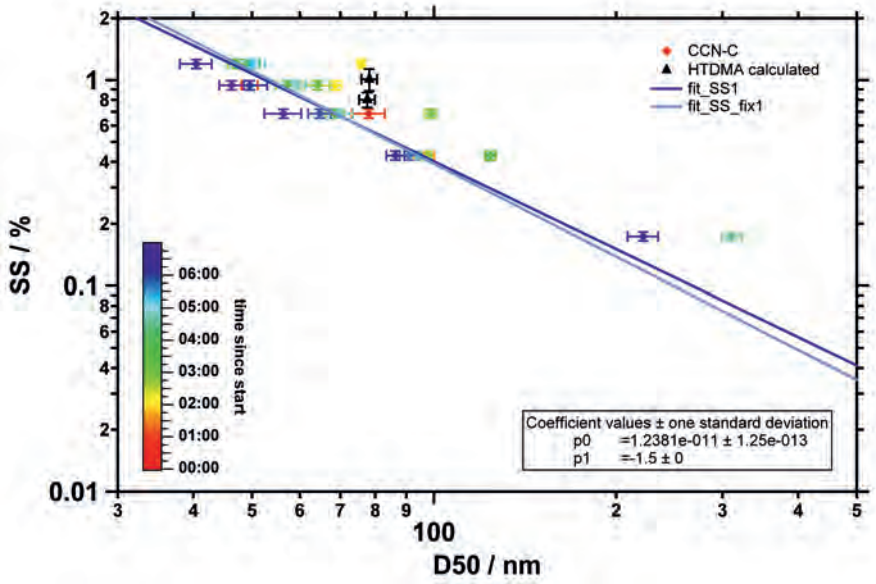

Figure A.23: *Measured $SS_{crit}/D50$ pairs for experiment 20_4: JPAC, PC 20° C.*

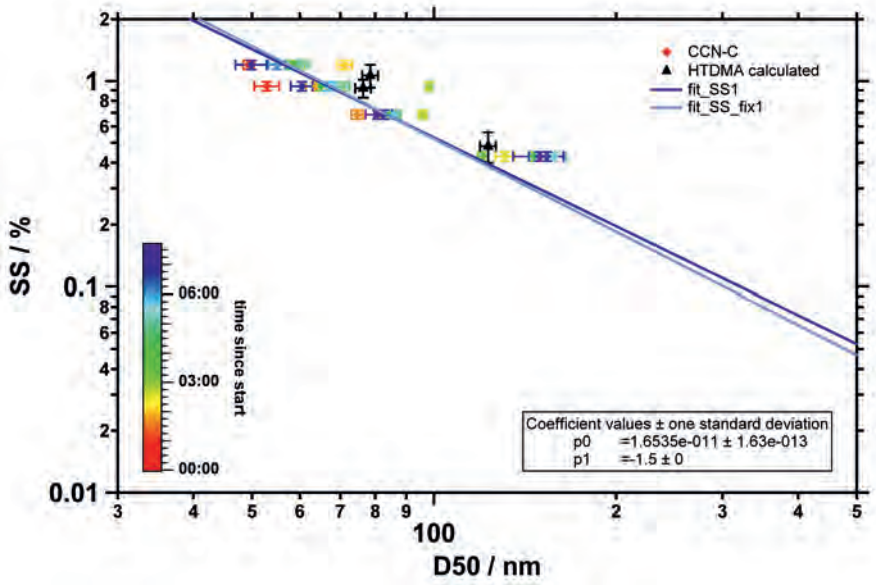

Figure A.24: *Measured $SS_{crit}/D50$ pairs for experiment 25_1: JPAC, PC 25° C.*

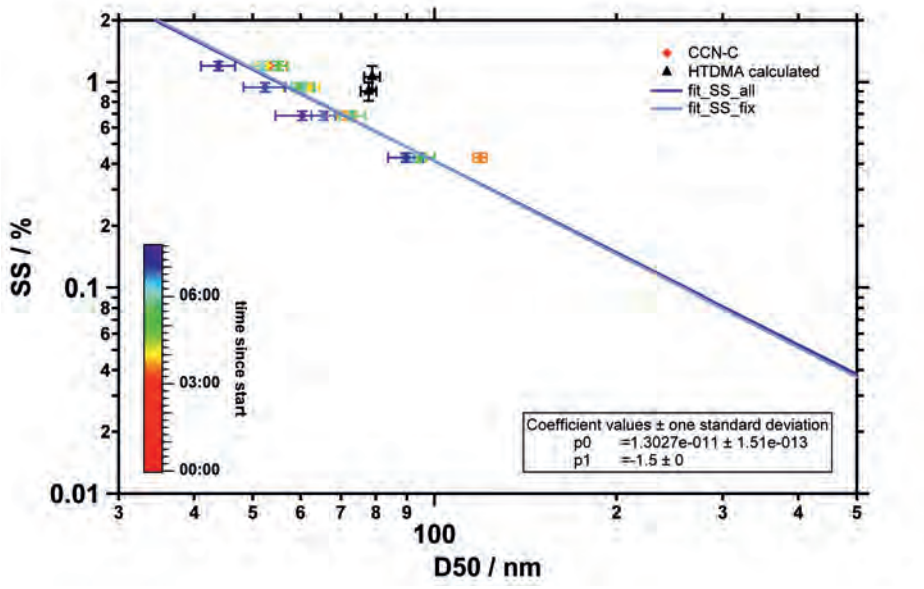

Figure A.25: *Measured $SS_{crit}/D50$ pairs for experiment 25_2: JPAC, PC 25° C.*

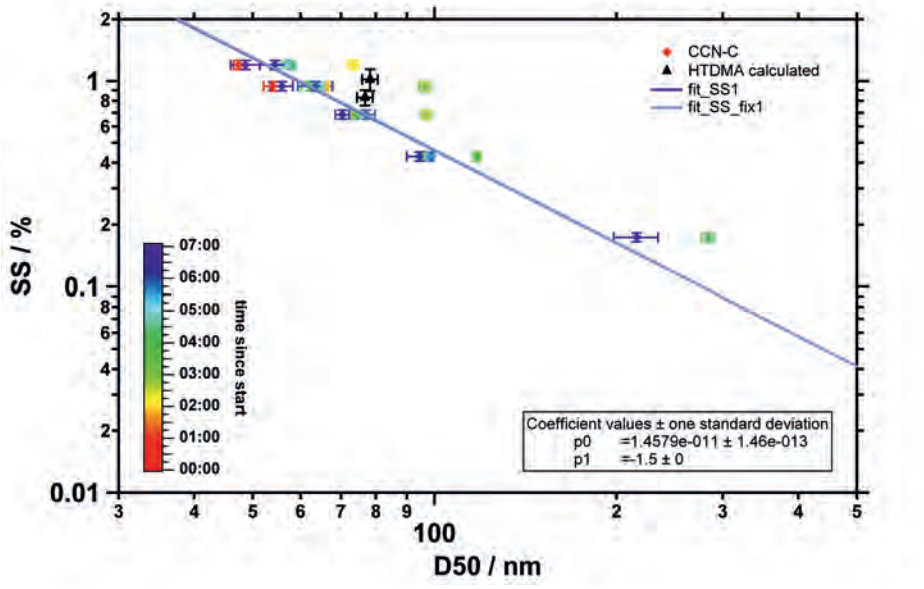

Figure A.26: *Measured $SS_{crit}/D50$ pairs for experiment 25_3: JPAC, PC 25° C.*

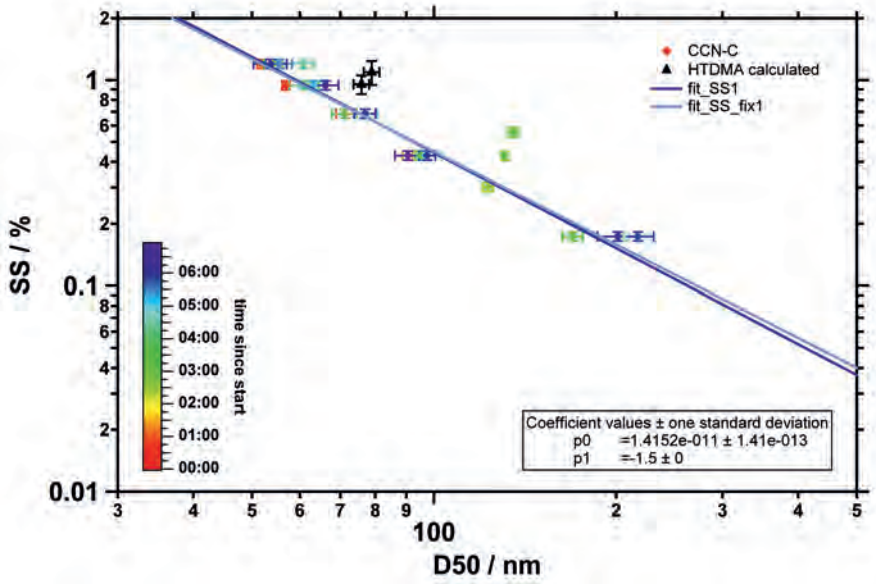

Figure A.27: *Measured $SS_{crit}/D50$ pairs for experiment 30_1: JPAC, PC 30° C.*

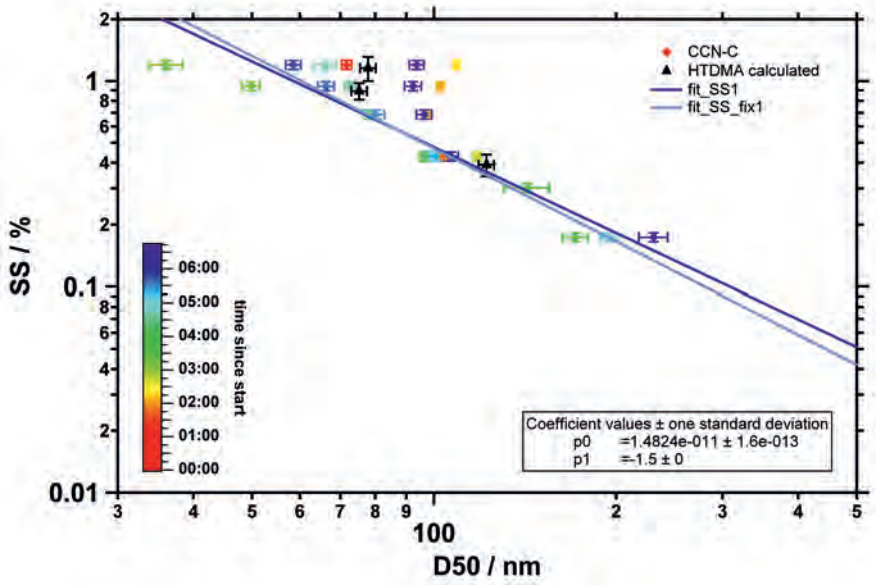

Figure A.28: *Measured $SS_{crit}/D50$ pairs for experiment 30_2: JPAC, PC 30° C.*

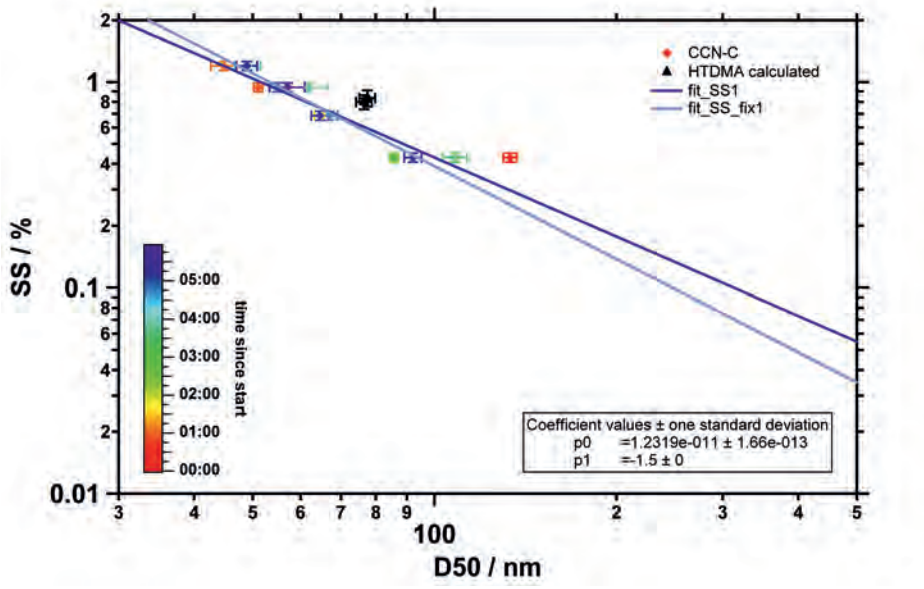

Figure A.29: *Measured SS_{crit}/D50 pairs for experiment 35D_1: JPAC, PC 35°C, lights off in PC.*

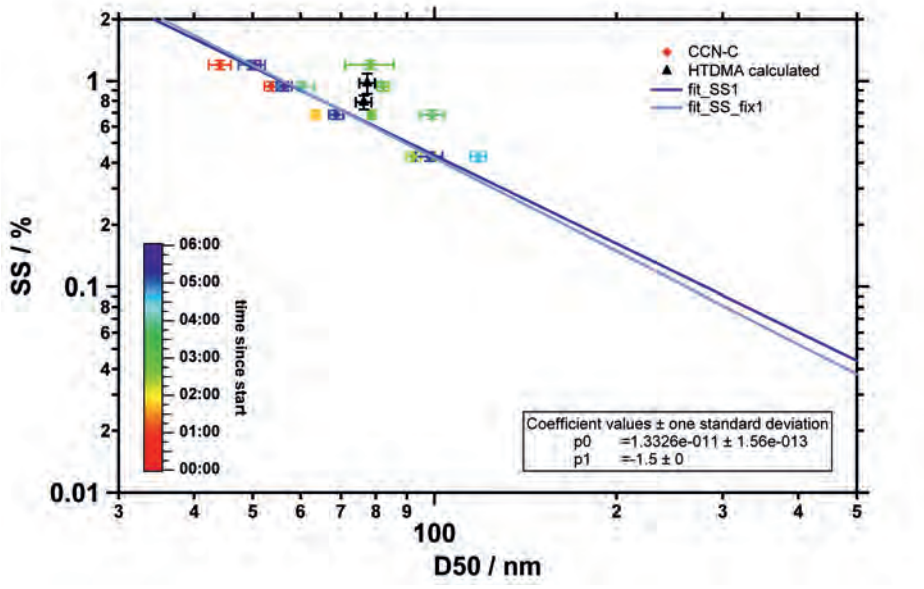

Figure A.30: *Measured SS_{crit}/D50 pairs for experiment 35D_2: JPAC, PC 35°C, lights off in PC.*

A.2 Hygroscopic growth data

In the following, the measured growth curves (diamonds) and fits calculated with UNIFAC (lines) for all experiments are presented. To enhance clarity, the error bars are only shown for the first data set. They are representative for all data sets. The measurements are numbered according to the time they were taken. Numbers from 1 to 3 indicate measurements on the first day of a SAPHIR chamber experiment. 4 to 6 are measurements on the second day. For JPAC experiments 1 and 2 are particles from the mode nucleated first and 3 and 4 are from the second mode. To enable direct compatibility between measurements with different dry particle sizes (50 - 250 nm), GF is plotted vs a_w as the Kelvin effect is eliminated this way.
In the table A.1 and A.2 GF, κ, and ϕ at 90% RH are listed for all measurements.

A.2.1 BMT- and α-pinene experiments in SAPHIR

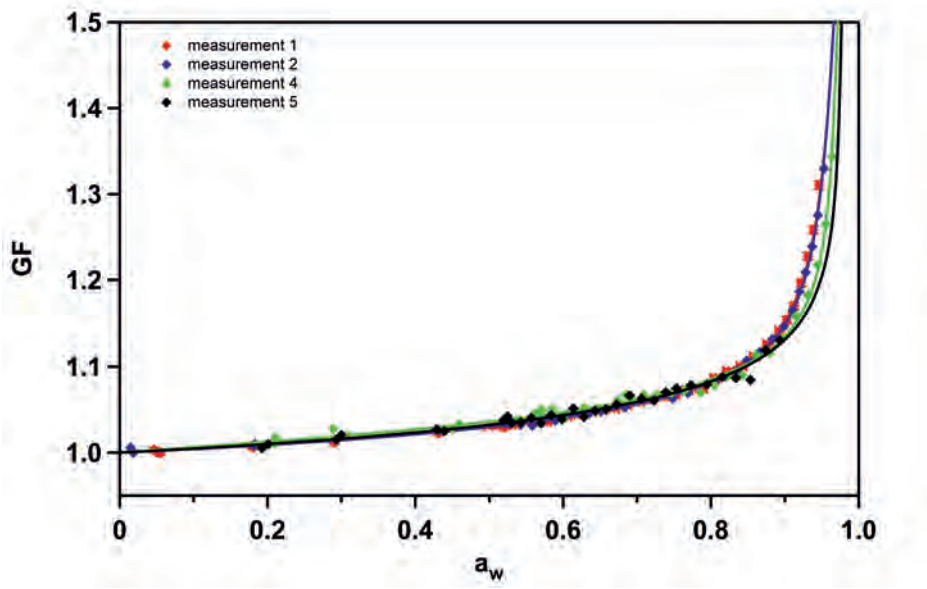

Figure A.31: *Measured growth curves for experiment 1: SAPHIR, 500 ppbC BMT, type A, b/c.*

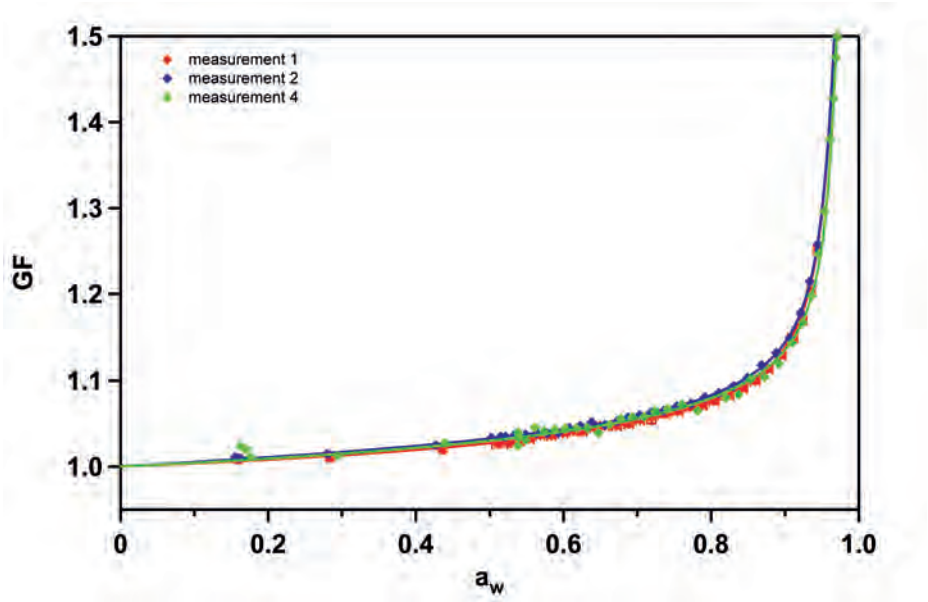

Figure A.32: *Measured growth curves for experiment 2: SAPHIR, 500 ppbC BMT without ocimene, type A, b/c.*

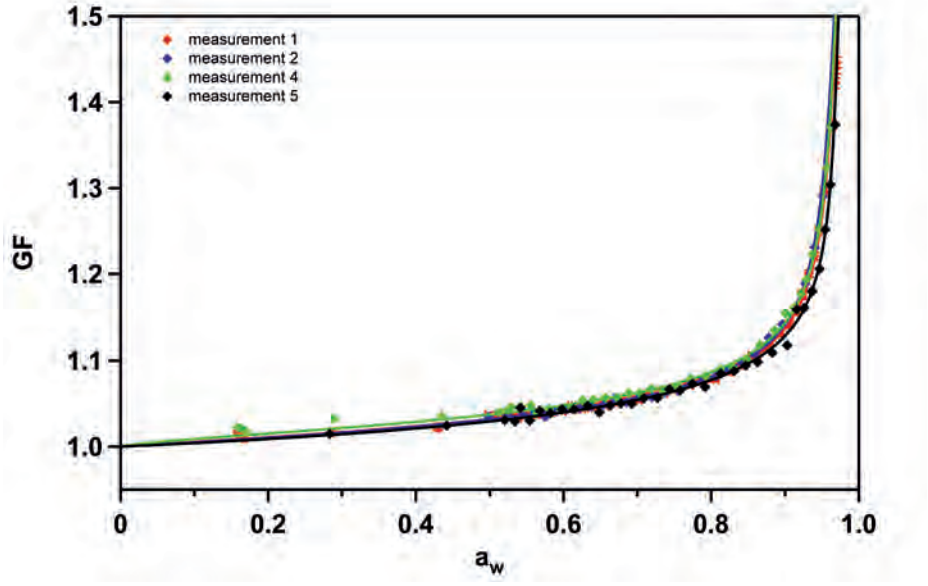

Figure A.33: *Measured growth curves for experiment 3: SAPHIR, 1000 ppbC BMT, type A, b/b.*

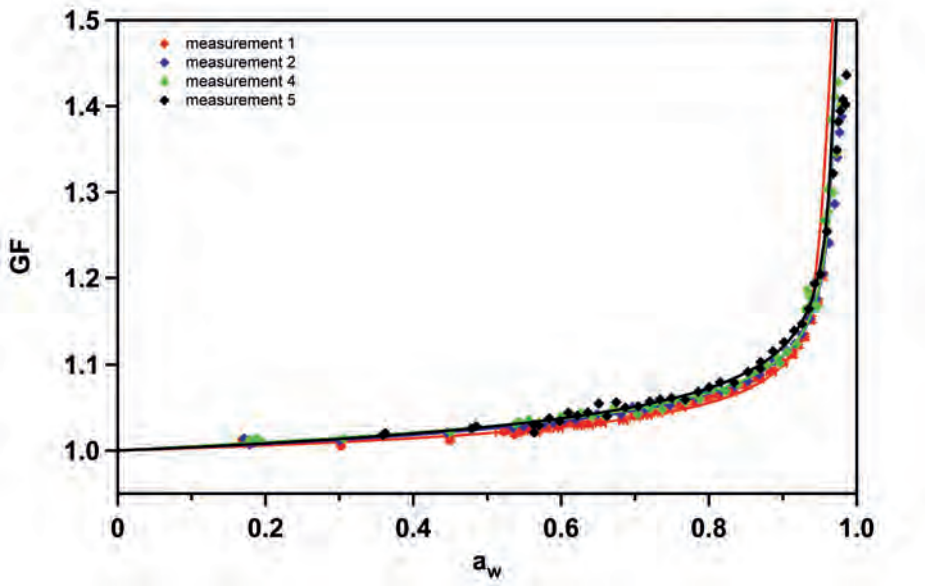

Figure A.34: *Measured growth curves for experiment 4: SAPHIR, 500 ppbC BMT + 45 ppbC SQT, type A, c/c.*

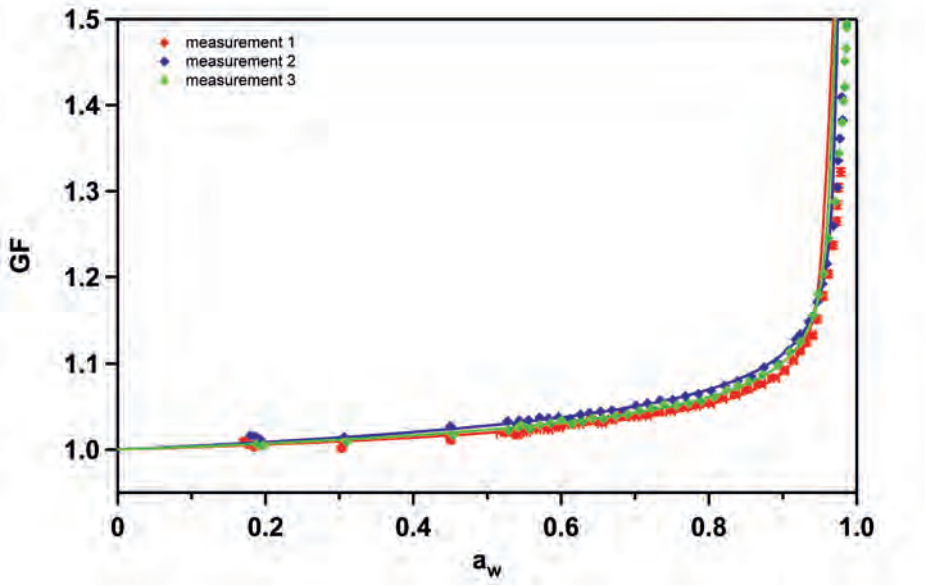

Figure A.35: *Measured growth curves for experiment 5: SAPHIR, 1000 ppbC BMT, type A, c/c.*

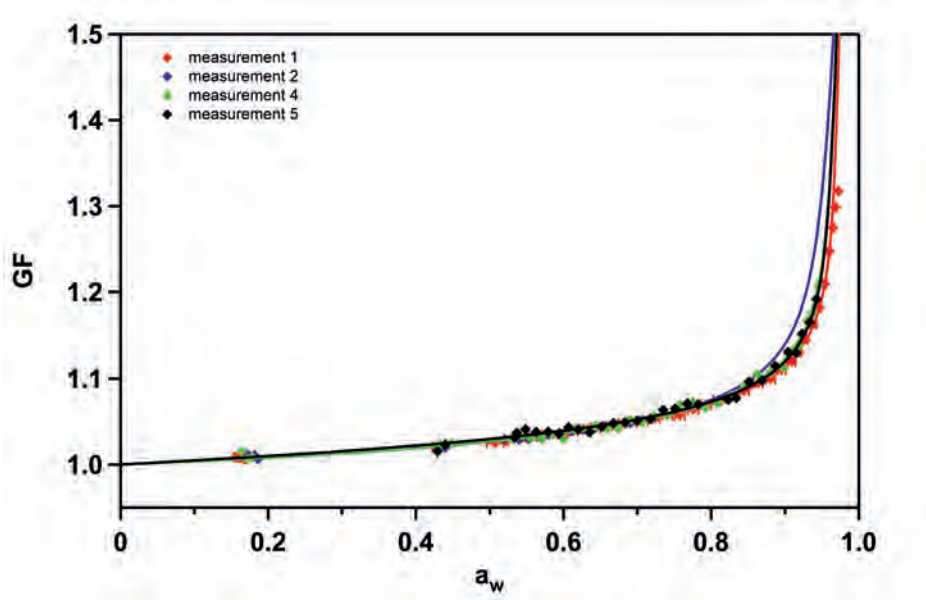

Figure A.36: *Measured growth curves for experiment 6: SAPHIR, 1000 ppbC BMT without ocimene, type A, c/b.*

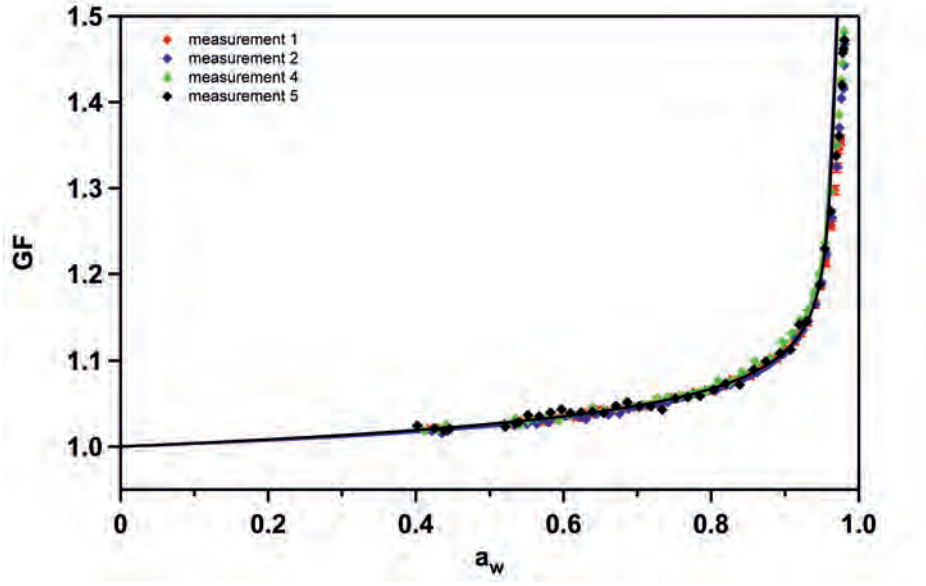

Figure A.37: *Measured growth curves for experiment 7: SAPHIR, 1000 ppbC BMT + 45 ppbC SQT, type A, b/b.*

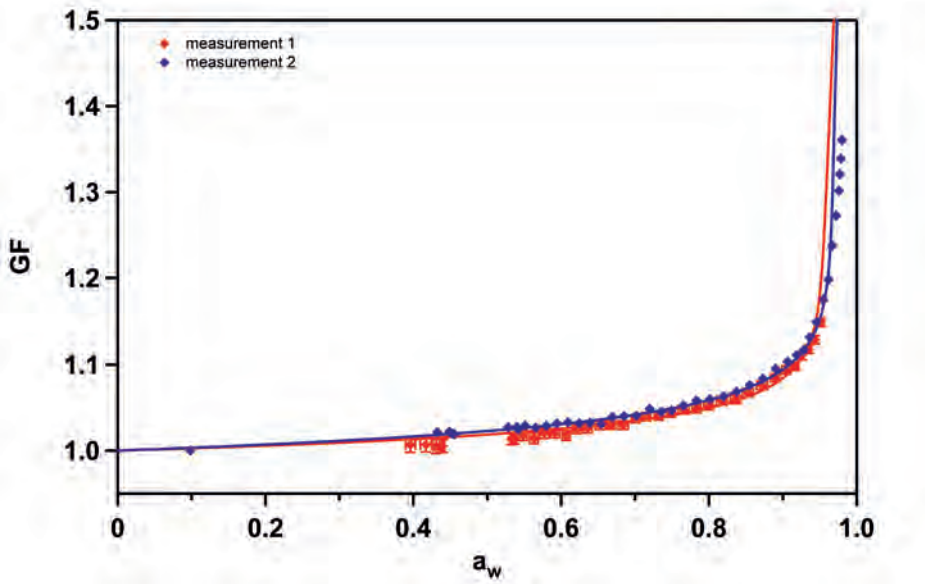

Figure A.38: *Measured growth curves for experiment 8: SAPHIR, 1000 ppbC BMT, 200 ppb O_3, type B*, dark. Red line is a fit with fixed exponent to the data of the first 6h.*

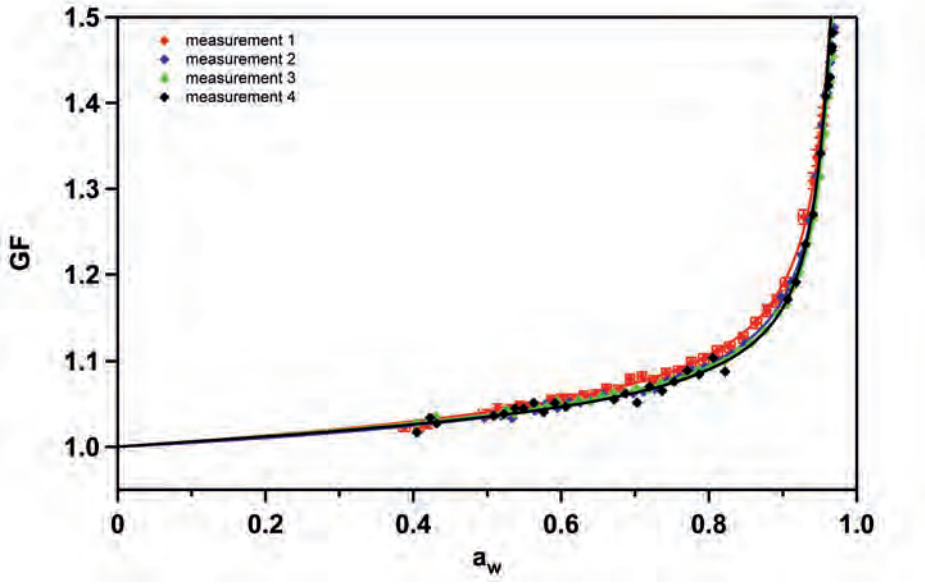

Figure A.39: *Measured growth curves for experiment 11: SAPHIR, 3x40 ppbC BMT, type A, b/b.*

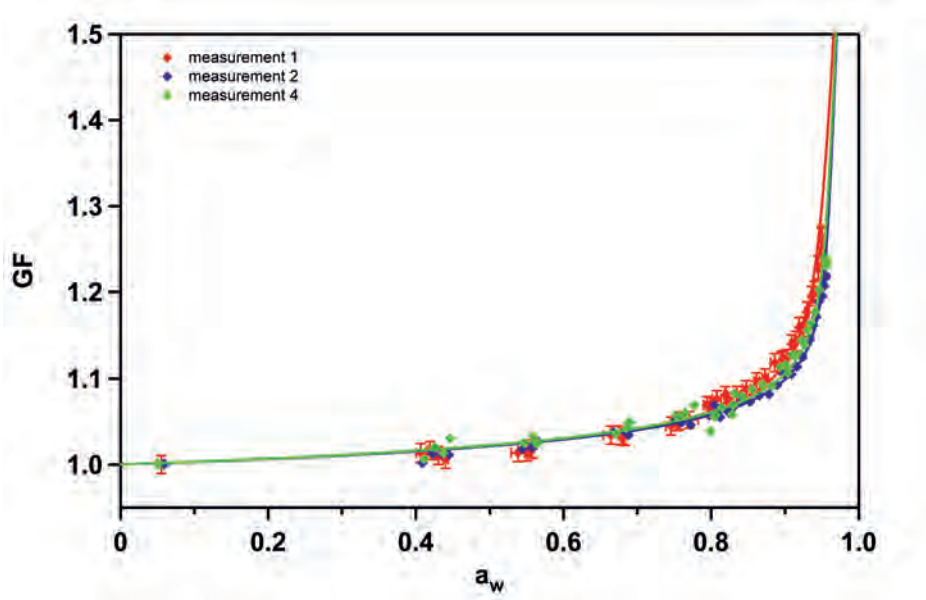

Figure A.40: *Measured growth curves for experiment 20: SAPHIR, 100 ppbC α-pinene, type B, b/dark.*

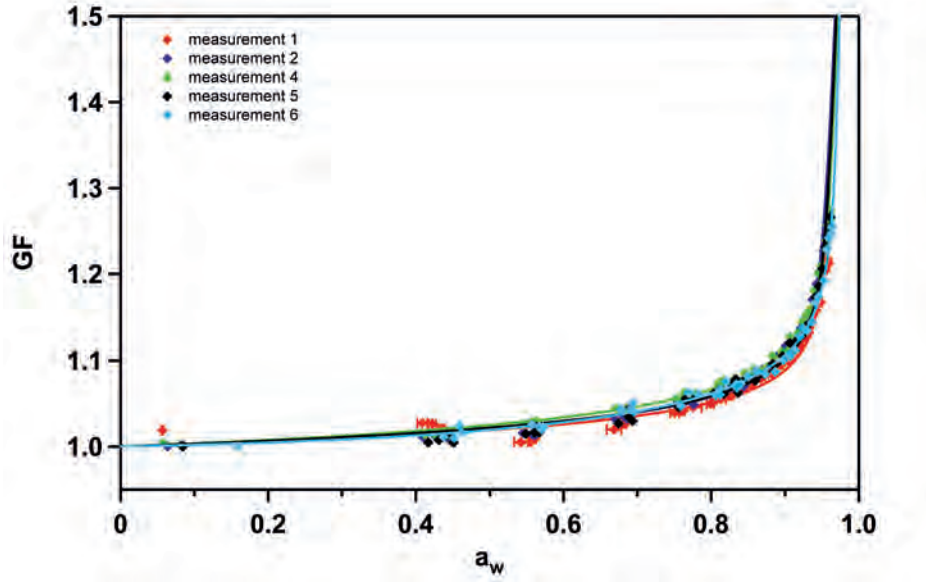

Figure A.41: *Measured growth curves for experiment 21: SAPHIR, 400 ppbC α-pinene, type B, b/b.*

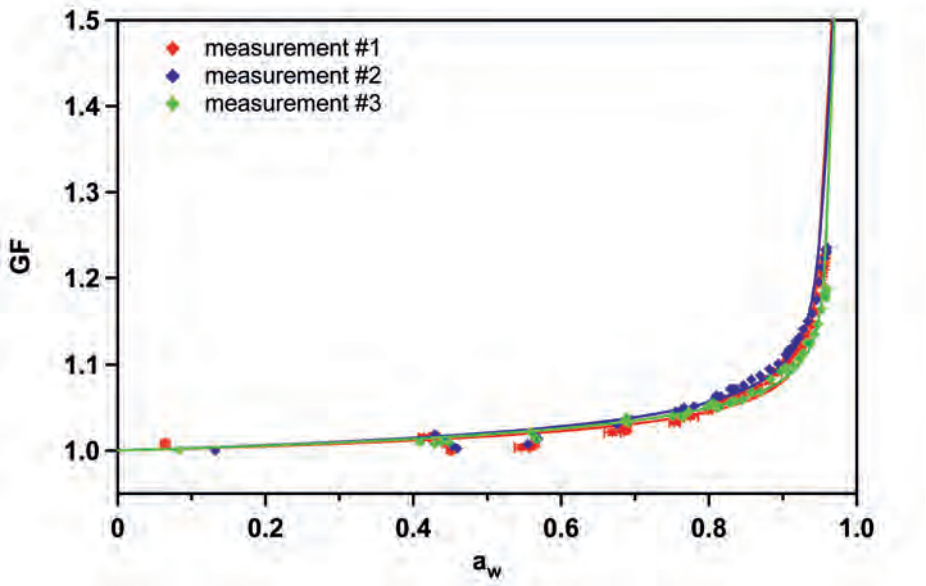

Figure A.42: *Measured growth curves for experiment 22: SAPHIR, 400 ppbC α-pinene + 300 ppm CO, type B, b/b.*

Table A.1: *GF, κ, ρ_{ion}, and ϕ at 90% RH for all HTDMA measurements at SAPHIR. The given errors are the accuracy calculated according to equation 4.5.*

exp No.	#	GF	κ	ρ_{ion}	ϕ
1	1	1.12 ± 0.01	0.059 ± 0.010	3065 ± 534	0.44 ± 0.08
	2	1.13 ± 0.01	0.058 ± 0.010	3033 ± 497	0.43 ± 0.07
	4	1.13 ± 0.01	0.054 ± 0.009	2816 ± 489	0.40 ± 0.07
2	1	1.11 ± 0.01	0.053 ± 0.010	2774 ± 506	0.40 ± 0.07
	2	1.13 ± 0.01	0.058 ± 0.010	3018 ± 501	0.43 ± 0.07
	4	1.12 ± 0.01	0.050 ± 0.009	2609 ± 472	0.37 ± 0.07
3	1	1.12 ± 0.01	0.055 ± 0.009	2864 ± 482	0.41 ± 0.07
	2	1.13 ± 0.01	0.057 ± 0.009	2955 ± 443	0.42 ± 0.06
	4	1.12 ± 0.01	0.052 ± 0.008	2694 ± 420	0.38 ± 0.06
	5	1.12 ± 0.01	0.048 ± 0.007	2516 ± 390	0.36 ± 0.06
4	1	1.09 ± 0.01	0.040 ± 0.009	2087 ± 452	0.30 ± 0.06
	2	1.11 ± 0.01	0.044 ± 0.008	2321 ± 396	0.33 ± 0.06
	4	1.10 ± 0.01	0.041 ± 0.007	2163 ± 385	0.31 ± 0.06
	5	1.12 ± 0.01	0.051 ± 0.008	2649 ± 392	0.38 ± 0.06
5	1	1.09 ± 0.01	0.036 ± 0.008	1856 ± 396	0.27 ± 0.06
	2	1.10 ± 0.01	0.042 ± 0.007	2178 ± 387	0.31 ± 0.06
	3	1.11 ± 0.01	0.042 ± 0.007	2192 ± 363	0.31 ± 0.05
6	1	1.11 ± 0.01	0.044 ± 0.009	2314 ± 443	0.33 ± 0.06
	4	1.11 ± 0.01	0.046 ± 0.008	2391 ± 401	0.34 ± 0.06
	5	1.12 ± 0.01	0.047 ± 0.007	2456 ± 388	0.35 ± 0.06
7	1	1.10 ± 0.01	0.044 ± 0.008	2302 ± 437	0.33 ± 0.06
	2	1.10 ± 0.01	0.043 ± 0.007	2248 ± 390	0.32 ± 0.06
	4	1.11 ± 0.01	0.046 ± 0.008	2427 ± 402	0.35 ± 0.06
	5	1.11 ± 0.01	0.045 ± 0.007	2337 ± 375	0.33 ± 0.05
8	1	1.09 ± 0.01	0.038 ± 0.007	1993 ± 348	0.28 ± 0.05
	2	1.09 ± 0.01	0.038 ± 0.007	2008 ± 348	0.29 ± 0.05
9	1	1.15 ± 0.01	0.078 ± 0.015	4036 ± 803	0.58 ± 0.11
11	1	1.15 ± 0.01	0.079 ± 0.015	4057 ± 784	0.58 ± 0.11
	2	1.14 ± 0.01	0.067 ± 0.012	3502 ± 618	0.50 ± 0.09
	3	1.14 ± 0.01	0.067 ± 0.012	3462 ± 612	0.49 ± 0.09
	5	1.15 ± 0.01	0.074 ± 0.012	3811 ± 640	0.54 ± 0.09
20	1	1.11 ± 0.01	0.050 ± 0.010	2761 ± 504	0.37 ± 0.07
	2	1.09 ± 0.01	0.037 ± 0.009	2072 ± 446	0.28 ± 0.06
	4	1.10 ± 0.01	0.042 ± 0.008	2358 ± 441	0.32 ± 0.06
21	1	1.09 ± 0.01	0.037 ± 0.008	2056 ± 416	0.28 ± 0.06
	2	1.10 ± 0.01	0.043 ± 0.008	2364 ± 438	0.32 ± 0.06
	4	1.11 ± 0.01	0.045 ± 0.008	2486 ± 407	0.33 ± 0.06
	5	1.10 ± 0.01	0.041 ± 0.008	2283 ± 392	0.31 ± 0.06
	6	1.09 ± 0.01	0.037 ± 0.007	2056 ± 362	0.28 ± 0.05
22	1	1.09 ± 0.01	0.036 ± 0.008	1992 ± 407	0.27 ± 0.06
	2	1.10 ± 0.01	0.041 ± 0.008	2261 ± 392	0.30 ± 0.06
	3	1.09 ± 0.01	0.035 ± 0.007	1956 ± 367	0.26 ± 0.05

A.2.2 JPAC experiments

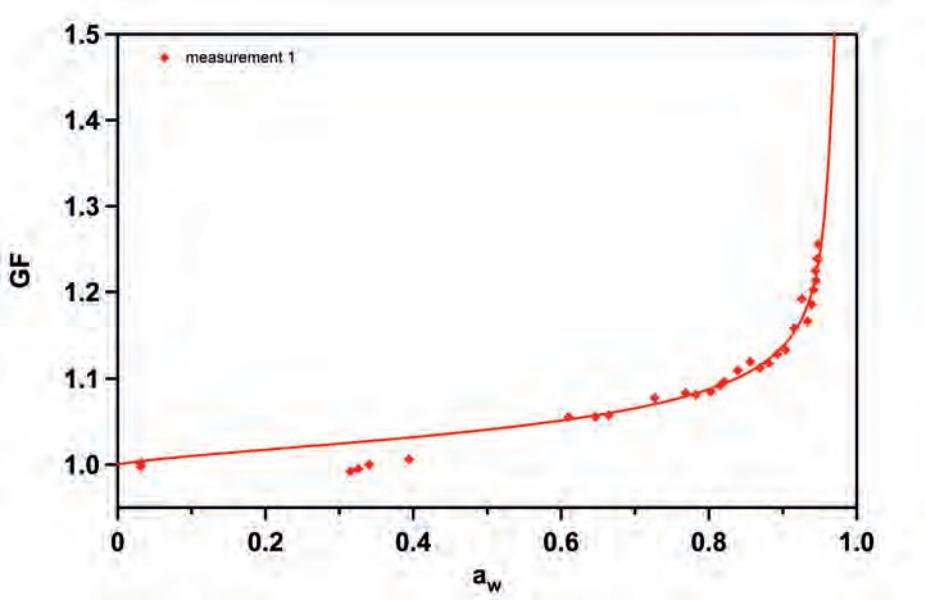

Figure A.43: *Measured growth curves for experiment 15_1: JPAC, PC 15° C.*

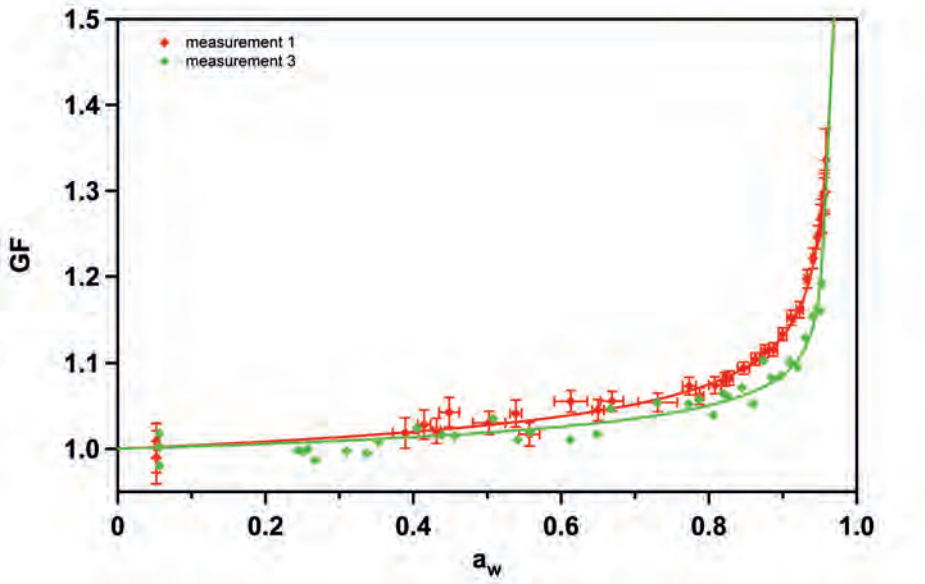

Figure A.44: *Measured growth curves for experiment 15_4: JPAC, PC 15° C.*

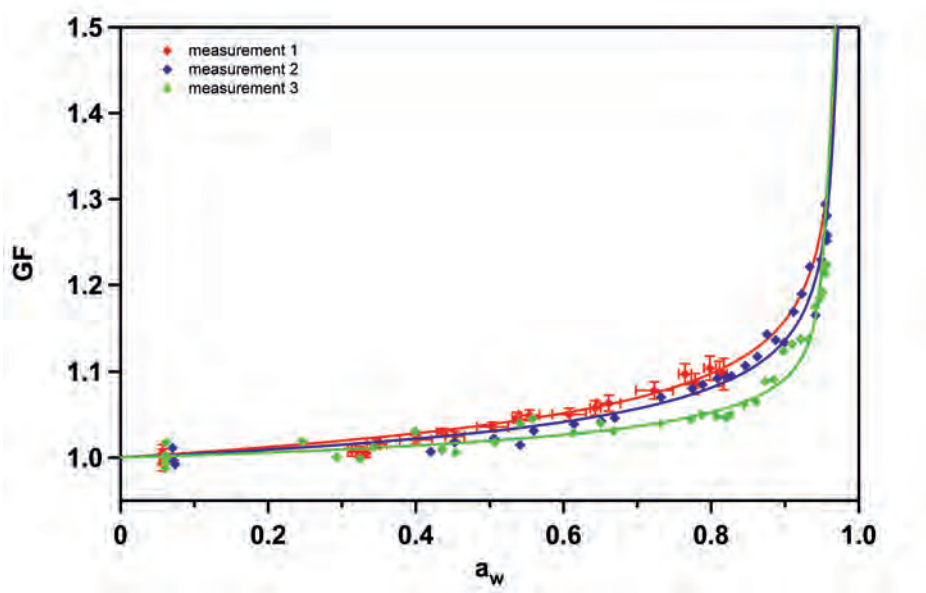

Figure A.45: *Measured growth curves for experiment 15_5: JPAC, PC 15° C.*

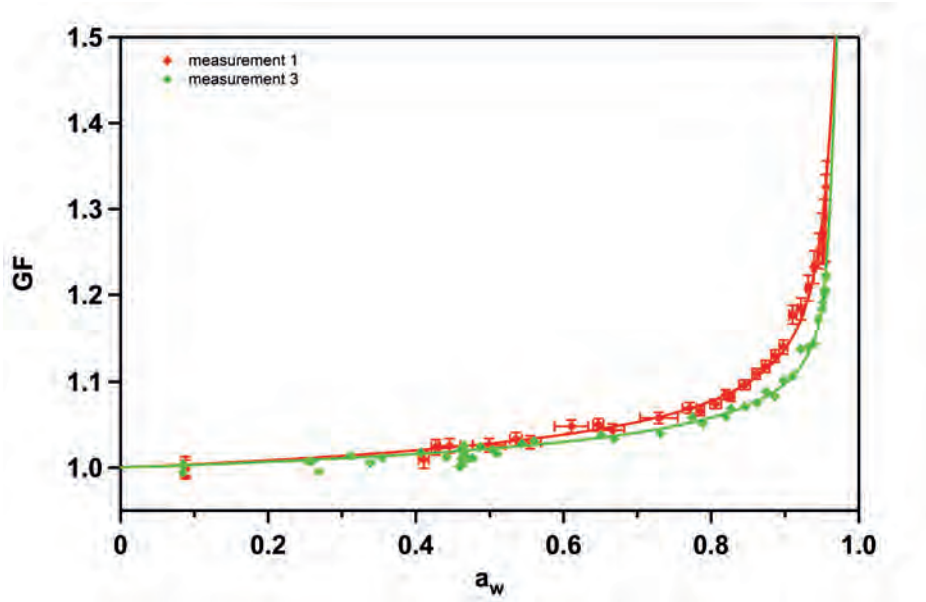

Figure A.46: *Measured growth curves for experiment 15_7: JPAC, PC 15° C.*

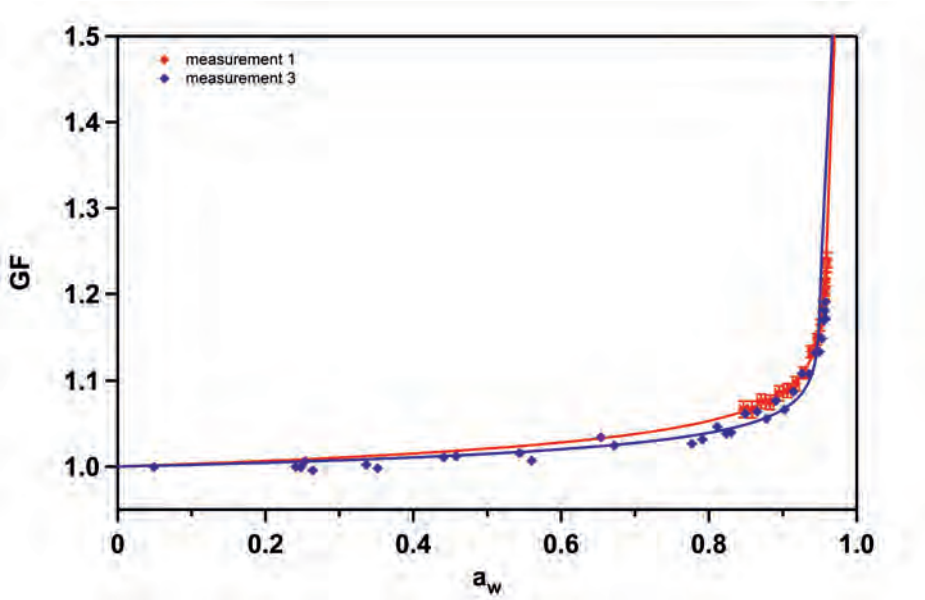

Figure A.47: *Measured growth curves for experiment 20_1: JPAC, PC 20° C.*

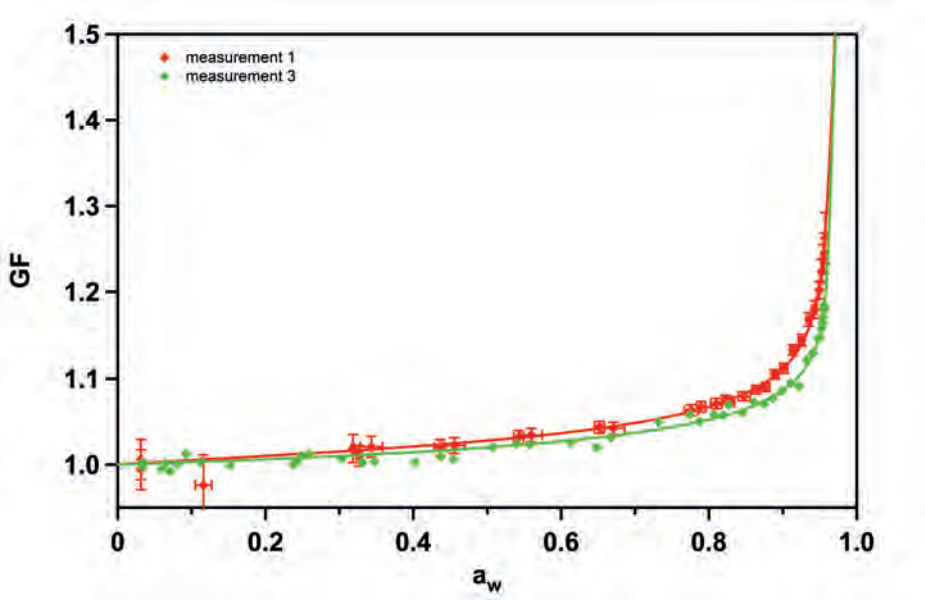

Figure A.48: *Measured growth curves for experiment 20_2: JPAC, PC 20° C.*

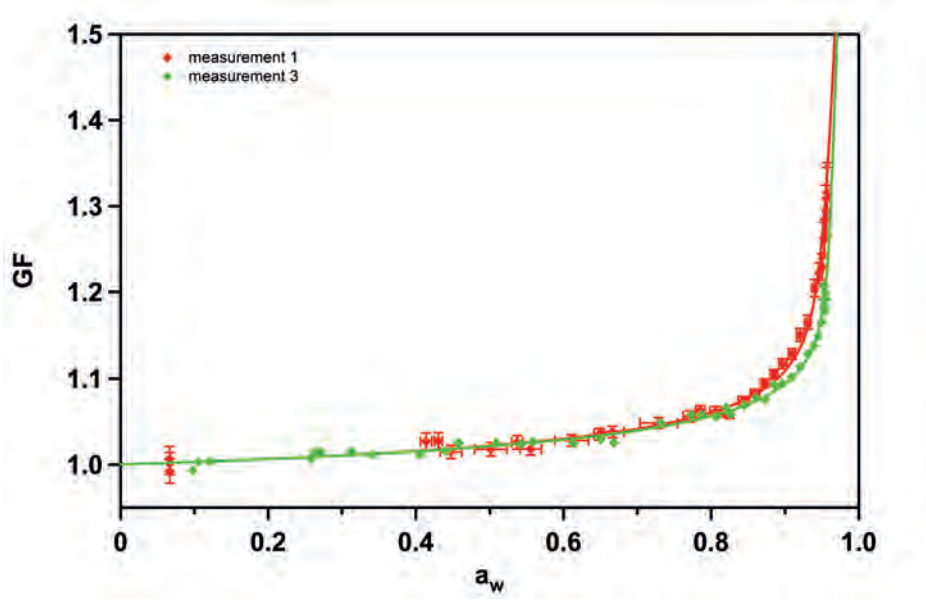

Figure A.49: *Measured growth curves for experiment 20_3: JPAC, PC 20° C.*

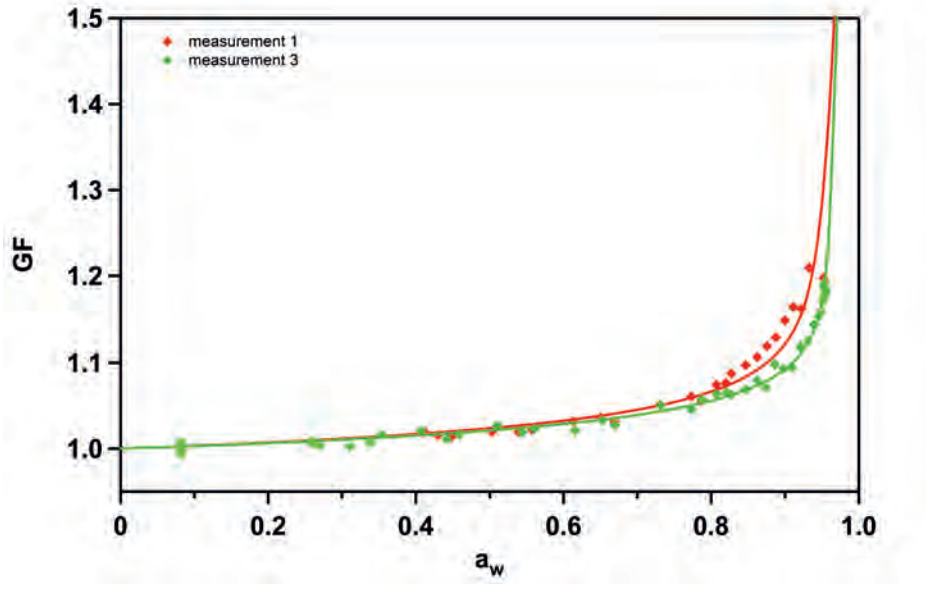

Figure A.50: *Measured growth curves for experiment 20_4: JPAC, PC 20° C.*

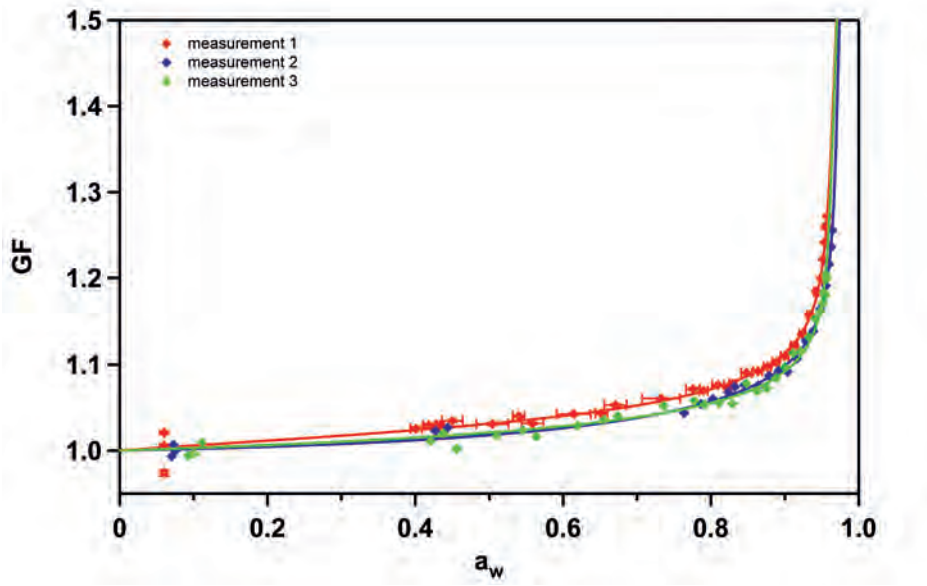

Figure A.51: *Measured growth curves for experiment 25_1: JPAC, PC 25° C.*

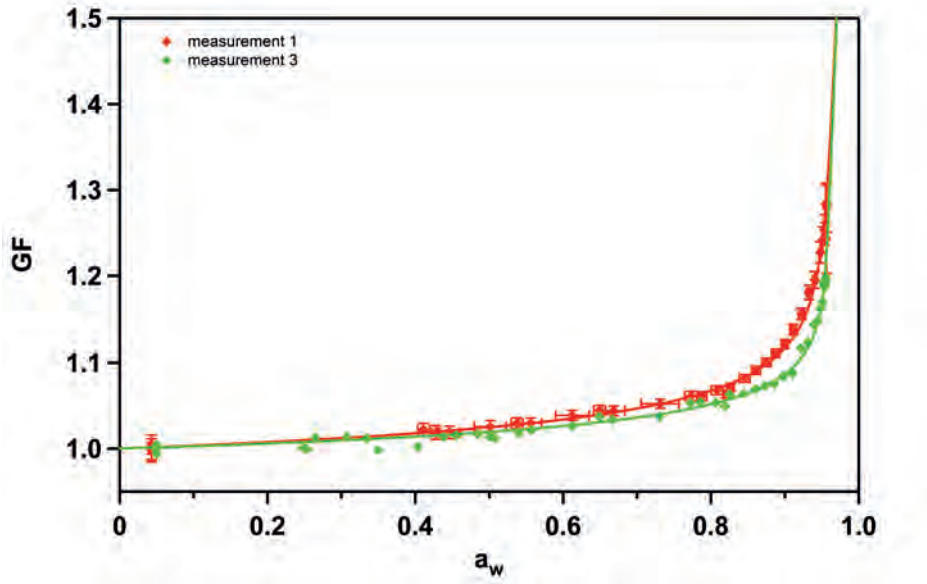

Figure A.52: *Measured growth curves for experiment 25_2: JPAC, PC 25° C.*

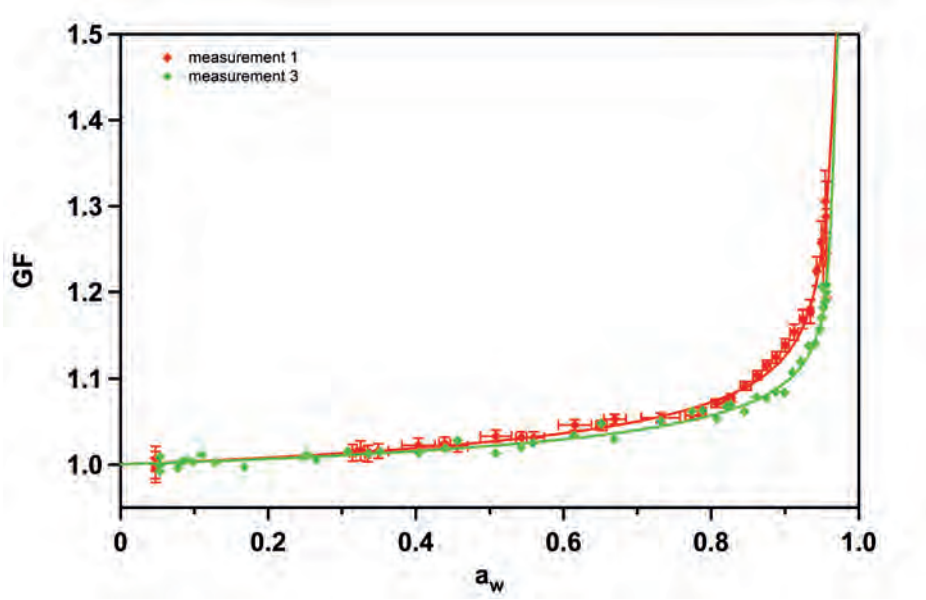

Figure A.53: *Measured growth curves for experiment 25_3: JPAC, PC 25° C.*

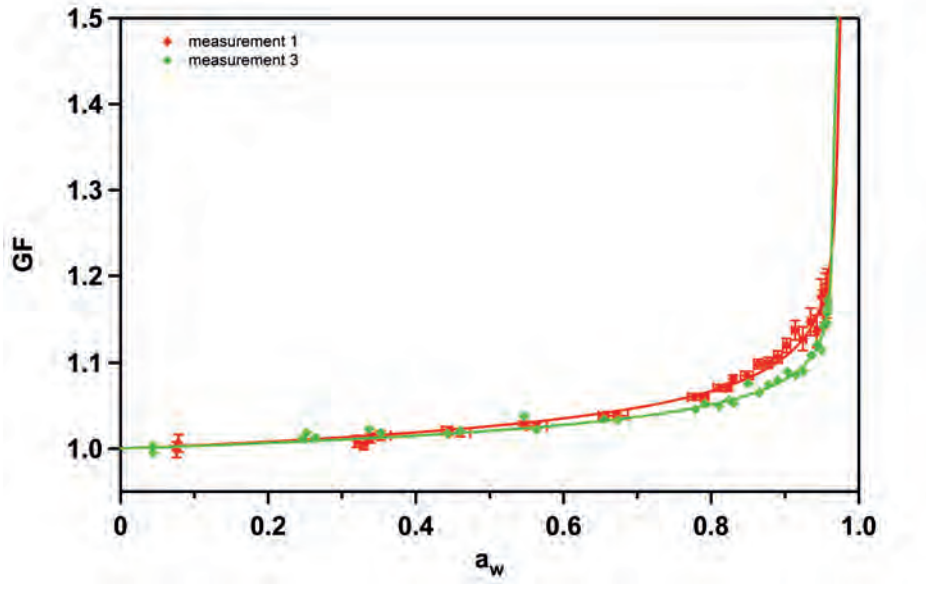

Figure A.54: *Measured growth curves for experiment 30_1: JPAC, PC 30° C.*

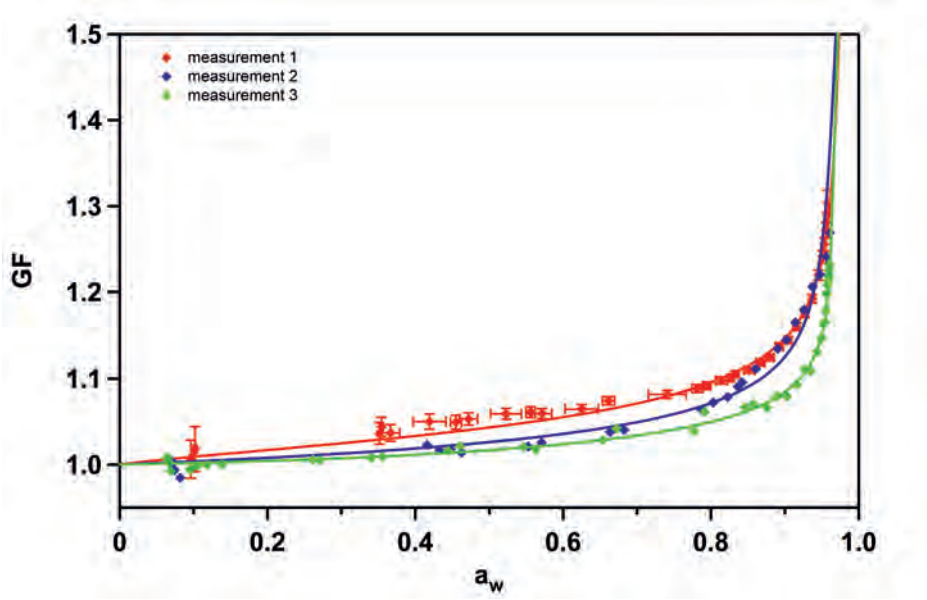

Figure A.55: *Measured growth curves for experiment 30_2: JPAC, PC 30° C.*

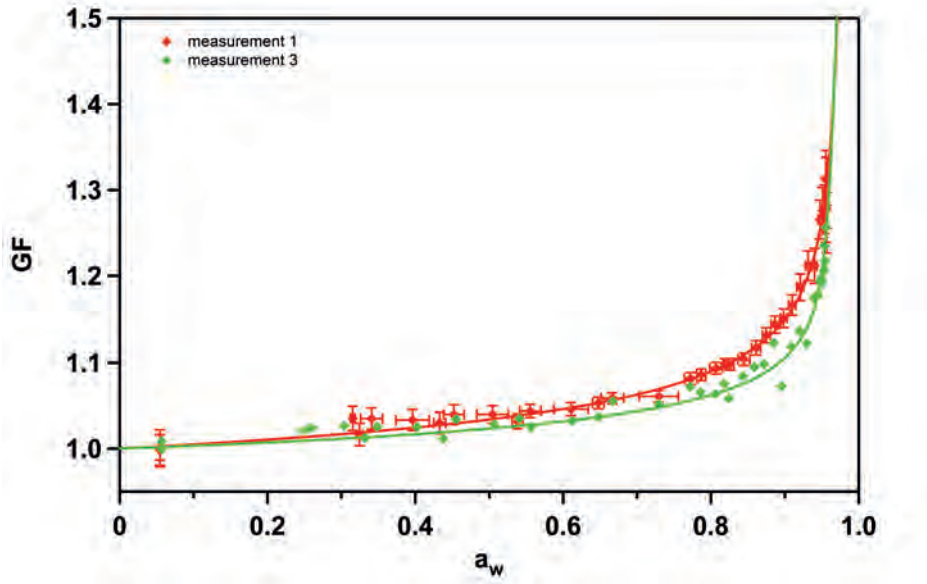

Figure A.56: *Measured growth curves for experiment 35D_1: JPAC, PC 35° C, lights off in PC.*

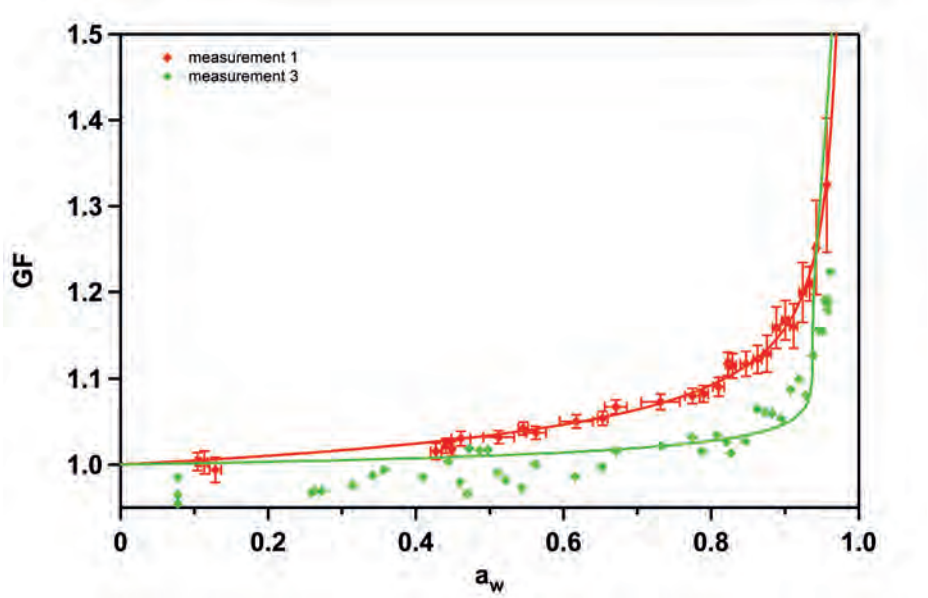

Figure A.57: *Measured growth curves for experiment 35D_2: JPAC, PC 35° C, lights off in PC.*

Table A.2: *GF, κ, ρ_{ion}, and ϕ at 90% RH for all HTDMA measurements at JPAC. The given errors are the accuracy calculated according to equation 4.5.*

exp No.	#	*GF*	κ	ρ_{ion}	ϕ
20_1	1	1.08 ± 0.01	0.034 ± 0.009	1782 ± 458	0.25 ± 0.07
	3	1.03 ± 0.01	0.013 ± 0.006	693 ± 300	0.10 ± 0.04
20_2	1	1.06 ± 0.01	0.025 ± 0.008	1276 ± 394	0.18 ± 0.06
	3	1.04 ± 0.01	0.019 ± 0.007	994 ± 347	0.14 ± 0.05
30_1	1	1.07 ± 0.01	0.030 ± 0.008	1573 ± 436	0.22 ± 0.06
	3	1.04 ± 0.01	0.019 ± 0.007	980 ± 349	0.14 ± 0.05
30_2	1	1.08 ± 0.01	0.036 ± 0.009	1884 ± 480	0.27 ± 0.07
	2	1.11 ± 0.01	0.047 ± 0.008	2454 ± 443	0.35 ± 0.06
	3	1.04 ± 0.01	0.017 ± 0.006	882 ± 332	0.13 ± 0.05
15_1	1	1.10 ± 0.01	0.048 ± 0.012	2482 ± 624	0.35 ± 0.09
25_1	1	1.07 ± 0.01	0.032 ± 0.009	1664 ± 446	0.24 ± 0.06
	2	1.07 ± 0.01	0.029 ± 0.007	1536 ± 358	0.22 ± 0.05
	3	1.05 ± 0.01	0.021 ± 0.007	1063 ± 359	0.15 ± 0.05
25_2	1	1.07 ± 0.01	0.032 ± 0.008	1649 ± 439	0.24 ± 0.06
	3	1.05 ± 0.01	0.020 ± 0.007	1062 ± 363	0.15 ± 0.05
25_3	1	1.09 ± 0.01	0.040 ± 0.009	2083 ± 490	0.30 ± 0.07
	3	1.05 ± 0.01	0.023 ± 0.007	1207 ± 380	0.17 ± 0.05
35D_1	1	1.09 ± 0.01	0.044 ± 0.010	2297 ± 513	0.33 ± 0.07
	3	1.09 ± 0.01	0.039 ± 0.009	2005 ± 486	0.29 ± 0.07
15_4	1	1.09 ± 0.01	0.044 ± 0.010	2297 ± 516	0.33 ± 0.07
	3	1.07 ± 0.01	0.031 ± 0.008	1593 ± 433	0.23 ± 0.06
15_5	1	1.14 ± 0.01	0.066 ± 0.012	3449 ± 619	0.49 ± 0.09
	3	1.07 ± 0.01	0.029 ± 0.008	1492 ± 425	0.21 ± 0.06
15_7	1	1.09 ± 0.01	0.038 ± 0.009	1999 ± 490	0.29 ± 0.07
	3	1.07 ± 0.01	0.031 ± 0.008	1595 ± 433	0.23 ± 0.06
20_3	1	1.07 ± 0.01	0.033 ± 0.009	1708 ± 453	0.24 ± 0.06
	3	1.05 ± 0.01	0.023 ± 0.007	1201 ± 387	0.17 ± 0.06
20_4	1	1.09 ± 0.01	0.042 ± 0.010	2177 ± 499	0.31 ± 0.07
	3	1.06 ± 0.01	0.024 ± 0.008	1239 ± 392	0.18 ± 0.06
35D_2	1	1.10 ± 0.01	0.046 ± 0.010	2373 ± 522	0.34 ± 0.07
	3	1.06 ± 0.01	0.027 ± 0.008	1385 ± 410	0.20 ± 0.06

A.3 $\phi(a_w)$ curves from HTDMA measurements

In this section the $\phi(a_w)$ curves calculated for the whole range of the measured growth curves are shown.

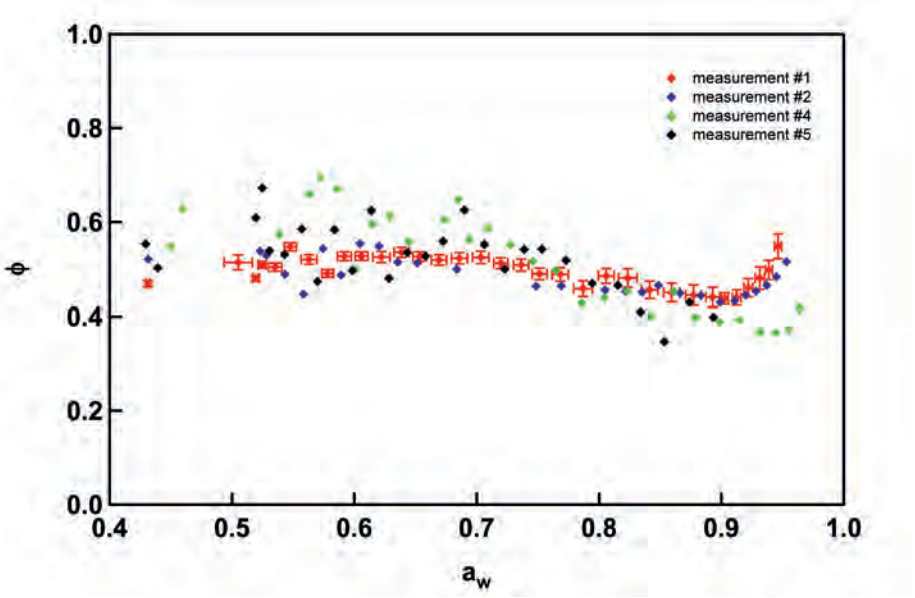

Figure A.58: *Calculated $\phi(a_w)$ curves for experiment 1: SAPHIR, 500 ppbC BMT, type A, b/c.*

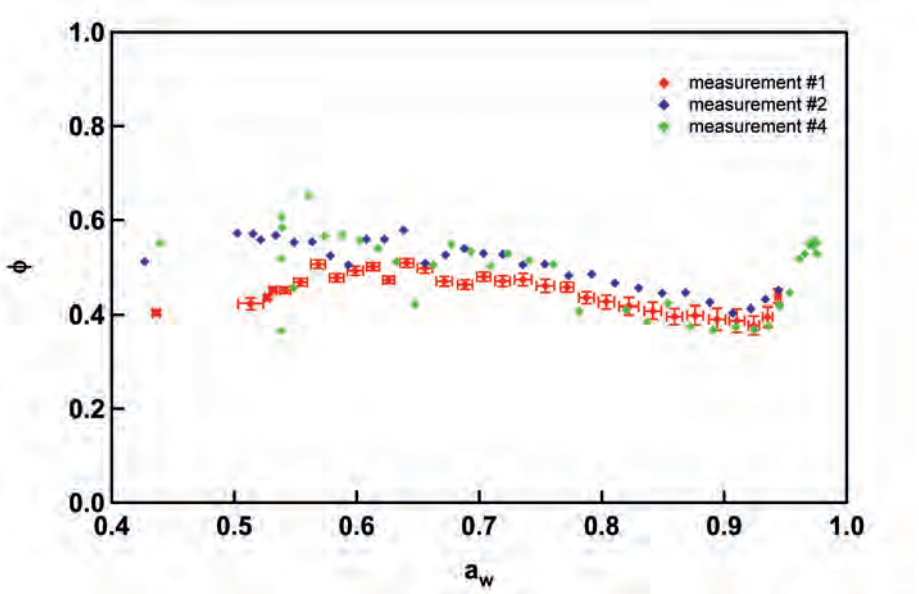

Figure A.59: *Calculated $\phi(a_w)$ curves for experiment 2: SAPHIR, 500 ppbC BMT without ocimene, type A, b/c.*

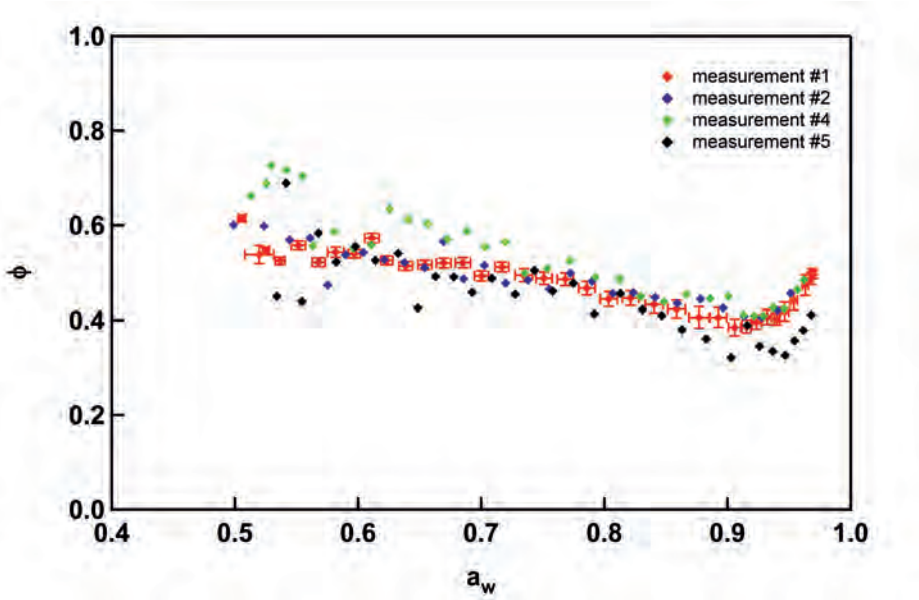

Figure A.60: *Calculated $\phi(a_w)$ curves for experiment 3: SAPHIR, 1000 ppbC BMT, type A, b/b.*

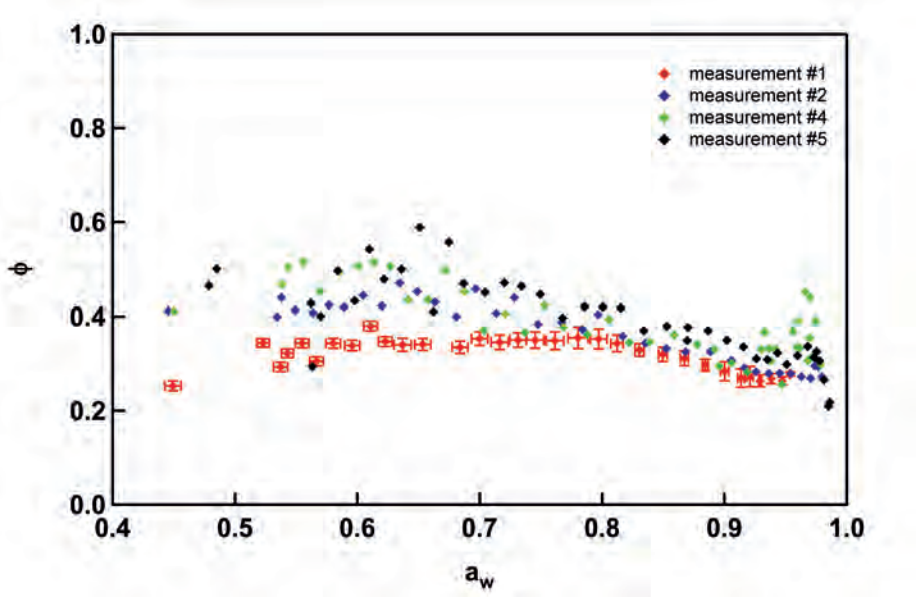

Figure A.61: *Calculated $\phi(a_w)$ curves for experiment 4: SAPHIR, 500 ppbC BMT + 45 ppbC SQT, type A, c/c.*

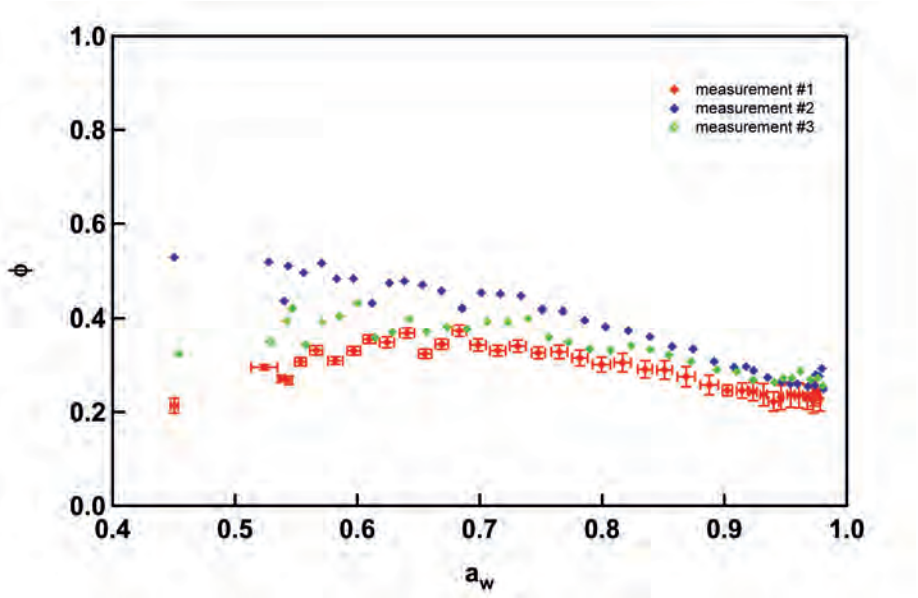

Figure A.62: *Calculated $\phi(a_w)$ curves for experiment 5: SAPHIR, 1000 ppbC BMT, type A, c/c.*

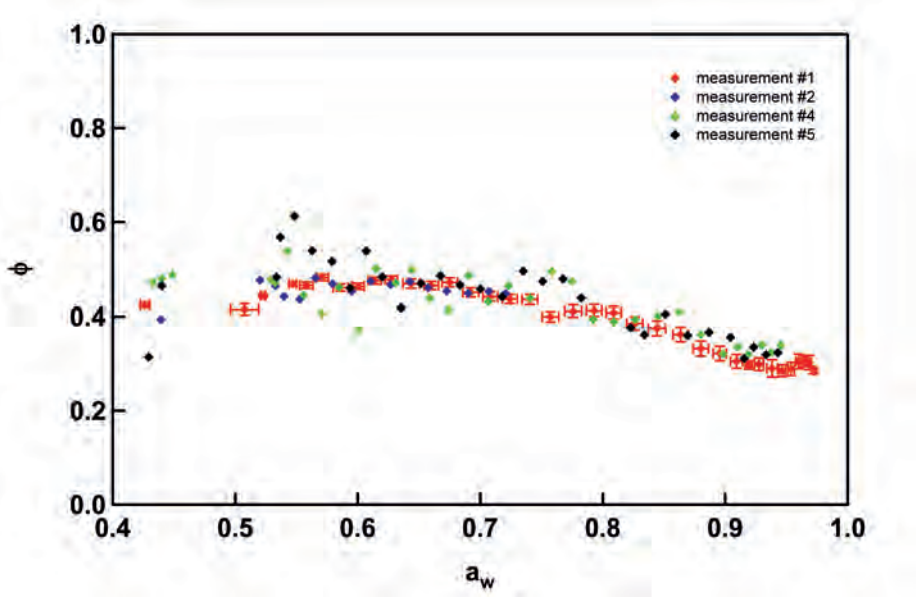

Figure A.63: *Calculated $\phi(a_w)$ curves for experiment 6: SAPHIR, 1000 ppbC BMT without ocimene, type A, c/b.*

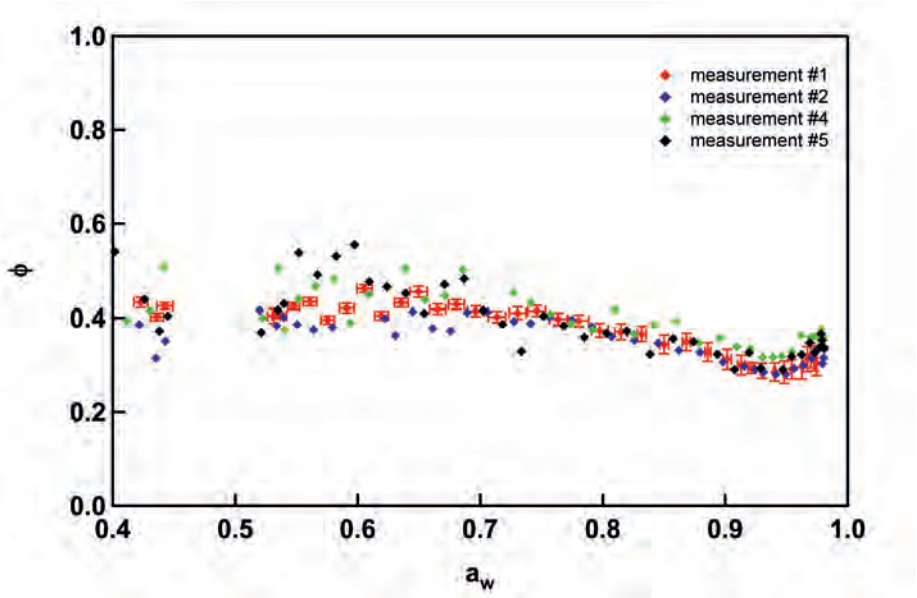

Figure A.64: *Calculated $\phi(a_w)$ curves for experiment 7: SAPHIR, 1000 ppbC BMT + 45 ppbC SQT, type A, b/b.*

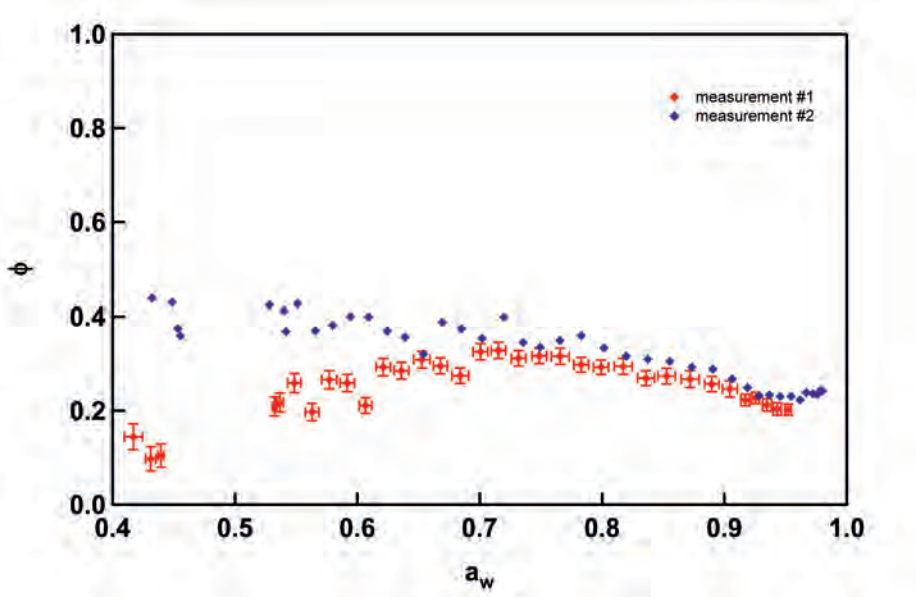

Figure A.65: *Calculated $\phi(a_w)$ curves for experiment 8: SAPHIR, 1000 ppbC BMT, 200 ppb O_3, type B*, dark. Red line is a fit with fixed exponent to the data of the first 6h.*

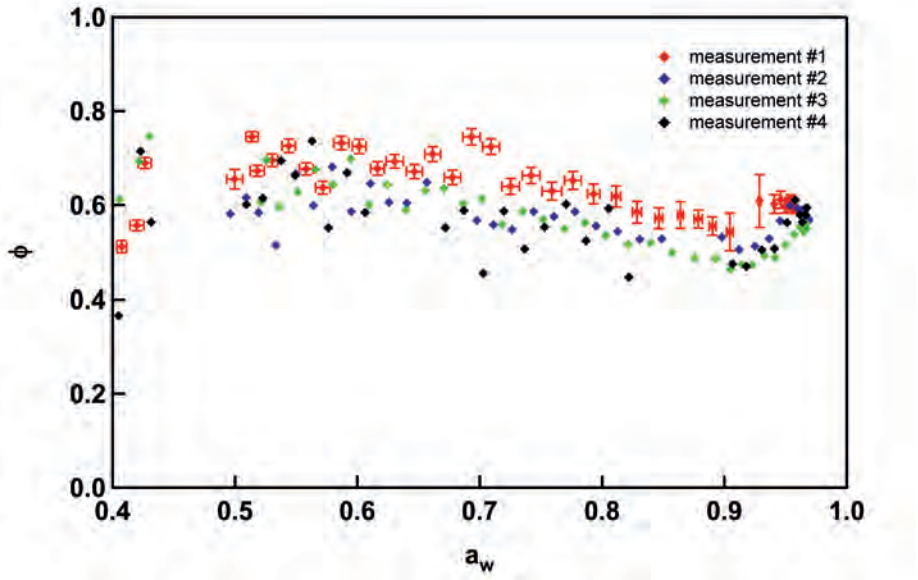

Figure A.66: *Calculated $\phi(a_w)$ curves for experiment 11: SAPHIR, 3x40 ppbC BMT, type A, b/b.*

A.4 Primary OH production

In the following table the integrated $j(O^1D)$, $[O_3]$, and potential OH are listed for all HTDMA measurements at SAPHIR. All quantities are integrated from opening the roof of the chamber until the end of the humidogram measurement. In the last three columns $j(O^1D)$, $[O_3]$, and OH_{pot} are scaled with the initial VOC concentration in each experiment.

Table A.3: *Integrated $j(O^1D)$, $[O_3]$, and potential OH ($[OH_{pot}]$) for all experiment. The last three columns are the values presented in the previous columns scaled with the initial VOC concentration.*

exp No.	#	$\int j(O^1D)$	$\int [O_3] \cdot 10^6$	$\int OH_{pot} \cdot 10^{10}$	$\int j(O^1D)^s \cdot 10^{-3}$	$\int [O_3]^s$	$\int OH_{pot}^s \cdot 10^7$
1	1	0.12	0.45	1.91	0.242	894	3.8
	2	0.15	1.84	2.04	0.296	3689	4.1
	4	0.22	2.05	2.21	0.431	4094	4.4
2	1	0.15	0.47	2.33	0.291	946	4.7
	2	0.20	0.87	3.20	0.396	1741	6.4
	4	0.25	2.76	3.39	0.504	5517	6.8
3	1	0.25	0.62	4.34	0.254	623	4.3
	2	0.29	1.11	5.44	0.292	1108	5.4
	4	0.50	3.87	7.33	0.505	3873	7.3
	5	0.62	4.39	8.66	0.625	4392	8.7
4	1	0.12	0.39	1.24	0.209	678	2.2
	2	0.14	0.69	1.45	0.241	1206	2.5
	4	0.16	1.67	1.50	0.286	2899	2.6
	5	0.18	1.79	1.52	0.319	3118	2.6
5	1	0.10	0.27	0.62	0.101	269	0.6
	2	0.12	0.41	0.69	0.118	414	0.7
	3	0.12	0.49	0.69	0.118	485	0.7
6	1	0.17	0.46	1.99	0.171	457	2.0
	4	0.45	2.46	3.50	0.447	2464	3.5
	5	0.51	3.21	3.82	0.508	3207	3.8
7	1	0.23	0.57	2.26	0.201	499	2.0
	2	0.23	0.85	2.26	0.345	742	0.0
	4	0.40	1.85	2.79	0.345	1610	2.4
	5	0.47	2.06	3.01	0.406	1789	2.6
9	1	0.33	1.25				
11	1	0.18	0.48	3.34	4.545	11959	83.6
	2	0.31	1.06	6.30	3.828	13204	78.7
	3	0.32	1.62	6.73	2.697	13517	56.1
	5	0.41	3.60	7.24	3.399	29962	60.3

B. Acknowledgments

Zum Abschluss gilt mein Dank Prof. Dr. Reinhard Strey für die Übernahme des Referats und die Freiheiten, die er mir in der Ausgestaltung meiner Promotion gelassen hat.
Prof. Dr. Andreas Wahner danke ich für die Übernahme des Koreferats und für die Möglickeit, am ICG-2 des Forschungszentrum Jülich die Arbeiten für diese Promotion durchführen zu können.

Bei meinem Betreuer PD Dr. Thomas Mentel möchte ich mich nicht nur für die vielen fruchtbaren Diskussionen und Anregungen ganz besonders bedanken sondern auch für das in mich gesetzte Vertrauen.
Mein tiefempfundener Dank geht an Michael Decker für die Automatisierungssoftware des HTDMA (Version 2.0). Zusätzlich danke ich für die Beantwortung (fast) aller meiner Computer-Fragen.
Ohne das Team der Pflanzenkammer und von SAPHIR wäre ein Großteil dieser Arbeit nicht möglich gewesen. Deshalb an alle, die für einen reibungslosen Ablauf während der Messkampagnen gesorgt haben und von deren Daten ich profitieren durfte, ein herzliches Dankeschön.
Meinen "Leidensgenossen" Eva Emanuelsson, Tina Claus und Katrin Mildenberger danke ich für einen tollen Sommer 2008 in unseren Containern. Markus Ziese gilt mein Dank, dafür dass er mich in meiner ersten richtigen Kampagne in Karlsruhe unter seine Fittiche genommen hat.
Bei der gesamten Hetero-Gruppe bedanke ich mich für ein hervorragendes Klima und die Unterstützung sowohl bei praktischen Aufgaben also auch im moralischen Sinne.
Brigitte Berger danke ich für ihre Hilfe und Sorgfalt bei allen Formalitäten rund um das Doktorandinnendasein im Forschungszentrum.
Bei unserer Punkt-11:30-Essen-gehen-Runde bedanke ich mich für die vielfältigen Diskussionen über Gott-und-die-Welt, die genau für das richtige Maß an Ablenkung vom stressigen Wissenschaftsalltag gesorgt haben.
Meinen fleißigen Korrekturlesern danke ich für die vielen interessanten Vorschläge für die englische Zeichensetzung.

Schließlich möchte ich meiner Familie danken, die mich in allem unterstützt und ermutigt hat.

C. List of Publications

Novel method of generation of $Ca(HCO_3)_2$ and $CaCO_3$ aerosols and first determination of hygroscopic and cloud condensation nuclei activation properties,
D. F. Zhao, A. Buchholz, Th. F. Mentel, K.-P. Müller, J. Borchardt, A. Kiendler-Scharr, C. Spindler, R. Tillmann, A. Trimborn, T. Zhu, and A. Wahner; Atmospheric Chemistry Physics Discussions, **10**, 8009-8049, 2010.

The chemical and microphysical properties of secondary organic aerosols from Holm Oak emissions,
N. Lang-Yona, Y. Rudich, Th. F. Mentel, A. Buchholz, A. Kiendler-Scharr, E. Kleist, C. Spindler, R. Tillmann, and J. Wildt; Atmospheric Chemistry Physics Discussions, **10**, 4753-4788, 2010.

D. Erklärung

Ich versichere, dass ich die von mir vorgelegte Dissertation selbständig angefertigt, die benutzten Quellen und Hilfsmittel vollständig angegeben und die Stellen der Arbeit - einschließlich Tabellen, Karten und Abbildungen -, die anderen Werken im Wortlaut oder dem Sinn nach entnommen sind, in jedem Einzelfall als Entlehnung kenntlich gemacht habe; dass diese Dissertation noch keiner anderen Fakultät oder Universität zur Prüfung vorgelegen hat; dass sie - abgesehen von unten angegebenen Teilpublikationen - noch nicht veröffentlicht worden ist sowie, dass ich eine solche Veröffentlichung vor Abschluss des Promotionsverfahrens nicht vornehmen werde. Die Bestimmungen der Promotionsordnung sind mir bekannt. Die von mir vorgelegte Dissertation ist von Prof. Dr. R. Strey betreut worden.

Köln, den 04.08.2010 _____

Angela Buchholz

1. **Einsatz von multispektralen Satellitenbilddaten in der Wasserhaushalts- und Stoffstrommodellierung – dargestellt am Beispiel des Rureinzugsgebietes**
   von C. Montzka (2008), XX, 238 Seiten
   ISBN: 978-3-89336-508-1

2. **Ozone Production in the Atmosphere Simulation Chamber SAPHIR**
   by C. A. Richter (2008), XIV, 147 pages
   ISBN: 978-3-89336-513-5

3. **Entwicklung neuer Schutz- und Kontaktierungsschichten für Hochtemperatur-Brennstoffzellen**
   von T. Kiefer (2008), 138 Seiten
   ISBN: 978-3-89336-514-2

4. **Optimierung der Reflektivität keramischer Wärmedämmschichten aus Yttrium-teilstabilisiertem Zirkoniumdioxid für den Einsatz auf metallischen Komponenten in Gasturbinen**
   von A. Stuke (2008), X, 201 Seiten
   ISBN: 978-3-89336-515-9

5. **Lichtstreuende Oberflächen, Schichten und Schichtsysteme zur Verbesserung der Lichteinkopplung in Silizium-Dünnschichtsolarzellen**
   von M. Berginski (2008), XV, 171 Seiten
   ISBN: 978-3-89336-516-6

6. **Politikszenarien für den Klimaschutz IV – Szenarien bis 2030**
   hrsg.von P. Markewitz, F. Chr. Matthes (2008), 376 Seiten
   ISBN 978-3-89336-518-0

7. **Untersuchungen zum Verschmutzungsverhalten rheinischer Braunkohlen in Kohledampferzeugern**
   von A. Schlüter (2008), 164 Seiten
   ISBN 978-3-89336-524-1

8. **Inorganic Microporous Membranes for Gas Separation in Fossil Fuel Power Plants**
   by G. van der Donk (2008), VI, 120 pages
   ISBN: 978-3-89336-525-8

9. **Sinterung von Zirkoniumdioxid-Elektrolyten im Mehrlagenverbund der oxidkeramischen Brennstoffzelle (SOFC)**
   von R. Mücke (2008), VI, 165 Seiten
   ISBN: 978-3-89336-529-6

10. **Safety Considerations on Liquid Hydrogen**
    by K. Verfondern (2008), VIII, 167 pages
    ISBN: 978-3-89336-530-2

11. **Kerosinreformierung für Luftfahrtanwendungen**
von R. C. Samsun (2008), VII, 218 Seiten
ISBN: 978-3-89336-531-9

12. **Der 4. Deutsche Wasserstoff Congress 2008 – Tagungsband**
hrsg. von D. Stolten, B. Emonts, Th. Grube (2008), 269 Seiten
ISBN: 978-3-89336-533-3

13. **Organic matter in Late Devonian sediments as an indicator for environmental changes**
by M. Kloppisch (2008), XII, 188 pages
ISBN: 978-3-89336-534-0

14. **Entschwefelung von Mitteldestillaten für die Anwendung in mobilen Brennstoffzellen-Systemen**
von J. Latz (2008), XII, 215 Seiten
ISBN: 978-3-89336-535-7

15. **RED-IMPACT**
Impact of Partitioning, Transmutation and Waste Reduction Technologies on the Final Nuclear Waste Disposal
SYNTHESIS REPORT
ed. by W. von Lensa, R. Nabbi, M. Rossbach (2008), 178 pages
ISBN 978-3-89336-538-8

16. **Ferritic Steel Interconnectors and their Interactions with Ni Base Anodes in Solid Oxide Fuel Cells (SOFC)**
by J. H. Froitzheim (2008), 169 pages
ISBN: 978-3-89336-540-1

17. **Integrated Modelling of Nutrients in Selected River Basins of Turkey**
Results of a bilateral German-Turkish Research Project
project coord. M. Karpuzcu, F. Wendland (2008), XVI, 183 pages
ISBN: 978-3-89336-541-8

18. **Isotopengeochemische Studien zur klimatischen Ausprägung der Jüngeren Dryas in terrestrischen Archiven Eurasiens**
von J. Parplies (2008), XI, 155 Seiten, Anh.
ISBN: 978-3-89336-542-5

19. **Untersuchungen zur Klimavariabilität auf dem Tibetischen Plateau - Ein Beitrag auf der Basis stabiler Kohlenstoff- und Sauerstoffisotope in Jahrringen von Bäumen waldgrenznaher Standorte**
von J. Griessinger (2008), XIII, 172 Seiten
ISBN: 978-3-89336-544-9

20. **Neutron-Irradiation + Helium Hardening & Embrittlement Modeling of 9%Cr-Steels in an Engineering Perspective (HELENA)**
by R. Chaouadi (2008), VIII, 139 pages
ISBN: 978-3-89336-545-6

21. **in Bearbeitung**

22. **Verbundvorhaben APAWAGS (AOEV und Wassergenerierung) – Teilprojekt: Brennstoffreformierung – Schlussbericht**
von R. Peters, R. C. Samsun, J. Pasel, Z. Porš, D. Stolten (2008), VI, 106 Seiten
ISBN: 978-3-89336-547-0

23. **FREEVAL**
Evaluation of a Fire Radiative Power Product derived from Meteosat 8/9 and Identification of Operational User Needs
Final Report
project coord. M. Schultz, M. Wooster (2008), 139 pages
ISBN: 978-3-89336-549-4

24. **Untersuchungen zum Alkaliverhalten unter Oxycoal-Bedingungen**
von C. Weber (2008), VII, 143, XII Seiten
ISBN: 978-3-89336-551-7

25. **Grundlegende Untersuchungen zur Freisetzung von Spurstoffen, Heißgaschemie, Korrosionsbeständigkeit keramischer Werkstoffe und Alkalirückhaltung in der Druckkohlenstaubfeuerung**
von M. Müller (2008), 207 Seiten
ISBN: 978-3-89336-552-4

26. **Analytik von ozoninduzierten phenolischen Sekundärmetaboliten in *Nicotiana tabacum* L. cv Bel W3 mittels LC-MS**
von I. Koch (2008), III, V, 153 Seiten
ISBN 978-3-89336-553-1

27. **IEF-3 Report 2009. Grundlagenforschung für die Anwendung**
(2009), ca. 230 Seiten
ISBN: 978-3-89336-554-8

28. **Influence of Composition and Processing in the Oxidation Behavior of MCrAlY-Coatings for TBC Applications**
by J. Toscano (2009), 168 pages
ISBN: 978-3-89336-556-2

29. **Modellgestützte Analyse signifikanter Phosphorbelastungen in hessischen Oberflächengewässern aus diffusen und punktuellen Quellen**
von B. Tetzlaff (2009), 149 Seiten
ISBN: 978-3-89336-557-9

30. **Nickelreaktivlot / Oxidkeramik – Fügungen als elektrisch isolierende Dichtungskonzepte für Hochtemperatur-Brennstoffzellen-Stacks**
von S. Zügner (2009), 136 Seiten
ISBN: 978-3-89336-558-6

31. **Langzeitbeobachtung der Dosisbelastung der Bevölkerung in radioaktiv kontaminierten Gebieten Weißrusslands – Korma-Studie**
von H. Dederichs, J. Pillath, B. Heuel-Fabianek, P. Hill, R. Lennartz (2009), Getr. Pag.
ISBN: 978-3-89336-532-3

32. **Herstellung von Hochtemperatur-Brennstoffzellen über physikalische Gasphasenabscheidung**
von N. Jordán Escalona (2009), 148 Seiten
ISBN: 978-3-89336-532-3

33. **Real-time Digital Control of Plasma Position and Shape on the TEXTOR Tokamak**
by M. Mitri (2009), IV, 128 pages
ISBN: 978-3-89336-567-8

34. **Freisetzung und Einbindung von Alkalimetallverbindungen in kohlebefeuerten Kombikraftwerken**
von M. Müller (2009), 155 Seiten
ISBN: 978-3-89336-568-5

35. **Kosten von Brennstoffzellensystemen auf Massenbasis in Abhängigkeit von der Absatzmenge**
von J. Werhahn (2009), 242 Seiten
ISBN: 978-3-89336-569-2

36. **Einfluss von Reoxidationszyklen auf die Betriebsfestigkeit von anodengestützten Festoxid-Brennstoffzellen**
von M. Ettler (2009), 138 Seiten
ISBN: 978-3-89336-570-8

37. **Großflächige Plasmaabscheidung von mikrokristallinem Silizium für mikromorphe Dünnschichtsolarmodule**
von T. Kilper (2009), XVII, 154 Seiten
ISBN: 978-3-89336-572-2

38. **Generalized detailed balance theory of solar cells**
by T. Kirchartz (2009), IV, 198 pages
ISBN: 978-3-89336-573-9

39. **The Influence of the Dynamic Ergodic Divertor on the Radial Electric Field at the Tokamak TEXTOR**
von J. W. Coenen (2009), xii, 122, XXVI pages
ISBN: 978-3-89336-574-6

40. **Sicherheitstechnik im Wandel Nuklearer Systeme**
von K. Nünighoff (2009), viii, 215 Seiten
ISBN: 978-3-89336-578-4

41. **Pulvermetallurgie hochporöser NiTi-Legierungen für Implanat- und Dämpfungsanwendungen**
von M. Köhl (2009), XVII, 199 Seiten
ISBN: 978-3-89336-580-7

42. **Einfluss der Bondcoatzusammensetzung und Herstellungsparameter auf die Lebensdauer von Wärmedämmschichten bei zyklischer Temperaturbelastung**
von M. Subanovic (2009), 188, VI Seiten
ISBN: 978-3-89336-582-1

43. **Oxygen Permeation and Thermo-Chemical Stability of Oxygen Permeation Membrane Materials for the Oxyfuel Process**
by A. J. Ellett (2009), 176 pages
ISBN: 978-3-89336-581-4

44. **Korrosion von polykristallinem Aluminiumoxid (PCA) durch Metalljodidschmelzen sowie deren Benetzungseigenschaften**
von S. C. Fischer (2009), 148 Seiten
ISBN: 978-3-89336-584-5

45. **IEF-3 Report 2009. Basic Research for Applications**
(2009), 217 Seiten
ISBN: 978-3-89336-585-2

46. **Verbundvorhaben ELBASYS (Elektrische Basissysteme in einem CFK-Rumpf) - Teilprojekt: Brennstoffzellenabgase zur Tankinertisierung - Schlussbericht**
von R. Peters, J. Latz, J. Pasel, R. C. Samsun, D. Stolten
(2009), xi, 202 Seiten
ISBN: 978-3-89336-587-6

47. **Aging of ^{14}C-labeled Atrazine Residues in Soil: Location, Characterization and Biological Accessibility**
by N. D. Jablonowski (2009), IX, 104 pages
ISBN: 978-3-89336-588-3

48. **Entwicklung eines energetischen Sanierungsmodells für den europäischen Wohngebäudesektor unter dem Aspekt der Erstellung von Szenarien für Energie- und CO_2 - Einsparpotenziale bis 2030**
von P. Hansen (2009), XXII, 281 Seiten
ISBN: 978-3-89336-590-6

49. **Reduktion der Chromfreisetzung aus metallischen Interkonnektoren für Hochtemperaturbrennstofzellen durch Schutzschichtsysteme**
von R. Trebbels (2009), iii, 135 Seiten
ISBN: 978-3-89336-591-3

50. **Bruchmechanische Untersuchung von Metall / Keramik-Verbundsystemen für die Anwendung in der Hochtemperaturbrennstoffzelle**
von B. Kuhn (2009), 118 Seiten
ISBN: 978-3-89336-592-0

51. **Wasserstoff-Emissionen und ihre Auswirkungen auf den arktischen Ozonverlust**
Risikoanalyse einer globalen Wasserstoffwirtschaft
von T. Feck (2009), 180 Seiten
ISBN: 978-3-89336-593-7

52. **Development of a new Online Method for Compound Specific Measurements of Organic Aerosols**
by T. Hohaus (2009), 156 pages
ISBN: 978-3-89336-596-8

53. **Entwicklung einer FPGA basierten Ansteuerungselektronik für Justageeinheiten im Michelson Interferometer**
von H. Nöldgen (2009), 121 Seiten
ISBN: 978-3-89336-599-9

54. **Observation – and model – based study of the extratropical UT/LS**
by A. Kunz (2010), xii, 120, xii pages
ISBN: 978-3-89336-603-3

55. **Herstellung polykristalliner Szintillatoren für die Positronen-Emissions-Tomographie (PET)**
von S. K. Karim (2010), VIII, 154 Seiten
ISBN: 978-3-89336-610-1

56. **Kombination eines Gebäudekondensators mit H2-Rekombinatorelementen in Leichwasserreaktoren**
von S. Kelm (2010), vii, 119 Seiten
ISBN: 978-3-89336-611-8

57. **Plant Leaf Motion Estimation Using A 5D Affine Optical Flow Model**
by T. Schuchert (2010), X, 143 pages
ISBN: 978-3-89336-613-2

58. **Tracer-tracer relations as a tool for research on polar ozone loss**
by R. Müller (2010), 116 pages
ISBN: 978-3-89336-614-9

59. **Sorption of polycyclic aromatic hydrocarbon (PAH) to Yangtze River sediments and their components**
by J. Zhang (2010), X, 109 pages
ISBN: 978-3-89336-616-3

60. **Weltweite Innovationen bei der Entwicklung von CCS-Technologien und Möglichkeiten der Nutzung und des Recyclings von CO_2**
Studie im Auftrag des BMWi
von W. Kuckshinrichs et al. (2010), X, 139 Seiten
ISBN: 978-3-89336-617-0

61. **Herstellung und Charakterisierung von sauerstoffionenleitenden Dünnschichtmembranstrukturen**
von M. Betz (2010), XII, 112 Seiten
ISBN: 978-3-89336-618-7

62. **Politikszenarien für den Klimaschutz V – auf dem Weg zum Strukturwandel, Treibhausgas-Emissionsszenarien bis zum Jahr 2030**
hrsg. von P. Hansen, F. Chr. Matthes (2010), 276 Seiten
ISBN: 978-3-89336-619-4

63. **Charakterisierung Biogener Sekundärer Organischer Aerosole mit Statistischen Methoden**
von C. Spindler (2010), iv, 163 Seiten
ISBN: 978-3-89336-622-4

64. **Stabile Algorithmen für die Magnetotomographie an Brennstoffzellen**
von M. Wannert (2010), ix, 119 Seiten
ISBN: 978-3-89336-623-1

65. **Sauerstofftransport und Degradationsverhalten von Hochtemperaturmembranen für CO2-freie Kraftwerke**
von D. Schlehuber (2010), VII, 139 Seiten
ISBN: 978-3-89336-630-9

66. **Entwicklung und Herstellung von foliengegossenen, anodengestützten Festoxidbrennstoffzellen**
von W. Schafbauer (2010), VI, 164 Seiten
ISBN: 978-3-89336-631-6

67. **Disposal strategy of proton irradiated mercury from high power spallation sources**
by S. Chiriki (2010), xiv, 124 pages
ISBN: 978-3-89336-632-3

68. **Oxides with polyatomic anions considered as new electrolyte materials for solid oxide fuel cells (SOFCs)**
by O. H. Bin Hassan (2010), vii, 121 pages
ISBN: 978-3-89336-633-0

69. **Von der Komponente zum Stack: Entwicklung und Auslegung von HT-PEFC-Stacks der 5 kW-Klasse**
von A. Bendzulla (2010), IX, 203 Seiten
ISBN: 978-3-89336-634-7

70. **Satellitengestützte Schwerewellenmessungen in der Atmosphäre und Perspektiven einer zukünftigen ESA Mission (PREMIER)**
von S. Höfer (2010), 81 Seiten
ISBN: 978-3-89336-637-8

71. **Untersuchungen der Verhältnisse stabiler Kohlenstoffisotope in atmosphärisch relevanten VOC in Simulations- und Feldexperimenten**
von H. Spahn (2010), IV, 210 Seiten
ISBN: 978-3-89336-638-5

72. **Entwicklung und Charakterisierung eines metallischen Substrats für nanostrukturierte keramische Gastrennmembranen**
von K. Brands (2010), vii, 137 Seiten
ISBN: 978-3-89336-640-8

73. **Hybridisierung und Regelung eines mobilen Direktmethanol-Brennstoffzellen-Systems**
von J. Chr. Wilhelm (2010), 220 Seiten
ISBN: 978-3-89336-642-2

74. **Charakterisierung perowskitischer Hochtemperaturmembranen zur Sauerstoffbereitstellung für fossil gefeuerte Kraftwerksprozesse**
von S.A. Möbius (2010) III, 208 Seiten
ISBN: 978-3-89336-643-9

75. **Characterization of natural porous media by NMR and MRI techniques: High and low magnetic field studies for estimation of hydraulic properties**
by L.-R. Stingaciu (2010), 96 pages
ISBN: 978-3-89336-645-3

76. **Hydrological Characterization of a Forest Soil Using Electrical Resistivity Tomography**
by Chr. Oberdörster (2010), XXI, 151 pages
ISBN: 978-3-89336-647-7

77. **Ableitung von atomarem Sauerstoff und Wasserstoff aus Satellitendaten und deren Abhängigkeit vom solaren Zyklus**
von C. Lehmann (2010), 127 Seiten
ISBN: 978-3-89336-649-1

78. **18th World Hydrogen Energy Conference 2010 – WHEC2010 Proceedings**
Speeches and Plenary Talks
ed. by D. Stolten, B. Emonts (2010)
ISBN: 978-3-89336-658-3

78-1. **18th World Hydrogen Energy Conference 2010 – WHEC2010 Proceedings**
Parallel Sessions Book 1:
Fuel Cell Basics / Fuel Infrastructures
ed. by D. Stolten, T. Grube (2010), ca. 460 pages
ISBN: 978-3-89336-651-4

78-2. **18th World Hydrogen Energy Conference 2010 – WHEC2010 Proceedings**
Parallel Sessions Book 2:
Hydrogen Production Technologies – Part 1
ed. by D. Stolten, T. Grube (2010), ca. 400 pages
ISBN: 978-3-89336-652-1

78-3. **18th World Hydrogen Energy Conference 2010 – WHEC2010 Proceedings**
Parallel Sessions Book 3:
Hydrogen Production Technologies – Part 2
ed. by D. Stolten, T. Grube (2010), ca. 640 pages
ISBN: 978-3-89336-653-8

78-4. **18th World Hydrogen Energy Conference 2010 – WHEC2010 Proceedings**
Parallel Sessions Book 4:
Storage Systems / Policy Perspectives, Initiatives and Cooperations
ed. by D. Stolten, T. Grube (2010), ca. 500 pages
ISBN: 978-3-89336-654-5

78-5. **18th World Hydrogen Energy Conference 2010 – WHEC2010 Proceedings**
Parallel Sessions Book 5:
Stategic Analysis / Safety Issues / Existing and Emerging Markets
ed. by D. Stolten, T. Grube (2010), ca. 530 pages
ISBN: 978-3-89336-655-2

78-6. **18th World Hydrogen Energy Conference 2010 – WHEC2010 Proceedings**
Parallel Sessions Book 6:
Stationary Applications / Transportation Applications
ed. by D. Stolten, T. Grube (2010), ca. 330 pages
ISBN: 978-3-89336-656-9

78 Set (complete book series)

18th World Hydrogen Energy Conference 2010 – WHEC2010 Proceedings
ed. by D. Stolten, T. Grube, B. Emonts (2010)
ISBN: 978-3-89336-657-6

79. **Ultrafast voltex core dynamics investigated by finite-element micromagnetic simulations**
by S. Gliga (2010), vi, 144 pages
ISBN: 978-3-89336-660-6

80. **Herstellung und Charakterisierung von keramik- und metallgestützten Membranschichten für die CO_2-Abtrennung in fossilen Kraftwerken**
von F. Hauler (2010), XVIII, 178 Seiten
ISBN: 978-3-89336-662-0

81. **Experiments and numerical studies on transport of sulfadiazine in soil columns**
by M. Unold (2010), xvi, 115 pages
ISBN: 978-3-89336-663-7

82. **Prompt-Gamma-Neutronen-Aktivierungs-Analyse zur zerstörungsfreien Charakterisierung radioaktiver Abfälle**
von J.P.H. Kettler (2010), iv, 205 Seiten
ISBN: 978-3-89336-665-1

83. **Transportparameter dünner geträgerter Kathodenschichten der oxidkeramischen Brennstoffzelle**
von C. Wedershoven (2010), vi, 137 Seiten
ISBN: 978-3-89336-666-8

84. **Charakterisierung der Quellverteilung von Feinstaub und Stickoxiden in ländlichem und städtischem Gebiet**
von S. Urban (2010), vi, 211 Seiten
ISBN: 978-3-89336-669-9

85. **Optics of Nanostructured Thin-Film Silicon Solar Cells**
by C. Haase (2010), 150 pages
ISBN: 978-3-89336-671-2

86. **Entwicklung einer Isolationsschicht für einen Leichtbau-SOFC-Stack**
von R. Berhane (2010), X, 162 Seiten
ISBN: 978-3-89336-672-9

87. **Hydrogen recycling and transport in the helical divertor of TEXTOR**
by M. Clever (2010), x, 172 pages
ISBN: 978-3-89336-673-6

88. **Räumlich differenzierte Quantifizierung der N- und P-Einträge in Grundwasser und Oberflächengewässer in Nordrhein-Westfalen unter besonderer Berücksichtigung diffuser landwirtschaftlicher Quellen**
von F. Wendland et. al. (2010), xii, 216 Seiten
ISBN: 978-3-89336-674-3

89. **Oxidationskinetik innovativer Kohlenstoffmaterialien hinsichtlich schwerer Lufteinbruchstörfälle in HTR´s und Graphitentsorgung oder Aufarbeitung**
von B. Schlögl (2010), ix, 117 Seiten
ISBN: 978-3-89336-676-7

90. **Chemische Heißgasreinigung bei Biomassenvergasungsprozessen**
von M. Stemmler (2010), xv, 196 Seiten
ISBN: 978-3-89336-678-1

91. **Untersuchung und Optimierung der Serienverschaltung von Silizium-Dünnschicht-Solarmodulen**
von S. Haas (2010), ii, 202 Seiten
ISBN: 978-3-89336-680-4

92. **Non-invasive monitoring of water and solute fluxes in a cropped soil**
by S. Garré (2010), xxiv, 133 pages
ISBN: 978-3-89336-681-1

93. **Improved hydrogen sorption kinetics in wet ball milled Mg hydrides**
by L. Meng (2011), II, 119 pages
ISBN: 978-3-89336-687-3

94. **Materials for Advanced Power Engineering 2010**
ed. by J. Lecomte-Beckers, Q. Contrepois, T. Beck and B. Kuhn
(2010), 1327 pages
ISBN: 978-3-89336-685-9

95. **2D cross-hole MMR – Survey design and sensitivity analysis for cross-hole applications of the magnetometric resistivity**
by D. Fielitz (2011), xvi, 123 pages
ISBN: 978-3-89336-689-7

96. **Untersuchungen zur Oberflächenspannung von Kohleschlacken unter Vergasungsbedingungen**
von T. Melchior (2011), xvii, 270 Seiten
ISBN: 978-3-89336-690-3

97. **Secondary Organic Aerosols: Chemical Aging, Hygroscopicity, and Cloud Droplet Activation**
by A. Buchholz (2011), xiv, 134 pages
ISBN: 978-3-89336-691-0

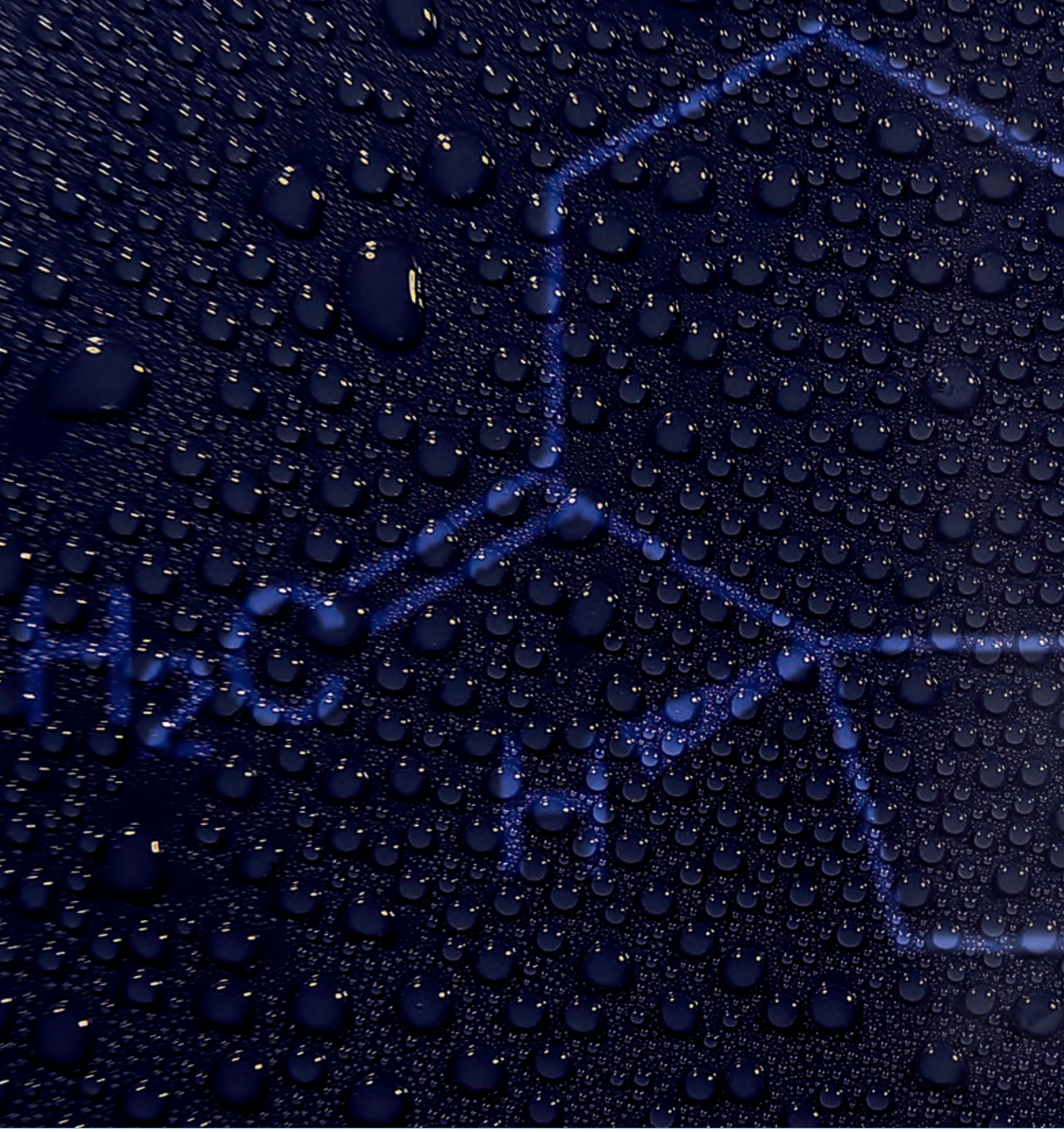

Energie & Umwelt / Energy & Environment
Band / Volume 97
ISBN 978-3-89336-691-0

JÜLICH
FORSCHUNGSZENTRUM